EXPLORING IRON METABOLISM AND REGULATION IN *SACCHAROMYCES CEREVISIAE* USING AN INTEGRATIVE BIOPHYSICAL AND BIOANALYTICAL APPROACH

A Dissertation

by

JINKYU PARK

Submitted to the Office of Graduate and Professional Studies of
Texas A&M University
in partial fulfillment of the requirements for the degree of

DOCTOR OF PHILOSOPHY

Chair of Committee,	Paul A. Lindahl
Committee Members,	Tadhg P. Begley
	Frank M. Raushel
	Gregory D. Reinhart
Head of Department,	David H. Russell

December 2013

Major Subject: Chemistry

ABSTRACT

Fe metabolism in budding yeast *Saccharomyces cerevisiae* was studied using an integrative systems-level approach involving Mössbauer, EPR, UV-Vis spectroscopy and LC-ICP-MS, combined with conventional biochemical techniques. Wild-type cells growing exponentially on rich and minimal media were well-regulated in terms of cellular Fe homeostasis, while post-exponentially grown cells were unregulated. Such cells became overloaded with Fe^{III} oxyhydroxide nanoparticles and nonheme high spin (NHHS) Fe^{III}. Fe overloading probably arose from a mismatch between growth rate and Fe uptake rate. A mathematical model that describes iron trafficking and regulation in these cells was developed.

The speciation of Fe in cells also depended on the nutrient composition of the growth media. Adenine deficiency induced a transient reduction of vacuolar Fe^{III} to Fe^{II} which probably accumulated in the cytosol. The concentration of glucose impacted the Fe import rate but had little effect on Fe speciation. The concentration of amino acids and nucleotide bases impacted the level of Fe accumulation and shifted the Fe distribution toward NHHS Fe^{II}. A thermodynamic model which correlated nutrient-dependent Fe transformations with vacuolar pH and redox status was developed.

The effect of deleting the *MTM1* gene, which encodes a transport carrier on the mitochondrial inner membrane, was investigated. Deleting *MTM1* caused Fe to accumulate in mitochondria and the Mn superoxide dismutase 2 (SOD2) activity to decline. Previous studies had concluded that this inactivation arose from the

misincorporation of Fe into apo-Sod2p. Most of the accumulated Fe was found to be Fe^{III} nanoparticles which are unlikely to misincorporate into apo-Sod2p. Soluble extracts from WT and Δ*mtm1* mitochondria were subjected to size-exclusion and anion-exchange liquid chromatography interfaced with an on-line ICP-MS. Two major Mn peaks were observed, one due to MnSod2p and the other to a Mn species with a molecular mass of 2 - 3 kDa. None of the Fe traces comigrated precisely with MnSod2p, contrary to the Fe-misincorporation hypothesis. Deleting *MTM1* probably diminishes SOD2 activity by failing to metallate apo-Sod2 protein. The low-molecular-mass Mn species may function to install Mn into apo-Sod2p during maturation in the mitochondrial matrix, using some maturation factor imported by Mtm1p.

DEDICATION

I dedicate this work to my family. My parents, my brothers, and my wife, Jinhee have always supported me to become successful in daily life and professional pursuit by providing the love and encouragement.

ACKNOWLEDGEMENTS

I would like to express my deepest gratitude to my advisor, Dr. Paul A. Lindahl who has supported me during my research and the preparation of this dissertation. He has always helped me with the constant and generous encouragement, and wise guidance throughout the course of this research. I also would like to thank my committee members; Dr. Tadhg P. Begley, Dr. Frank M. Raushel, and Dr. Gregory D. Reinhart for their time and professional advices.

Thanks also go to all Dr. Lindahl's lab members, past and present: Jessica, Ren, Greg, Allison, Nema, Mike, Marco, Wolfgang and Ivan for their kind help, encouragement and discussion. Especially I would like to thank Sean for his great contribution to all my projects.

I also wish to thank our collaborators: Dr. Roland Lill and Dr. Jerry Kaplan for the generous gifts of yeast strains; Dr. Andrew Dancis for the generous gifts of yeast strain and antibody; Dr. Valeria Culotta for the generous gift of antibody and helpful advice; Dr. Brad Pierce for allowing us to use his EPR spectrometer; Dr. Eckard Münck for collecting high field Mössbauer spectrum.

Finally, I thank my parents and brothers for their encouragement and my wife for her patience and love.

NOMENCLATURE

AIR	phosphoribosylaminoimidazole
apo-Sod2p	Sod2 protein prior to metal installation
ASR	apo-Sod2p reactive
CAIR	phosphoribosylaminoimidazole carboxylate
CD	central doublet
CIA	cytosolic iron sulfur cluster assembly
CVs	column-volumes
δ	isomer shift
ΔE_Q	quadrupole splitting
DMSO	dimethyl sulfoxide
DNP	2,4-dinitrophenyl
DNPH	2,4-dinitrophenylhydrazine
DT	doubling time
DTPA	diethylenetriamine pentaacetate
ENDOR	electron nuclear double resonance
EPR	electron paramagnetic resonance
Fe_{ASR}	sought-after Fe species proposed to misincorporate into apo-Sod2p
FeSod2p	inactive form of Sod2p, with Fe bound
FPLC	fast protein liquid chromatography

HI	high affinity pathway
HPLC	high-performance liquid chromatography
HS	high spin
ICP-MS	inductively coupled plasma mass spectrometry
IMM	intermediate molecular mass
INT	iodonitrotetrazolium
ISC	iron sulfur cluster
LC	liquid chromatography
LMM	low molecular mass
LO	low affinity pathway
LS	low spin
MB	Mössbauer
MF	apo-Sod2p maturation factor
MM	minimal medium
Mn_{ASR}	Mn species that incorporates into apo-Sod2p
MnSod2p	active form of Sod2p, with Mn bound
Mtm1p	Manganese Trafficking factor for Mitochondrial SOD2, YGR257C; Mol. Wt 40,763 Da)
NHHS	nonheme high spin
OD, OD_{600}	optical density at 600 nm
ODE	ordinary differential equation
PMSF	phenylmethanesulfonylfluoride

ROS	reactive oxygen species
SDH	succinate dehydrogenase
SDS	sodium dodecyl sulfate
SOD2	superoxide dismutase 2
TOR	target of rapamycin
TORC1	TOR complex 1
WT	wild type
XAS	X-ray absorption spectroscopy
YNB	yeast nitrogen base
YPAD	yeast extracts, peptone, adenine hemisulfate, and dextrose

TABLE OF CONTENTS

LIST OF FIGURES

LIST OF TABLES

CHAPTER I

INTRODUCTION

Importance of Fe and Its Regulation in Biological Systems

The redox-active transition metal iron (Fe) plays fundamental roles in biological systems by participating in enzyme catalysis, electron transfer processes, small-molecule binding and substrate activation.[1] Fe in biological systems can be stabilized in a wide range of oxidation states. The most common redox states are Fe^{III} and Fe^{II}, but Fe^{I}, Fe^{IV} and Fe^{V} states have been observed in catalytic intermediates. The Fe^{II}/Fe^{III} redox potential is highly variable, but it can be finely tuned via use of different ligands. Thus, Fe compounds cover almost the entire range of biologically relevant redox potentials, from *ca.* –0.5 V to *ca.* +0.6 V. Fe can be found in various forms in biological systems, including Fe/S clusters, heme centers, nonheme mono- and dinuclear complexes among others.

Examples of Fe-containing enzymes include ribonucleotide reductase (RNR) which catalyzes the reduction of ribonucleotides to their corresponding dexoy-ribonucleotides.[2] Class Ia RNR utilizes a dinuclear Fe center while class III RNR employs an Fe/S cluster active site. Fe is essential in the mitochondrial electron transport chain and in the citric acid cycle, both of which are required to generate chemical energy in the form of adenosyl triphosphate (ATP) for cellular function. Here, Fe is found as Fe_2S_2, Fe_3S_4, and Fe_4S_4 clusters and as numerous types of heme centers. Such prosthetic groups are incorporated into proteins including cytochromes, cytochrome c oxidase,

succinate dehydrogenase and aconitase.[1] Fe in hemoglobin and myoglobin reversibly bind molecular O_2. Hemoglobin transports O_2 from the lungs to bodily tissues where it transfers O_2 to myoglobin for storage.[1] Bacterial dioxygenases convert aromatic molecules, often in the soil, into nonaromatic compounds which are then utilizable as carbon sources for cell growth.[3] These enzymes employ nonheme high spin (NHHS) Fe centers as a cofactor; some of them additionally contain a Fe_2S_2 cluster. Another group of enzymes utilizing an Fe cofactor is the radical *S*-adenosylmethionine (SAM) superfamily.[4] This family comprises more than 2,800 proteins with three cysteine residues and a SAM moiety together bound to Fe_4S_4. The members partake in more than 40 different biochemical transformations including radical isomerization of lysine, biotin biosynthesis and thiamine biosynthesis.

Conversely, Fe can also be *deleterious* to cells, in that certain forms can participate in Fenton chemistry that generate reactive oxygen species (ROS) which can, in turn, damage DNA, proteins, and membranes.[5] ROS typically includes superoxide anion radical (O_2^-), hydroxyl radical (•OH) and hydrogen peroxide (H_2O_2). The major source of O_2^- is the electron transport chain in mitochondria. H_2O_2 is the by-product of O_2^- scavenging by superoxide dismutases. Of all ROS, •OH is the most reactive as it reacts with most biomolecules at virtually diffusion-limited rates. The anionic charge of O_2^- inhibits its reaction with anionic molecules and H_2O_2 has a relatively stable O-O bond to diminish its reactivity. The Fenton reaction produces •OH from H_2O_2 according to the reaction [$Fe^{2+} + H_2O_2 \rightarrow Fe^{3+} + {\bullet}OH + OH^-$]. Thus, rigorous Fe regulation is expected to be a critical aspect of cellular Fe metabolism.

Fe Regulation and Trafficking in Yeast

The molecular-level details of Fe regulation and trafficking are best understood in the budding yeast *Saccharomyces cerevisiae*. Transcription factors Aft1p/Aft2p encode at least 20 Fe-related genes in this organism, including Fe reductases and permeases.[6] These transcription factors translocate from cytosol to the nucleus in response to low intracellular Fe; once in the nucleus they activate the transcription of genes of the Fe regulon.[7] Fe sensing by Aft1p/Aft2p requires the regulatory proteins Fra1p/Fra2p and the monothiol glutaredoxins Grx3p/Grx4p. It has been suggested that the Fe_2S_2 cluster-bridged Fra2p-Grx3p or Grx4p heterodimer inhibits Aft1p/Aft2p activation under Fe-replete condition.[8]

Fe trafficking via plasma membrane-bound Fe transporters

The major "traffic hubs" in Fe metabolism include the mitochondria and vacuoles, but the plasma membrane, cytosol and nucleus also play important roles.[9,10] The plasma membrane contains numerous proteins that import Fe from the environment (Figure I-1). Also involved are ferric reductases, Fre1-4p, which reduce environmental Fe^{III} to Fe^{II}, thereby 'labilizing' the metal ion (Fe^{II} complexes have far faster ligand exchange kinetics than Fe^{III} and are thus considered to be more 'labile').[11-13] Since most of the Fe in nature favor the +3 oxidation state, which is extremely insoluble in water ($[Fe^{III}] = 10^{-18}$ M at pH 7.0), this is a strategy of *S. cerevisiae* to outcompete other organisms for Fe uptake in an Fe-deficient environment. The reduced Fe, if not bound by siderophore ligands (see below), is transported via the membrane-bound Fet3p/Ftr1p

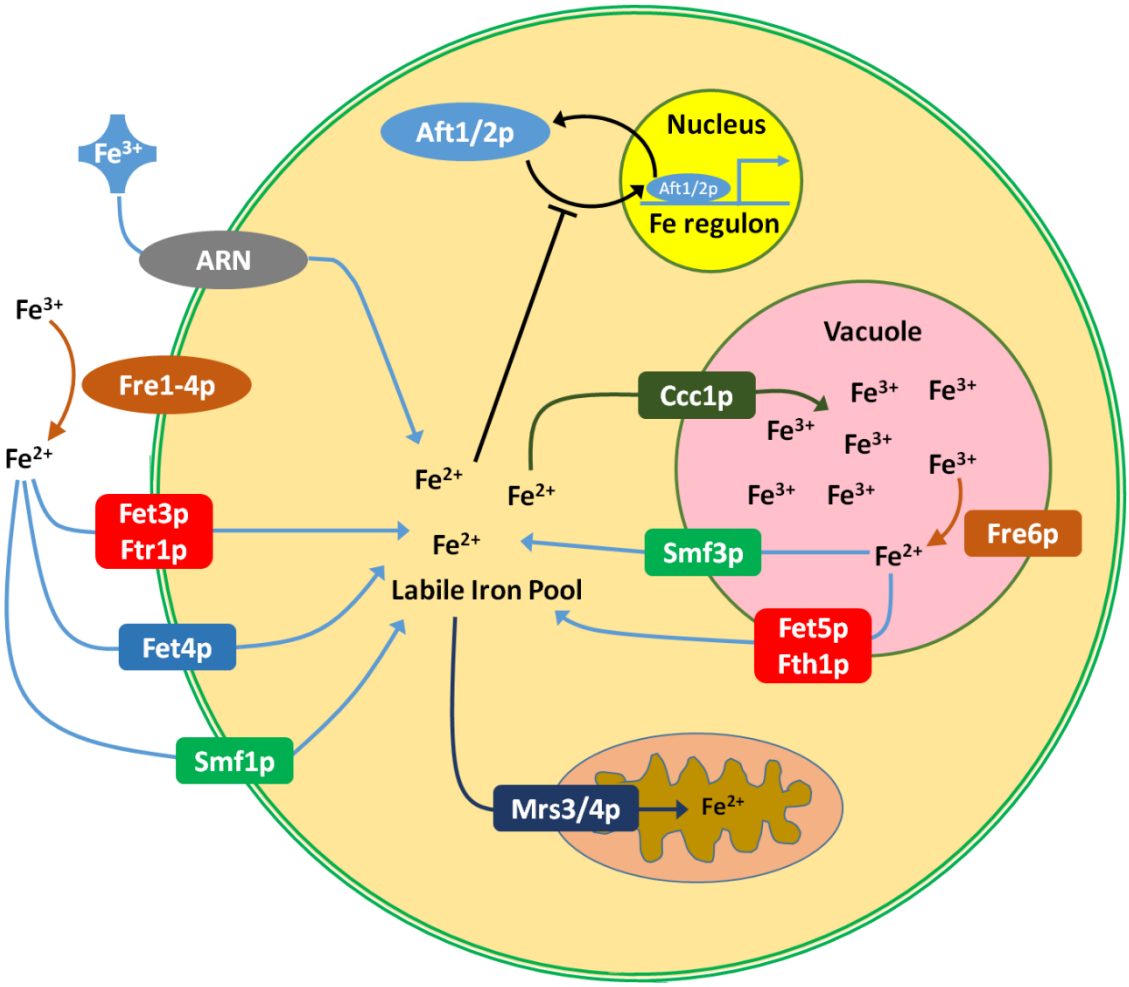

Figure I-1. Fe trafficking in *Saccharomyces cerevisiae*.

(multi-copper peroxidase/Fe^{III} permease) complex. This complex constitutes the "high-affinity" Fe importer. Low-affinity Fe importers include Smf1p and Fet4p.[14] Another strategy used by *S. cerevisiae* is to uptake siderophore–bound Fe^{III}. ARN family transporters are responsible for siderophore-bound Fe uptake although *S. cerevisiae* does not produce any siderophores of its own.[15-17]

Fet3p is a multi-copper oxidase which facilitates Fe uptake by catalyzing the oxidation of reductase-generated Fe^{II}. Ftr1p transports the resultant Fe^{III} into the cytosol where it becomes re-reduced to the Fe^{II} state. Both proteins are regulated by Aft1p/Aft2p in response to medium Fe level. Fe uptake via the high-affinity system is saturable, with an apparent K_m = 0.2 μM.[18] The Fet3p expression level during mid- to late-exponential growth (OD 1.0 – 1.4) was undetectable by Western blot at the medium Fe concentration above 1 μM,[19] implying its tight regulation by Aft1p/Aft2p.

Fet4p, a low-affinity divalent metal transporter, is induced by Aft1p in response to low concentrations of medium Fe.[20] Fe uptake via Fet4p is also saturable, with K_m = 35 μM.[21,22] Its expression can be detected by Western blot in cells grown on medium supplemented with as high as 1 mM Fe.[22] A LacZ reporter activity assay was used to show that Fet4p expression levels remain at about 40% of the maximum level (where the medium Fe was at 0.5 μM) as the medium Fe increases up to 50 μM.[20]

Fet4p transports several other metal ions including Cu and Zn. [20] Its expression is sensitive to low Zn ion concentrations regulated via Zap1p, a Zn-regulated transcription factor.[20] Smf1p is a plasma membrane protein that may constitute a second low-affinity Fe importer. It is a divalent metal transporter that primarily transports Mn^{II}. It can also

transport Fe^{II}, albeit with low affinity.[23] Fe uptake via Smf1p is also saturable with K_m = 2.2 μM.[24]

Fe that enters the cytosol becomes part of a pool of redox-active Fe complexes with unknown ligand(s). This pool is often called labile Fe pool (LIP) and has been operationally defined as Fe that is reactive to cell-permeable chelators such as calcein.[25] The LIP is believed to supply Fe to mitochondrial Fe/S cluster and heme biosynthesis in addition to many cytosolic Fe-containing enzymes. Its size has been proposed to vary from nM → μM among mammalian and yeast cells, as estimated by chelator methods.[26,27] The ligand(s) involved in the LIP have not been identified. They have been suggested to be adenine nucleotides or glutathione, but a diverse population of multiple ligands would appear capable of coordinating cytosolic Fe.[25,28,29]

Fe trafficking in mitochondria

The mitochondrion is double-membrane enclosed structure found in most eukaryotic cells.[30] It is surrounded by an outer membrane (OM) that separates the intermembrane space (IMS) from the cytosol. The inner mitochondrial membrane (IM) separates the internal matrix from the IMS. Energy-generating metabolism occurs within the IM via electron transport chain and citric acid cycle. The OM is relatively permeable due to the presence of many *porin* molecules. These ion channels, associated with the lipid bilayer, allow molecules of 5 kD or less to enter the IMS. Low-molecular-mass (LMM) forms of cytosolic Fe are considered to enter the IMS without restriction, but the cytosol-to-IMS pathway is poorly characterized. Contrary to the OM, the IM is

impermeable to most diffusing molecules, thereby providing a chemically isolated environment in the matrix. This aqueous space contains a highly concentrated mixture of enzymes.

Nucleus-encoded proteins are imported into the mitochondrion via protein translocases of the outer and inner membranes (called TOM and TIM proteins).[30] For example, mitochondrial Cu/Zn superoxide dismutase (SOD1) is imported via TOM and maturated in IMS. Mn superoxide dismutase (SOD2) translocates via TIM/TOM complex and folded in matrix. Cytosolic Fe also requires IM-bound Fe transporters to enter matrix.[31,32] Mrs3p and Mrs4p are the high-affinity transporters of Fe into the matrix.[32] These redundant proteins provide the Fe required for mitochondrial Fe/S cluster assembly and heme biosynthesis. The double Δ*mrs3*Δ*mrs4* mutant strain requires a higher concentration of Fe in the medium to grow normally and synthesize Fe/S cluster at the wild-type rate. The type of Fe used as the substrate for these processes is unknown.

Once internalized, Fe has been proposed to form a mitochondrial LIP supplying Fe for mitochondrial ISC and heme biosynthetic pathways.[33] According to chelator studies on rat hepatocytes, the mitochondrial LIP represents 0.4% - 25% of total Fe in the organelles.[33,34] Recently, a Mössbauer study identified a nonheme high spin (NHHS) Fe^{II} pool that might be the LIP; this species accounted for ~ 20% of total organellar Fe (corresponding to ~ 150 μM).[35] Discrepancy among these data may originate from the differences in organisms (mammalian vs. yeast) or in preparation methods of mitochondria (aerobic vs. anaerobic). Mössbauer parameters of NHHS Fe^{II} species

suggested that the Fe is coordinated by five to six O and N ligands. The labile character of NHHS Fe^{II} complex is consistent with a trafficking role.

Physiological evidence for a mitochondrial LIP has been reported in studies of ISC assembly in isolated mitochondria. New ISCs were synthesized on mitochondrial ISC proteins, aconitase and Yah1 ferredoxin, without exogenous Fe added, implying that endogenous Fe was donated to ISC assembly.[36,37] When membrane permeable Fe chelator, 1,10-phenanthroline, was added, no holoprotein was formed. This study provides substantial evidence that the mitochondrial LIP served as feedstock for ISC and heme syntheses. The nature of the complex involved remains unknown.

Another major unknown is how Fe (in the form of hemes and Fe/S clusters) exports the mitochondria; no transporters have been identified. Atm1p has been proposed to be a putative mitochondrial Fe exporter involved in cytosolic Fe/S cluster (ISC) assembly[38] but this is uncertain.

Fe trafficking in vacuoles

Yeast vacuoles are acidic (pH ~5.3)[39] membrane-enclosed organelles which stores nutrients including amino acids and polyphosphates. They also store metals such as Fe, Pb and Cd for future use, or sequester them as a means of detoxification.[40-42] Excess cytosolic Fe is imported into or exported out of vacuoles, depending on Fe availability. Ccc1p is the only known Fe importer located on the vacuolar membrane, although Fe can also be imported via Ccc1p-independent endocytosis (implying another import mechanism).[42] Yap5p is an Fe-sensing transcription factor that regulates the

transcription of *CCC1* mRNA in response to cytosolic Fe.[43] *CCC1* mRNA is also regulated by Cth1p/2p; the binding of these proteins under Fe-limited conditions destabilizes the message thereby preventing its translation.[44] Limited Fe availability also induces vacuolar membrane-bound Fe efflux systems, Fet5p/Fth1p and Smf3p/Fre6p, to mobilize the stored Fe.[45] The dominant form of Fe in the organelle is proposed to be a redox-active mononuclear high-spin (HS) Fe^{III} complex with polyphosphate-related ligands.[46]

Yeast Metabolic Modes

Yeast cells utilize fermentation and respiration as major energy-generating metabolisms depending on nutrient and O_2 availability. Under glucose-replete or anaerobic growth conditions they exclusively undergo fermentation, while respiration is predominant under glucose-depleted and aerobic conditions. During growth, if the glucose in medium is exhausted, cells switch the metabolism from fermentation to respiration by a process called the *diauxic shift*.[47]

Both metabolisms are initiated with glycolysis which produces two pyruvate molecules from one molecule of glucose while generating two molecules of ATP.[30] During fermentation, one of the resulting pyruvate molecules is converted to ethanol and carbon dioxide. During respiration, pyruvate enters the mitochondrial matrix where it feeds into the citric acid cycle (TCA cycle), a series of chemical reactions generating two molecules of ATP per glucose molecule. During the TCA cycle, reducing equivalents, reduced nicotinamide adenine dinucleotide (NADH) and flavin adenine

dinucleotide ($FADH_2$) are also produced. These redox carriers donate electrons to the electron transport chain for oxidative phosphorylation, generating 26 molecules of ATP per glucose molecule.

The electron transport chain consists of four complexes, including Complex I-IV.[30] These complexes are packed with Fe/S clusters and heme centers. Complex I contains flavin mononucleotide (FMN) and a series of Fe/S clusters. Respiratory Complex II, also known as succinate dehydrogenase (SDH) transfers electrons from $FADH_2$ to Q for entry into the electron transport chain, while converting succinate to fumarate. It contains three Fe/S clusters and one heme center. Complex III contains three heme centers as well as an Fe/S cluster. Finally, Complex IV, also known as cytochrome c oxidase, oxidizes the reduced cytochrome *c* generated by Complex III. This is coupled to the reduction of O_2 to two molecules of H_2O and to the translocation of four protons per reaction cycle out of the matrix. Complex IV utilizes not only two heme groups as other complexes, but also two copper sites including dinuclear Cu_A and mononuclear Cu_B. The resultant pH gradient (matrix side basic) powers Respiratory Complex V (ATP synthase) also associated with IM to synthesize ATP from ADP and phosphate.

Although the electron transport chain is remarkably successful in the complete reduction of O_2 without releasing intermediates, small amounts of O_2^- are occasionally produced due to partial O_2 reduction.[30] SOD2 is a part of cellular defense system against ROS, scavenging O_2^- by catalyzing the reaction [$2O_2^- + 2H+ \rightarrow O_2 + H_2O_2$]. SOD2 protects the matrix where the O_2^- is generated mainly by Respiratory Complexes I and

III. SOD2-generated H_2O_2 is decomposed to O_2 and H_2O by catalase, a ubiquitous heme-containing protein.

SOD2 utilizes manganese as a cofactor, which is coordinated in a distorted trigonal bipyramid by three histidines, an aspartate and a solvent molecule.[48] Fe superoxide dismutase (Fe-SOD) found in bacteria and plant employs the same ligands in the same geometry with slightly different ligand side chain rotations or distances to the metal ion.[49] This similarity causes mismetallation into the active site of each enzyme if both metals are available, and thus mismetallated enzymes are catalytically inactivated except for cambialistic SODs. Possible reasons for the enzyme inactivation include distortion of the active-site by nonnative metal ions, inability to bind the substrate and the inability to supply the required proton. Also, a reduction potential (E^0) of the metal ion in Fe-substituted Mn-SOD is well below 0.2 – 0.4 V (vs. SHE), which is typical E^0 observed in most Fe- and Mn-SODs, indicating that the enzyme is unable to mediate both catalytic half-reactions effectively. Therefore, mismetallation in SOD2 by Fe may be a critical issue regarding both Fe regulation and cellular ROS defense.

Mitochondrial Fe/S Cluster Assembly

The numerous Fe-containing cofactors contained in the respiratory complexes are synthesized within the mitochondria. The last step of heme biosynthetic pathway is the installation of Fe into protoporphyrin IX by ferrochelatase located on IM. Mitochondrial Fe/S cluster biosynthetic pathway involves a number of proteins (Figure I-2).[38] Fe/S clusters are assembled on a scaffold protein called Isu1p/2p. Yfh1p, a yeast homolog of

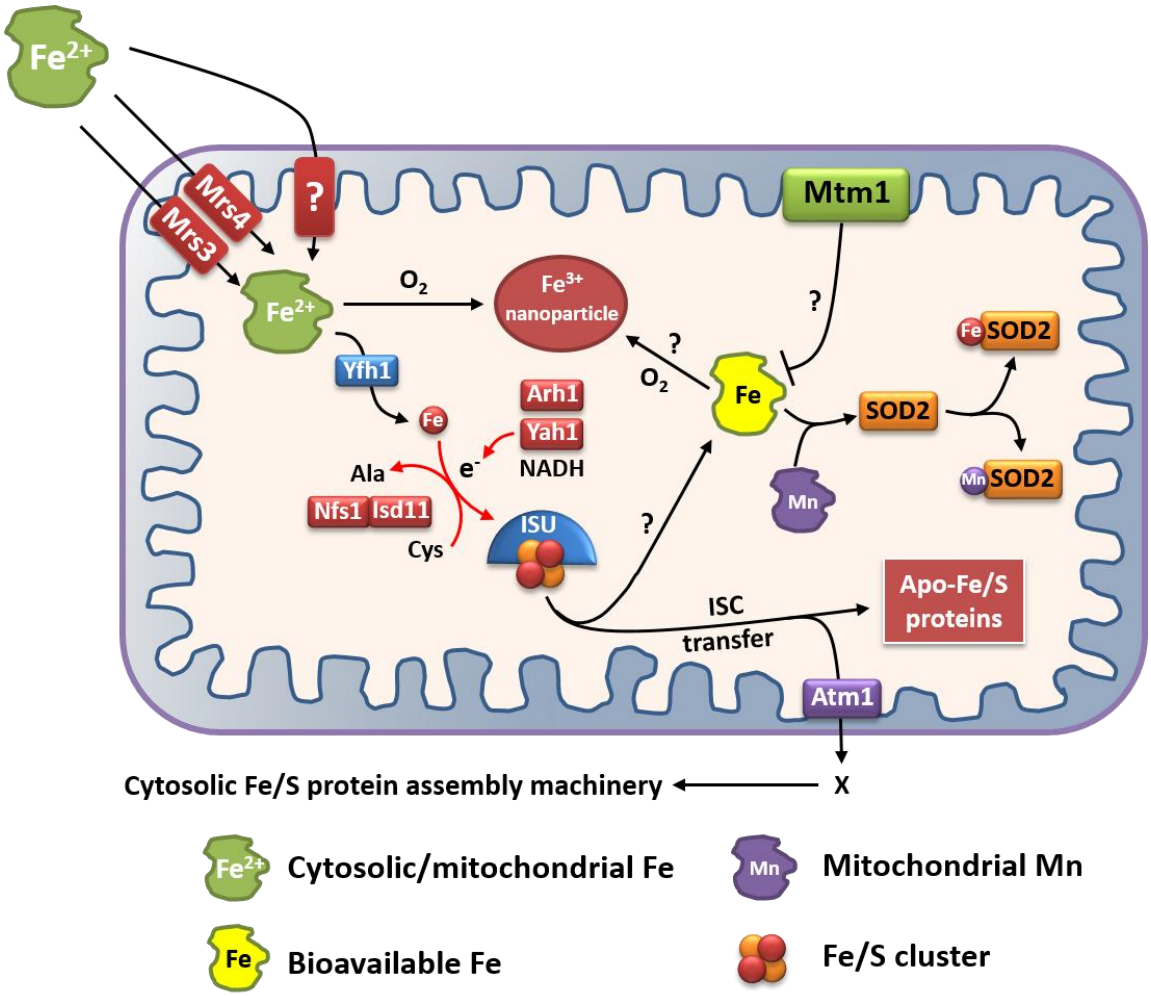

Figure I-2. Mitochondrial Fe/S cluster assembly pathway and a suggested mechanism of SOD2 inactivation by the deletion of *MTM1*.

frataxin, a deficiency of which is responsible for a neurodegenerative disease Friedrich's Ataxia, has a controversial role, either donating Fe to Isu1p[50] or allosterically activating the Fe/S cluster biosynthetic complex.[51] Cysteine desulfurase, composed of Nfs1p complexed with Isd11p, supplies sulfur to the scaffold protein. The electron transport chain supplies NADH, which is used by ferredoxin reductase (Arh1p) and ferredoxin (Yah1p) to provide electrons to reduce sulfur to sulfide in Fe/S cluster assembly.

Once assembled, the cluster is transferred and installed into recipient apoproteins facilitated by chaperone proteins such as Ssq1p and Grx5p. Interestingly, Atm1p, an ATP-binding cassette (ABC) transporter associated with inner mitochondrial membrane (IMM), is proposed to transport an unknown, Fe- and/or sulfur-containing species produced during the Fe/S cluster assembly to cytosol for cytosolic Fe/S protein assembly machinery.[52]

Suggested Role of Mtm1p and SOD2 Inactivation Mechanism

Another IM-bound protein, Mtm1p, has been suggested to have a role in an Fe/S cluster transfer step; its deletion causes the inactivation of SOD2 reportedly due to Fe misincorporation.[53-55] Mtm1p is a member of the mitochondrial carrier family.[53,56] Located in the mitochondrial IM, members of this family transport low-molecular-weight (LMW) species between the cytosol and the matrix of the organelle. Culotta and coworkers discovered that deleting the *MTM1* gene partially inactivates SOD2,[53,54] suggesting that Mtm1p might be involved in Mn metabolism. During maturation, apo-Sod2p is sent to the mitochondrial matrix where Mn is installed during folding,

suggesting that Mtm1p either imports Mn or is a chaperone for that installation. However, Mn concentrations within Δ*mtm1* mitochondria are elevated relative to that of WT mitochondria, [53] discounting the possibility that Mtm1p imports Mn.

Attention shifted to iron metabolism when Yang *et al*. found that SOD2 was inactivated in Δ*mtm1* cells [54]. Their genetic and chromatographic results suggested the presence of an apo-Sod2p-reactive (ASR) pool of Fe in the matrix that competes with a pool of Mn ions in the same compartment for installation into the active-site of apo-Sod2p. Indeed, Fe misincorporates into bacterial superoxide dismutases, a process that prevents the apo-enzyme from being activated by Mn.[57] The size of the Mn pool in yeast mitochondria was hypothesized to vary with the concentration of Mn in the growth medium[53] while the size of the Fe pool was proposed to increase with the deletion of *mtm1*. Consistent with this idea, Δ*mtm1* cells contain an abundance of Fe.[54]

Naranuntarat *et al.* classified several mutant strains that are involved in ISC assembly and delivery into two groups, one participating in *early* ISC assembly pathway (*yfh1*, *isu1*) and the other participating in *late* ISC assembly pathway (*grx5*, *ssq1*, *atm1*).[55] All mutant strains have shown common phenotypes such as Fe overload, ISC/heme defects and oxidative damage. However, SOD2 activity is normal in *early* stage-mutant strains while it is low in *late* stage-ones, similarly in Δ*mtm1*. Based on unpublished data showing a loss of aconitase activity in the absence of Mtm1p and the common phenotypes, they suggested that Mtm1p plays a role in *late* stage in ISC assembly pathway. Also they claimed that the apo-Sod2p reactive Fe pool expands only when *late* stage proteins are mutated while *early* state proteins are normal.

Nutrient Signaling in Yeast and Relations to Fe Regulation and Stress Response

Yeast cells are generally grown on glucose as a carbon source and ammonium ion and amino acids as nitrogen sources. When these nutrients are limited, the global transcription patterns change (Figure I-3).[47] When depleted of glucose, cells undergo the diauxic shift to change energy metabolism from fermentation to respiration.[58] This process involves Snf1p, a protein kinase involved in expressing many respiratory and gluconeogenic genes.[47] Since many respiratory components require Fe cofactors, Snf1p induces the expression of Fe uptake genes by activating the Aft1 Fe regulon during diauxic shift.[59,60]

Nitrogen is essential not only for energy production but also for the biosynthesis of nucleotides, amino acids and proteins. When nitrogen is limited, cells retard their growth by lengthening the G1 phase of the cell cycle, which is under the control of the TOR (Target Of Rapamycin) pathway.[47] The TOR protein, a highly conserved protein kinase, is the central player in controlling the cell growth in accordance to nutrients levels.[61] This protein is a component of TORC1, a multiprotein complex that is inhibited by rapamycin, an immune-suppressive drug. The downregulation of TORC1, caused either by rapamycin treatment or starvation of carbon or nitrogen nutrients, induces numerous cellular responses. These include a decrease in protein synthesis, an increase in amino acid biosynthesis, the induction of autophagy, G_1 cell-cycle arrest and eventually entry into quiescence.[47,61,62]

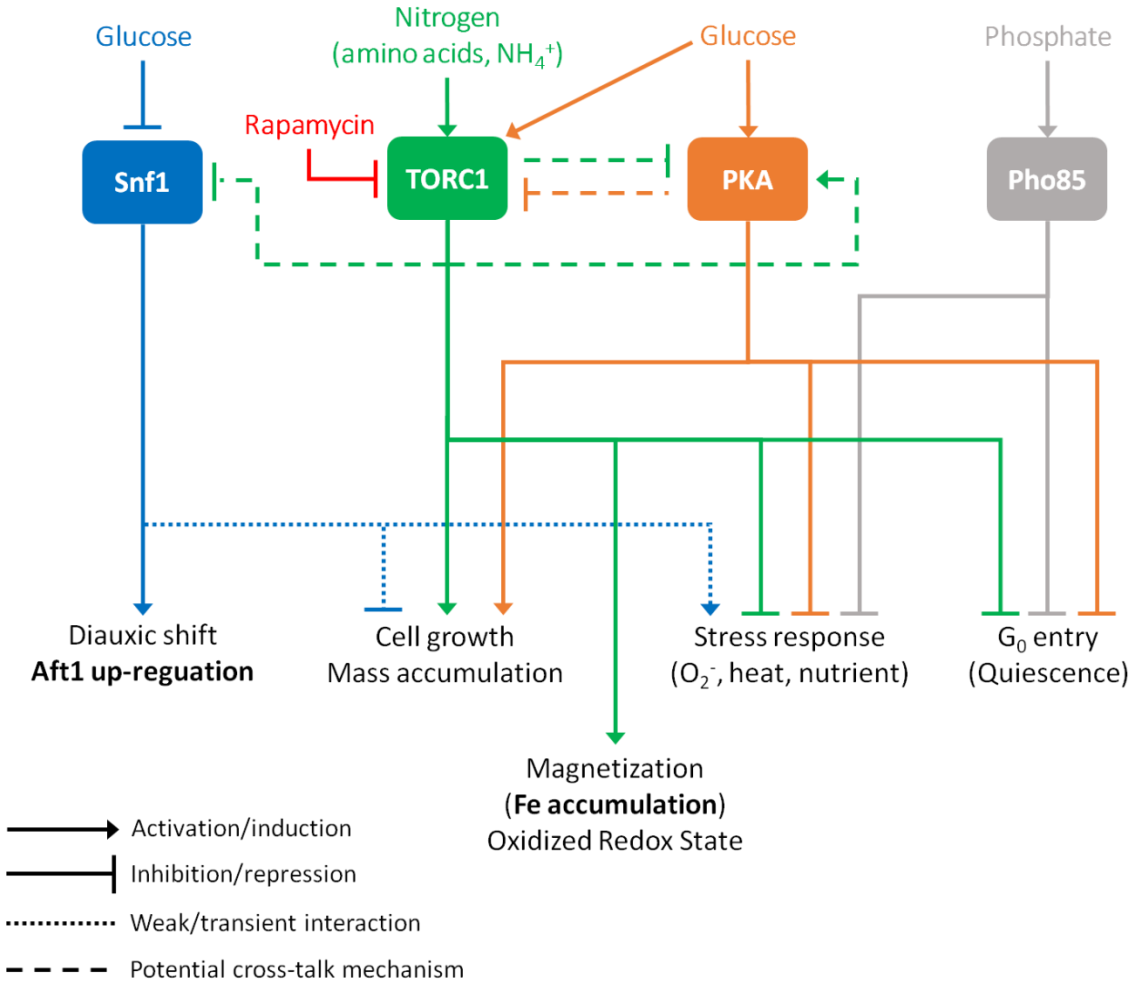

Figure I-3. Nutrient signaling pathway and its relation to Fe homeostasis in *Saccharomyces cerevisiae*.

TORC1 inhibition by rapamycin also decreases the magnetization of yeast cells grown on high Fe-containing medium, implying that TORC1 activity is important in cellular Fe acquisition.[63] Interestingly, both nutrients of carbon and nitrogen effect the magnetization of cells, but in opposite ways; glucose promotes magnetization while amino acids and nucleotides discourage it. TORC1 also plays a role in cellular redox control which is closely related to Fe homeostasis. Cells with the deletion of Tco89p, a component of TORC1, are more reducing, probably preventing Fe precipitation.

Stress-response genes are also tightly regulated by nutrient status via TORC1 and other pathways involving PKA (Protein Kinase A) and Pho85.[47] PKA helps regulate cell growth similar to the effect of TORC1. PKA is deactivated by the depletion of glucose; this leads to cell-growth-arrest and quiescence. Pho85p, a cyclin-dependent kinase, regulates the phosphate starvation response, which also promotes entry to quiescence. All three pathways repress Rim15p, a protein kinase controlling the expression of stress-response genes such as SODs and heat-shock proteins.

When cells are starved for nutrients, Rim15p activates stress-response genes that keep cells viable during quiescence. This extends the chronological life span (CLS) of rapamycin-treated cells.[64] Increased mitochondrial electron transport chain activity followed by increased ROS production due to reduced TORC1 signaling also extends CLS in a Rim15p-independent manner.[65]

Calorie restriction (CR) of yeast, which typically involves limiting glucose in the medium, also extends CLS by enhancing expression of stress-response genes.[66] The extension in CLS by CR is Rim15p-dependent but its mechanism may differ from that

involving TORC1, because CR has an additional effect on cells where the reduced TORC1 activity has already extended the CLS. Glucose-restricted cells accumulate less Fe than non-restricted cells.[67] Higher levels of Fe may promote oxidative stress in cells that are not glucose-starved.

Some yeast strains such as W303 are auxotrophic for several nitrogen-containing nutrients including adenine.[68] W303 contains a mutation in ADE2, which produces a protein catalyzing a step in *de novo* purine biosynthesis.[69] Adenine deprivation causes a toxic red adenine precursor to accumulate in vacuoles via glutathione (GSH)-mediated detoxification pathway.[70] Whether this detoxifying process influences Fe homeostasis is unknown. However, Cd^{2+} ions are effluxed into the vacuole by a GSH-mediated system.[71]

Integrative Approach to Investigate Fe Regulation and Trafficking in Yeast

The standard approach to studying Fe trafficking in biological systems relies on the phenotypic characterization of genetic constructs.[72] Recently, the Lindahl lab has employed Mössbauer spectroscopy, electron paramagnetic resonance (EPR) and electron absorption spectroscopies, in conjunction with inductively-coupled plasma mass spectrometry (ICP-MS) to characterize the phenotype of such strains.[73] Entire cells and isolated subcellular organelles can be studied. Anaerobic isolation prevents Fe oxidation. Packing organelles by centrifugation in a sample holder before the analysis maximizes signal intensity for spectroscopies. A method for determining the absolute concentrations of Fe species, not relative concentrations normalized by protein amount, was developed.

Mössbauer (MB) spectroscopy is a powerful tool enabling us to detect and characterize groups of Fe species in a cell or an organelle. A more informative name for this technique is *nuclear gamma-ray resonance*. Nuclei of ^{57}Fe in a sample, with the ground spin state I = ½ ,are promoted to the first excited spin state I = 3/2 by absorbing 14.4 keV gamma rays emitted by the decay of radioactive ^{57}Co (Figure I-4).[74] The energy of gamma radiation is slightly modulated, using the Doppler Effect, by moving the source back-and-forth relative to the sample. The resulting spectra are displayed as absorption intensity (%) on the y-axis vs. velocity (mm/sec) on the x-axis. Spectra are calibrated using α-Fe foil.[74]

MB spectroscopy can provide us information about spin and oxidation states of Fe center, relative amount of each Fe species, and coordination number and geometry via comparison with model complexes. Different spectral patterns are observed, depending on the spin and oxidation state of the Fe. A two-line pattern, called a quadrupole doublet, is due to the interaction of an electric field gradient with a quadrupole moment. A six-line pattern, called a sextet, arises from magnetic hyperfine interaction. Spectral features are also characterized by the isomer shift (δ) and quadrupole splitting (ΔE_Q) parameters. The spectral intensity is proportional to the ^{57}Fe concentration in the sample. Importantly, the percentage of intensity due to a given species is approximately equal to the percentage of ^{57}Fe associated with that same species in the sample probed. Another advantage of the technique is that all 57Fe species are observed – there are no "MB silent" species. The biggest disadvantages of MB spectroscopy are its low sensitivity (50 – 100 μM), cost of operation, and difficulty of

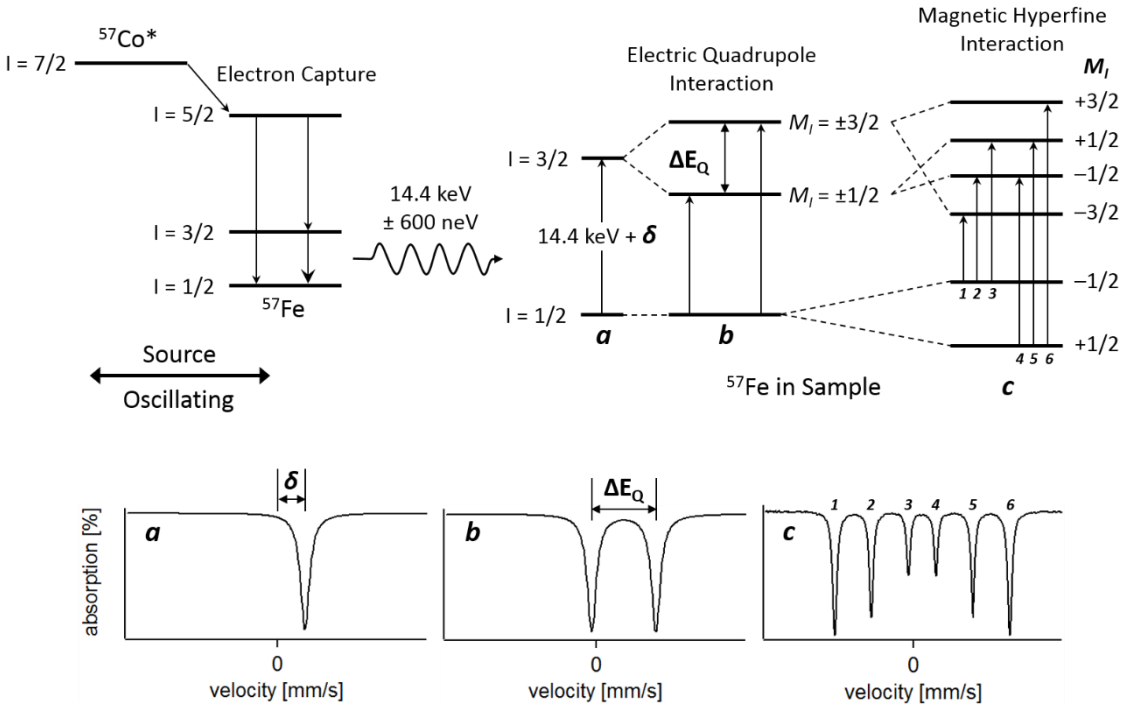

Figure I-4. Fundamental principle of Mössbauer spectroscopy.

analysis.

δ is basically determined by the s electron density at the nuclei; this parameters becomes larger as the density decreases.[75] δ of Fe^{II} ($3d^6$) nucleus is larger than that of Fe^{III} ($3d^5$) because of the increased shielding of the s electron through the increase in 3d valence electrons. ΔE_Q arises because the nucleus with I > 1/2 (^{57}Fe at the excited spin state, I = 3/2) has non-spherical electric charge distribution, producing a quadrupole moment.[75] In this condition, the excited spin state (I = 3/2) splits into two spin states m_I = ± 3/2 and ± 1/2, resulting in the two-line pattern with the energy splitting of ΔE_Q. ΔE_Q increases when the symmetry of the electric charge distribution becomes lower.

Typically high spin (HS) Fe^{II} has a higher ΔE_Q than HS Fe^{III}, because the electronic structure of $3d^6$ orbital is less symmetric than that of $3d^5$ in high spin state.

EPR spectroscopy detects transitions between the ground and excited spin states of unpaired electrons under the externally applied magnetic field. Most EPR spectrometers are X-band (9.5 GHz microwave radiation). The frequency is fixed as the static magnetic field sweeps between 0 and 0.5 T (5000 G).[76] Resonant absorption occurs when the transition energy is equal to the energy of the microwave radiation. Typically, the resulting signal is presented as first derivative of the intensity absorbed by the spin. Basically any paramagnetic systems, including $[Fe_4S_4]^+$ and oxidized hemes, can be studied by this technique. Each system can be identified by its spectral pattern and *g value* which is the effective Zeeman factor unique for each magnetic species. EPR spectroscopy is also a non-destructive method, and much more sensitive than MB spectroscopy, so that it can detect species at the low micromolar level.

Electronic absorption spectroscopy is used to measure heme concentration in whole cells and mitochondria. Heme a/a_3, *b* and *c* have absorption maxima at 605, 560 and 550 nm, respectively. Their extinction coefficients have been experimentally determined using heme-containing proteins,[77] so that absolute concentrations of heme centers can be determined.

ICP-MS is a highly accurate and sensitive technique to determine metal concentrations in organelles and cells. This technique allows detection of most of elements including all biometals such as Fe, Mn, Cu and Zn with a detection limit as low as ~ 10 part per trillion. To investigate Fe species present at low abundance in biological

systems, an on-line LC-ICP-MS system was built (by Sean McCormick, another student in the Lindahl lab) in Ar-atmosphere glovebox.[78] This novel setup allows Fe-containing species to be fractionated based on molecular weight, charge, hydrophobicity, etc. By maintaining anaerobic conditions during the sample preparation and separation, the oxidation of Fe is prevented, thereby minimizing possible ligand-exchange reactions.

Each technique described above has its own advantages and limitations, however, by integrating the results from whole cell and each subcellular organelle obtained by using all these techniques, we can obtain a snapshot of Fe distribution and speciation in biological systems to answer important questions about Fe trafficking and regulation mechanisms.

Objectives

One fundamental question in Fe trafficking pertains to how cells regulate Fe uptake during the different growth stages. This issue has been studied extensively using the genetic approach but only superficially using the biophysical and bioanalytical methods just described. Using these biophysical methods, Holmes-Hampton *et al.* has shown that wild-type (WT) yeast cells regulate cellular Fe when grown in medium containing 1 μM to 10 mM Fe.[35] However, Nishida *et al.* reported that WT yeast cells (with a slightly different genetic background) grown in medium containing 20 mM Fe are magnetized by forming large Fe deposits.[79] There were several differences between two studies but we hypothesized that the growth phase at the harvesting time was a critical (and unexplored) factor. In the former study, cells were grown to mid- or late

exponential phase, while in the latter cells were harvested at stationary phase. One objective of this dissertation was to examine the effect of growth mode on Fe regulation.

In addition, Nishida et al. demonstrated that higher-than-normal concentrations of the nitrogen sources in the growth medium diminished Fe magnetization while additional glucose increased it.[79] When they inhibited TORC1, magnetization was also diminished. These results supported known effects of calorie restriction (limiting glucose available in medium) on Fe accumulation. Reverter-Branchat et al. grew yeast cells on media with different carbon availability *for two months* and observed that cells grown on low glucose-medium accumulate much less Fe than those grown on high glucose-medium.[67] Thus, we decided to study yeast cells grown on different nutrient status using our integrative biophysical approach to probe the effects of nutrients on Fe regulation and speciation.

Finally, Culotta *et al*. hypothesized a pool of 'bioavailable' Fe in Δ*mtm1* mitochondria which was reactive to SOD2, inducing mismetallation and inactivation of the enzyme.[55] Previous studies of mitochondrial mutant strains (Atm1, Yah1, Yfh1, Aft1-up) demonstrated the accumulation of non-bioavailable Fe in the mutant mitochondrial.[80-83] We hypothesized that the bio-available Fe in Δ*mtm1* mitochondrial might be a pool of high-spin Fe^{II}. We considered that this pool might be the sought-after mitochondrial LIP. Therefore, a third objective of the dissertation was to characterize the bioavailable Fe in Δ*mtm1* mitochondria using our biophysical and bioanalytical techniques.

CHAPTER II

METHODOLOGY AND PROTOCOLS

Materials

Deionized (DI) water was prepared using Barnstead B-Pure^{TM} Triple (Double plus Single) holder systems (Thermo Scientific). It was used to prepare media and buffers. Ar (99.998%), O_2 (99.6%), N_2 (99.999%) and air (99%, 3 ppm moisture) gas cylinders were purchased from Praxair via the Texas A&M University Department of Chemistry Stockroom. ^{57}Fe metal (95% purity) was purchased from Cambridge Isotopes Laboratories, Inc. (Tewksbury, MA) or Isoflex (San Francisco, CA).

Yeast Strains

Saccharomyces cerevisiae strain W303-1B (*MATα, leu2-3, leu2-113, trp1-1, ura3-1, his3-11, his3-15, ade2-1, can1-100*)[84] was purchased from American Type Culture Collection (ATCC) and used as the wild-type strain in this study. DY150 FET3-GFP::KanMX (*MATa, leu2-3, leu2-113, trp1-1, ura3-1, his3-11, his3-15, ade2-1, can1-100*)[85] was used to visualize Fet3p-GFP. Δ*mtm1* and Gal-YAH1 strains were derived from W303-1B and Gal-YAH1 strain containing a galactose-inducible *YAH1* promoter.[86] Both strains were generously provided by Roland Lill (Institut für Zytobiologie, Philipps-Universität Marburg, Germany).

Media

Standard YPAD (YPAGal) with 2% (w/v) glucose (galactose) and 100 μM adenine hemisulfate dihydrate (MP Biomedicals, ICN10019525) agar plates were used as solid culture media. For liquid culture media, YPD, YPAD and synthetic minimal medium (MM) were prepared. MM consists of 1.7 g/L yeast nitrogen base from MP biomedical (#4027-112; which lacks $(NH_4)_2SO_4$, $FeCl_3$ and $CuSO_4$), 38 mM $(NH_4)_2SO_4$ (Fisher, A702-3), 1 μM $CuSO_4$, 2% (w/v) glucose, 760 μM leucine (MP Biomedicals, 194694), 130 μM histidine (MP Biomedicals, 101957), 240 μM tryptophan (Sigma-Aldrich, T0254), 100 μM adenine hemisulfate dihydrate, 180 μM uracil (MP Biomedicals, ICN10320425). ^{56}Fe- or ^{57}Fe-citrate from filter-sterilized 40 mM stock (pH ~ 5) was added separately to 20 or 40 μM final concentration. For nutrient effect studies, various MM-based media were prepared (*See* Table II-1 for definitions of media).

Growth

Cell stocks were prepared in 15% glycerol and stored at -80 ºC. As needed, frozen cells were scraped with a sterile wooded stick and spread onto a standard YPAD (YPAGal for Gal-YAH1) and grown for 3-4 days. For liquid culture, cells were usually grown to OD_{600} ~ 1 unless otherwise indicated.

For growth mode studies, single colonies were used to inoculate 50 mL YPD. Once grown, cultures were used to inoculate 1 L of YPAD and MM, such that the initial OD_{600} ~ 0.01. Both media were supplemented with 40 μM Fe and the endogenous concentration of Fe in YPAD was 8 ± 3 μM (n = 3), resulting in the final Fe

Table II-1. The Different Minimal-Medium-based media used in this study. The term *YNB* as used in the text consists of yeast nitrogen base *plus* $(NH_4)_2SO_4$.

Abbreviation	Description
MM	Minimal medium
A↓	8× less adenine
G↑	3× more glucose
G↓	10× less glucose
Fe↑	10× more Fe^{III}-citrate
G↑Fe↑	3× more glucose 10× more Fe^{III}-citrate
Y↑	3× more YNB
YAB↑	3× more YNB 3× more Leu, His, Trp ("amino acids") 3×more adenine and uracil ("bases")
AB↑	3× more amino acids 3× more bases
YAB↑G↑	3× more amino acids, 3× more bases 3× more glucose
YAB↑G↓	3× more amino acids 3× more bases 10× less glucose
RD+	200 μM rapamycin (VWR) dissolved in DMSO (EMD Millipore) and then added to media at 20 nM final concentration
D+	DMSO was added at the same concentration as in RD+ medium (0.01% v/v, final concentration).

concentration in YPAD ~ 50 μM. Cells were grown for 5 days at ~ 150 rpm and 30 ºC. Growth was monitored at OD_{600}. Cultured media were collected at different times by centrifugation at 2,500×g for 5 min. The resultant supernatants were used for measuringglucose concentrations in medium and the pellets were used to measure Fe concentrations in cell. Aliquots of cells were stored at -80 ºC for Western blot analysis, and packed into MB cups (hollowed Delrin cylinders, 12 mm o.d. × 10 mm)[73] or EPR tubes (4 or 5-mm outer diameter; 2.7 or 3.4-mm inner diameter; 80-mm long; Wilmad/Lab Glass, Buena, NJ, USA) at 4,000×g for 5 min, followed by freezing in liquid N_2. For mitochondria isolation, a whole 50 mL MM culture was transferred to 1 L of MM, and the whole 1 L culture was transferred to 24 L MM at 30 ºC in a stirred glass fermenter. Solutions were purged with O_2 at 1 L/min to achieve aerobic growth conditions. To prevent foaming, 100 ppm silicon antifoam B (Sigma-Aldrich, A6707) was added to the media. Cells were harvested after five days of growth and spun down at 5,500×g for 5 min.

For nutrient effect studies, cells were grown and harvested similarly as in growth mode studies, except that the YPD culture was used to inoculate 200 mL of MM-based media (Table II-1). Collected cells were used for Oxyblot, metal analysis, MB and EPR spectroscopies. Aliquots of cells were used for UV-Vis analysis. To isolate mitochondria and vacuoles from A↓ cells, 1 L (2 L for vacuoles) of MM culture was transferred to 24 L (48 L) of A↓ medium in the fermenter(s).

For Δ*mtm1* strain studies, Fe was added to 20 μM final concentration and some media were supplemented with 200 μM $MnCl_2$. For whole cell MB study and SOD2

activity assay, single colonies of WT, Δ*mtm1* and Gal-YAH1 strains were used to inoculate 200 mL MM. For mitochondria isolation, WT strain was grown on MM, while Δ*mtm1* strain was grown on YPAD up to 1 L scale and then switched to MM in 24 L scale. For anaerobic growth, MM was supplemented with 20 mg/L ergosterol (Acros Organics, AC11781) and 1.0 mL/L Tween-80 (Acros Organics, AC27863) dissolved in 1.0 mL/L ethanol, which was heated for 10 min in boiling water. Media were purged with Ar at ~ 1 L/min (~ 0.2 L/min for 200 mL cultures) to maintain anaerobicity.

Isolation of Mitochondria and Vacuoles

Pelleted cells were brought into refrigerated Ar-atmosphere glovebox (MBraun Labmaster, 3 – 8 ºC, O_2 < 10 ppm) and subcellular organelles were isolated as described.[46,73,87,88] Solutions used under anaerobic conditions were degassed on a Schlenk line and then brought into the box. Briefly, cells were first treated with 10 mM dithiothreitol for mitochondria or 5 mM TCEP-HCl (tris(2-carboxyethyl)-phosphine, Thermo Scientific, 20491) for vacuoles in 100 mM Tris-HCl (pH 9.4) buffer for 15 – 30 min. After rinsing with SP buffer (1.2 M sorbitol, 20 mM potassium phosphate, pH 7.4), cells were resuspended in SP buffer and added with 1,000 U lyticase (Sigma-Aldrich, L2524) per g of wet cell paste for 1 – 1.5 hr to convert cells > 80% to spheroplasts, followed by the centrifugation at 5,500×g for 5 min.

For mitochondria isolation, the lyticase-digested cells were rinsed twice with SP buffer and disrupted in SHP buffer (0.6 M sorbitol, 20 mM HEPES-KOH, pH 7.4, 1 mM PMSF) with Dounce Homogenizer (25 - 30 strokes). Non-disrupted cells were collected

by the centrifugation at 2,000×g for 5 min, followed by the second homogenization in SH buffer with 12 – 16 strokes and the centrifugation. Supernatant collected after each homogenization step was centrifuged at 15,000×g for 10 min to harvest crude mitochondria. Crude mitochondria were further purified by density gradient centrifugation. After resuspending in SH buffer, crude mitochondria were loaded on top of 16 – 21% Histodenz^{TM} (D2158, Sigma) discontinuous density gradients and centrifuged at 110,000×g (30,000 rpm) for 1 hr in an ultracentrifuge (Beckman Coulter Optima L-90K) with a swinging-bucket rotor (SW 32 Ti 32,000 RPM). Purified mitochondria were collected at the gradient interface and washed with SH buffer.

For vacuoles isolation, the lyticase-digested cells were resuspended in 15% Ficoll (Fisher BioReagents, BP525) buffer (15% Ficoll in 0.2 M sorbitol, 10 mM PIPES-KOH, pH 6.8) and was added with 100 μg/mL of diethylaminoethyl dextran (DEAE-Dextran, Sigma-Aldrich, D9885). The sample incubated for 3 min in ice bath and for 10 min in 32 ºC water bath. The lysate was sequentially overlaid with 8% Ficoll buffer and PS buffer, and centrifuged at 110,000×g for 1.5 hr. The crude material collected from the PS-8% interface was added with 15% Ficoll to make ~ 8% and overlaid with 4% Ficoll buffer and PS buffer. After another centrifugation, purified vacuoles were collected at the PS-4% interface and washed with PS buffer.

The isolated mitochondria were used for further analyses or packed into Mössbauer cups or EPR tubes at 24,600×g (12,000 rpm) for 30 min or 13,800×g (9,000 rpm) for 1 hr. A batch of isolated Δ*mtm1* mitochondria was packed in Mössbauer cup, treated with 1% sodium deoxycholate and then 10 mM sodium dithionite prior to

freezing. The isolated vacuoles were packed into those sample holders at 10,900×g (8,000 rpm) for 45 min. Packed samples were used to measure metal concentrations or frozen in liquid N_2.

Protein and Metal Content Analysis

Protein concentrations in whole cells and mitochondria were measured using the BCA protein assay kit (Pierce, 23227). Metal concentrations were measured by ICP-MS (Agilent 7700x). For BCA assay, packed mitochondria and whole cells were diluted with DI water up to 60-fold. For metal content assay, packed samples were diluted 2-4 fold with DI water. Then 50, 75 and 100 µL of the resulting suspensions were heated at 95 °C overnight in 200 µL of 30% trace-metal-grade HNO_3 and 100 µL of 35% trace-metal-grade HCl (both from Fisher Scientific). HCl was not used for nutrient effect study. Samples were diluted with 7.7 mL (7.8 mL for nutrient effect study) of distilled-DI water. Obtained metal concentrations were adjusted for dilution relative to the packed material, and by previously determined packing efficiencies of 0.70 for whole cells, 0.77 for mitochondria and 0.76 for vacuoles.[46,81] Resulting concentrations should reflect those present in mitochondria and whole cells.

Glucose Assays

Glucose concentrations in growth medium were measured using the Autokit Glucose (Wako Diagnostics, 439-90901) kit.[89] Culture medium was centrifuged at 16,000×g for 5 min to remove cells, and the supernatant was collected. 6.7 µL of cell-

free medium was added to 1 mL of the kit assay mix. After incubating the reaction mixture at 37 °C for 5 min, absorbance at 505 nm was measured. The absorbance due to a water-blank was subtracted. Glucose concentrations in the growth medium were calculated using a standard curve, adjusting for dilution factors.

SOD2 Activity Assays

Cells were grown on 200 mL of minimal medium containing 20 μM Fe-citrate. For 12 different batches, WT and Δ*mtm1* cells were harvested at OD_{600} between 0.6 – 1.8, matched to within 0.2 absorbance units for each pair of batches. Cells were harvested and lysed by glass-bead agitation.[53] For anaerobic growth, the medium was purged with Ar, and cells were harvested in the glovebox and processed under an Ar atmosphere. Cells were resuspended in lysis buffer containing 10 mM sodium phosphate (pH 7.8), 0.1% (v/v) Triton X-100, 5 mM EDTA, 5 mM EGTA, and 50 mM NaCl. An equivalent volume of 0.5 mm glass beads, 1 mM PMSF and 1% (v/v) protease inhibitor cocktail were added to cell suspensions. Cells were agitated by vortex action for 1 min and cooled on ice for $\geq$ 1 min; this procedure was repeated 6 more times. Lysate was clarified by centrifugation at 16,000×g for 10 min at 4 °C. The supernatant was passed through a 0.45 μm centrifuge tube filter (Millipore), and the filtrate was stored at 4 °C or in the glovebox.

The SOD activity gel assay was performed as described[90] except that 60 μg of whole-cell protein was loaded onto 12% Tris-HCl gels (Bio-Rad), and native gel electrophoresis was performed at 4 °C. The gel was soaked in a stain containing 50 mM

potassium phosphate (pH 8.2), 0.16 mM nitro blue tetrazolium (NBT), 0.27 mM riboflavin, 1 mM sodium cyanide, 6.7 mM TEMED (*N*,*N*,*N'*,*N'*-tetramethylethylene-diamine), and was incubated in the dark for 1 hr at 4 °C. The yellowish gel was exposed to light from a 40 W white bulb for 10 ~ 15 min to develop a blue background with colorless SOD bands. Gels were imaged by a Fujifilm LAS-4000 mini imaging system. The density of each band corresponding to SOD2 activity was quantified by using NIH ImageJ software and normalized to aerobically grown W303 activity.

Sod2p solution activity was measured by monitoring the reduction of NBT by a photochemical flux of O_2^{-}.[91] The reaction mixture was prepared in 330 µL of 50 mM potassium phosphate buffer at pH 7.8 containing 0.1 mM EDTA, by adding 10 µL of 90 mM NaCN, 33 µL of 1 mM NBT, 50 µL of 0.1 M methionine, and 10 µL of 0.16 mM riboflavin. Enzyme and water were added to a final volume of 1.0 mL. In the absence of enzyme, background formation of blue formazan was monitored at 550 nm after every 10 sec exposure to a 40 W white light bulb at the intensity required for the absorbance to increase at a rate of 0.05/min. One unit of SOD activity was defined by the amount of protein required to inhibit formazan formation by 50%.

Western Blots

Fet3p expression levels were measured in membrane-protein extracts prepared essentially as described.[92] Cell pellets were resuspended in an equivalent volume of extraction buffer (150 mM NaCl, 25 mM Tris-HCl (pH 7.4), 2% (v/v) protease inhibitor cocktail (Sigma-Aldrich, P8340) and 1 mM PMSF) followed by an equal volume of 0.5

mm glass beads (Biospec Inc.; 0.5 mm diameter). The mixture was vortexed for 1 min, and cooled on ice for ≥ 1 min. This procedure was repeated 3 more times. Glass beads and unbroken cells were removed by centrifugation at 2,500×g for 5 min; then homogenates were spun at 16,000×g for 30 min at 4 °C. Pellets were resuspended in buffer containing 25 mM Tris-HCl (pH 7.4) and 1% Triton-X, and were kept at 4 °C overnight. Resultant solutions were centrifuged at 16,000×g and 4 °C for 30 min. Supernatants were collected as a clarified extract.

Whole-cell lysates were obtained to determine Sod2p expression levels as described above except that the glass beads and unbroken cells were removed by centrifugation for 10 min. Resulting supernatants were collected as a purified extract. Whole-cell lysates were assayed by the Oxyblot method as described below. Protein concentrations in extracts were measured using the BCA protein assay kit (Pierce, 23227). 60 µg of extract proteins (16 µg for Sod2p assays) were resolved by 10% SDS-PAGE and transferred onto polyvinylidene fluoride membranes (Bio-Rad, 162-0218). For the Δ*mtm1* strain study, 60 µg of whole cell lysate or 20 µg of mitochondrial proteins were used. Membranes were blocked with 1% casein and incubated with an antibody against Fet3p or Sod2p. Developed membranes were imaged (FujiFilm LAS-4000 mini) and blot densities were Squantified by using ImageJ (National Institutes of Health) software. Unless noted otherwise, densities were normalized based on the highest intensity band.

Oxyblot Assay

Whole-cell lysates and mitochondrial extracts were solubilized with 6% (w/v, final concentration) SDS and then mixed 1:1 with the 2,4-dinitrophenylhydrazine (DNPH) solution included in the Oxyblot assay kit (Millipore, S7150). DNP-derivatized proteins were resolved by SDS-PAGE followed by Western blot. Blot membranes were visualized using an antibody against DNP. The level of oxidative stress was quantified by densitometry.

Fe/S Cluster-Containing Enzyme Assays

Aconitase assays were performed essentially as described.[80] Isolated mitochondria were solubilized in a buffer consisting of 20 mM Tris (pH 7.4) and 0.5% (v/v) Triton-X 100. 20 μL of solubilized mitochondria was mixed with 40 μL of 0.1 M Tris (pH 7.4), 40 μL of 0.5 M NaCl, and 80 μL of deionized H_2O in a 1 mm path length quartz cuvette. 20 μL of 10 mM sodium cis-aconitate (Sigma-Aldrich, A3412) was added to the mixture to initiate the reaction. The consumption of cis-aconitate was monitored by a decrease of OD_{240}. The reaction rate was calculated from the linear part of the slope assuming a molar extinction coefficient of 3.6 mM^{-1} cm^{-1}.[93] Activities were expressed as units per mg protein; 1 unit is defined as 1 nmol of aconitate converted per min.

Leu1p assays were performed as described.[94] Cells were grown on minimal medium with 30 mg/L leucine (to increase Leu1p expression level) and were harvested at OD_{600} of 0.7 ~ 0.8. 50 mL of cell culture was centrifuged and the pellet was washed

with ice-cold deionized water and resuspended in 0.3 mL of lysis buffer (20 mM KH_2PO_4 buffer, pH 7.2, 50 mM NaCl, 1 mM EDTA, 0.5 mM PMSF). Glass bead agitation was performed as above with 6 cycles of 30 sec-vortex and 30 sec-cooling on ice. Lysate was clarified by centrifugation at 10,000×g for 5 min. 50 µL of supernatant was immediately mixed with 50 µL of 0.2 M KH_2PO_4 (pH 7.0) buffer, 395 µL of deionized water, and 5 µL of 0.1 M sodium citraconate (Sigma-Aldrich). The decrease in OD_{235} was monitored for 3 min and the reaction rate was calculated from the initial slope assuming a molar extinction coefficient of 4.7 mM^{-1} cm^{-1}.[95] Activities are reported as units per mg protein, with 1 unit defined as 1 nmol of citraconate converted per min.

Succinate dehydrogenase (SDH) assays were performed essentially as described,[96] but modified as follows. Isolated mitochondria were diluted to 7 mg/ml protein concentration with 0.6 M sorbitol and 20 mM HEPES, pH 7.4. The reaction mixture consisted of 100 mM Tris-HCl (pH 8.3), 0.5 mM EDTA, 2 mM KCN, 2 mM iodonitrotetrazolium chloride (INT) (Sigma-Aldrich, I8377), 12 g/L Cremophor EL, and 20 mM sodium succinate, previously adjusted at pH 8.3. The reaction was initiated by adding 10 µL of mitochondrial suspension to 990 µL of the reagent at 30 ºC. Color development by INT-formazan was monitored at 500 nm for 6 min. The reaction rate was obtained from the linear part of the initial slope assuming a molar extinction coefficient of 19.3 mM^{-1} cm^{-1}.[96] Blank experiments were performed in the absence of sodium succinate and the resulting background rate was subtracted from the sample rates. Activities were determined as units per mg protein (1 unit is defined as 1 nmol of INT-formazan formed per min).

Mössbauer Spectroscopy

Low field MB spectra were collected at Texas A&M University using two sets of an instrument consisting of a Model MS4 WRC spectrometer (SEE Co., Edina, MN), a 4.5 to 300 K closed-cycle helium refrigerated system and a W106 temperature controller. Applied magnetic fields were parallel to the γ-radiation. High field MB spectra were collected at Carnegie Mellon University with a spectrometer using Janis Research Super-Varitemp dewar, capable of generating 0-8 T fields or at Texas A&M University with a Model LHe6T spectrometer, capable of generating 0-6 T fields (SEE Co.). Spectra were calibrated using an α-Fe foil and analyzed using WMOSS software package (SEE Co.)

EPR Spectroscopy

EPR spectra were recorded on X-band EMXplus^{TM} spectrometers (Bruker Biospin, Billerica, MA) at University of Texas, Arlington and Texas A&M University. Spectra were simulated with SpinCount (ver. 3.0.13, http://www.chem.cmu.edu/groups /hendrich/facilities/index.html) and signal intensities were quantified relative to 1 mM CuEDTA spectrum obtained at 0.2 mW and 10 K or 0.02 mW and 10 K. Some spectra were re-scaled on SpinCount using the 'T-scale' function which multiplies signal-intensity by temperature.

UV-Vis Spectroscopy

Packed cells and mitochondria were resuspended in an equal amount of DI water and SH buffer, respectively. 200 μL of the cell (mitochondria) suspension was transferred aerobically (anaerobically) to a custom 2 mm pathlength quartz UV-Vis cuvette (NSG Precision Cells, Inc.). Spectra were obtained using a Hitachi U3310 spectrometer with a Head-On photomultiplier tube. The cell suspension was scanned 6 times and the results were averaged to improve the signal-to-noise ratio. Resultant absorbances were normalized to that expected if a 10 mm pathlength cuvette had been used.

LC-ICP-MS Experiments

In the first group of experiments, isolated mitochondria were resuspended in 10 mM HEPES (pH 7.2) containing 1 mM PMSF, and sonicated 3 times for 30 sec each with a Branson 450 sonifier at a 60% duty load using a two-step microtip. The suspension was pelleted at 18,000×g for 30 min and the soluble mitochondrial layer was collected. For the first LC-ICP-MS experiment of this group, the pellet was resuspended in buffer, and the second soluble fraction was collected after centrifugation and combined with the first soluble fraction. For the second and third experiments of this group, the second soluble fraction was not combined. Extracts (2 mL injections) were passed through a Superdex 200pg 16 × 600 mm column (GE Life Science) equilibrated in 25 mM Tris-HCl pH 7.7. Buffer was prepared in double-distilled deionized trace-metal-free water. The elution flow rate was 0.75 mL/min, controlled by an ÄKTA (GE

Healthcare Life Science, New Jersey, USA) FPLC. The entire system was housed in a refrigerated (5^{o} C) Ar-atmosphere glovebox (Mbraun) with $O_2 < 3$ ppm as monitored by a Teledyne Model 310 analyzer.

The second group of LC studies involved size-exclusion chromatography of LMM species. Isolated mitochondria were solubilized with 1% sodium deoxycholate in 100 mM Tris at pH 7.4, and the supernatants were filtered through 10 kDa cut-off membrane using an Amicon stirred concentrator. The filtrates were applied (0.5 mL injections) to two Superdex Peptide 16 × 300 mm columns (GE Life Science) connected in series and equilibrated with 25 mM Tris-HCl pH 7.7, driven by a Bio-Inert HPLC (Agilent, Tokyo, Japan). The elution flow rate was 0.375 mL/min. The entire system was located within a refrigerated glovebox. The third group of LC studies involved anion-exchange chromatography (Mono Q 4.6/100 PE GE Healthcare; 1.7 mL column volume CV) of mitochondrial extracts. Extracts were prepared as described above for HMM size-exclusion studies involving sonication, except that the sonication buffer was 20 mM Tris pH 7.2. Buffer A (20 mM Tris pH 7.2) and buffer B (same as A but with 1 M NaCl) were used to generate the elution buffer gradient. The column was washed with 8 CVs of Buffer A. Proteins were eluted using 25 CVs of a 0 $\rightarrow$ 1 M NaCl linear gradient, followed by 8 CVs of Buffer B. For the second study, Buffer C (20 mM Tris pH 7.2 plus 0.1 M NaCl) and Buffer D (same as C but with 0.35 M NaCl) were used as the elution buffer. The column was washed with 5 CVs of Buffer A. Proteins were eluted using 3 CVs of Buffer C, followed by 25 CVs of a linear 0.1 $\rightarrow$ 0.35 M NaCl gradient, and then

5 CVs of Buffer D. The elution flow rate was 1 mL/min. The Bio-inert HPLC was used for these studies.

Aqueous Fe^{III} and many other Fe^{III} complexes are insoluble at neutral pH and tend to adhere to column media. Fe^{II} is easily oxidized to Fe^{III} in air, and even under essentially anaerobic conditions, Fe accumulated on our LC columns. Thus, after each use, the size-exclusion columns were cleaned by passing 5 CVs of a chelator cocktail containing 10 μM each of EGTA, EDTA, diethylenetriamine pentaacetate, and 2,2-bipyridine followed by 10 CVs of elution buffer. (WARNING: Early attempts to use 10 mM of the same chelator cocktail seemed to damage the column media.) This was followed by 15 CVs of elution buffer. The Mono Q column was cleaned by passing 15 CVs of 20 mM Tris plus 1 M NaCl, then 15 CVs of 10 μM EGTA and EDTA, followed by 10 CVs of 20 mM Tris (without NaCl).

The ICP-MS was used in collision cell mode (He: 4.3 mL min^{-1}) with platinum cones and skimmer. The instrument was optimized daily using manufacturer's tuning solution. The sample was introduced through a standard Micromist nebulizer (Glass Expansion, Australia). For size-exclusion chromatography, the eluent was split using a micro splitter valve (Upchurch Scientific, USA) with ~ 30% directed to ICP-MS and the remainder to the ÄKTA 950 fraction collector where 500 μL fractions were collected in Deep Well 96 well plates (Greiner, Germany). For anion exchange chromatography using the on-line ICP-MS, ~ 80% of the eluent was collected in 680 μL fractions using a 1260 Infinity Analytical-Scale Fraction Collector (Agilent, Tokyo, Japan). The

remaining ~ 20% of the eluent was sent to ICP-MS. ^{56}Fe, ^{57}Fe, ^{55}Mn, ^{31}P, and ^{34}S were monitored with a dwell time of 100 ms.

CHAPTER III

LACK OF IRON REGULATION IN *SACCHAROMYCES CEREVISIAE* DURING POST-EXPONENTIAL GROWTH MODES

Introduction

The redox-active transition metal iron plays fundamental roles in enzyme catalysis, electron transfer processes, small-molecule binding and activation. It is found in various forms, including Fe/S clusters, heme centers, nonheme mono- and dinuclear complexes, among others. Fe can also be deleterious to cells, as certain forms participate in Fenton chemistry that generate ROS which can, in turn, damage DNA, proteins, and membranes.[5] Thus, rigorous Fe regulation is expected to be a critical aspect of cellular Fe metabolism.

The molecular-level details of Fe trafficking and regulation are best understood in the budding yeast *Saccharomyces cerevisiae*. Major "traffic hubs" in Fe metabolism include the mitochondria and vacuoles, but the plasma membrane, cytosol and nucleus also play important roles.[9,10] The plasma membrane contains numerous proteins that import Fe from the environment. The membrane-bound Fet3p/Ftr1 complex constitutes the "high affinity" Fe importer.[14] Genes encoding these and about 20 other Fe-related proteins in the cell are controlled by Aft1p/Aft2p.[6] These transcription factors are sensitive (via a partially understood mechanism) to the concentration of unidentified Fe-containing species in the cytosol.

There is at least one low-affinity Fe import pathway composed of the plasma membrane proteins Fet4p.[21] Fet4p is induced by Aft1p in response to low medium Fe levels.[20] Fet4p levels are also sensitive to low Zn which is regulated in the cell via Zap1p, a Zn-regulated transcription factor.[20] Smf1p is another plasma membrane protein that may constitute a second low-affinity Fe importer. It is a divalent metal transporter that primarily transports Mn, but can also transport Fe^{II} with low affinity.[23]

Much cytosolic Fe is sent to the mitochondria as these organelles are the primary site of Fe/S cluster assembly and heme biosynthesis. The cytosolic Fe used for these processes is imported via the mitochondrial inner-membrane proteins Mrs3p/4p.[31] Many of the Fe-containing prosthetic groups that are generated in the mitochondria are installed into respiratory complexes.

Excess cytosolic Fe is transported into vacuoles, which store and sequester the metal, and which can mobilize Fe as needed by the cell. Ccc1p is the only known Fe importer located on vacuolar membrane, though Fe can also be imported via endocytosis.[42] Yap5p is an Fe-sensing transcription factor that regulates the transcription of *CCC1* mRNA in response to cytosolic Fe.[43] *CCC1* mRNA is also regulated by Cth1/2p; the binding of these proteins under Fe-limited conditions destabilizes the message thereby preventing its translation.[44] The dominant form of Fe in the organelle is a mononuclear high-spin (HS) Fe^{III} complex with polyphosphate-related ligands.[46]

Like all biological systems, yeast are commonly viewed as able to tightly regulate the import and trafficking of all cellular metabolites,[97] yet such cells reportedly accumulate Fe continuously during two months in glucose-containing media.[67] To

understand this phenomenon better, we used Mössbauer (MB) spectroscopy and ICP-MS to monitor the Fe content of yeast grown to various stages on rich medium (YPAD) and on minimal medium (MM). Exponentially growing cells maintained a constant level of cellular Fe due to a balance between cell growth and Fe import rates. However, in glucose-deficient post-exponential growth phases, Fe accumulated in cells as HS Fe^{III} (found in the vacuole) and as Fe^{III} oxyhydroxide nanoparticles. These effects were mimicked semi-quantitatively by a simple mathematical model. Surprisingly, the extent of cellular oxidative stress was not linked directly with Fe accumulation.

Results

Fe accumulation in rich medium (YPAD)-grown cells

We wanted to evaluate the Fe concentration and content of yeast grown in batch culture and harvested at different stages, including exponential and post-exponential growth modes. W303 cells grown on YPAD supplemented with 40 μM ^{57}Fe citrate grew exponentially with a doubling time (DT) of ~ 1.5 hr (Figure III-1A, circles). After *ca*. 10 hr, cells transitioned to a slow-growing state with a DT of ~100 hr. The glucose concentration in the culture (Figure III-1A, triangles) remained high during exponential growth, but declined dramatically during the transitionary period, such that the culture was virtually devoid of glucose during the slow-growth period. The observed diauxic growth pattern reflects a shift from fermentation to respiration.[98]

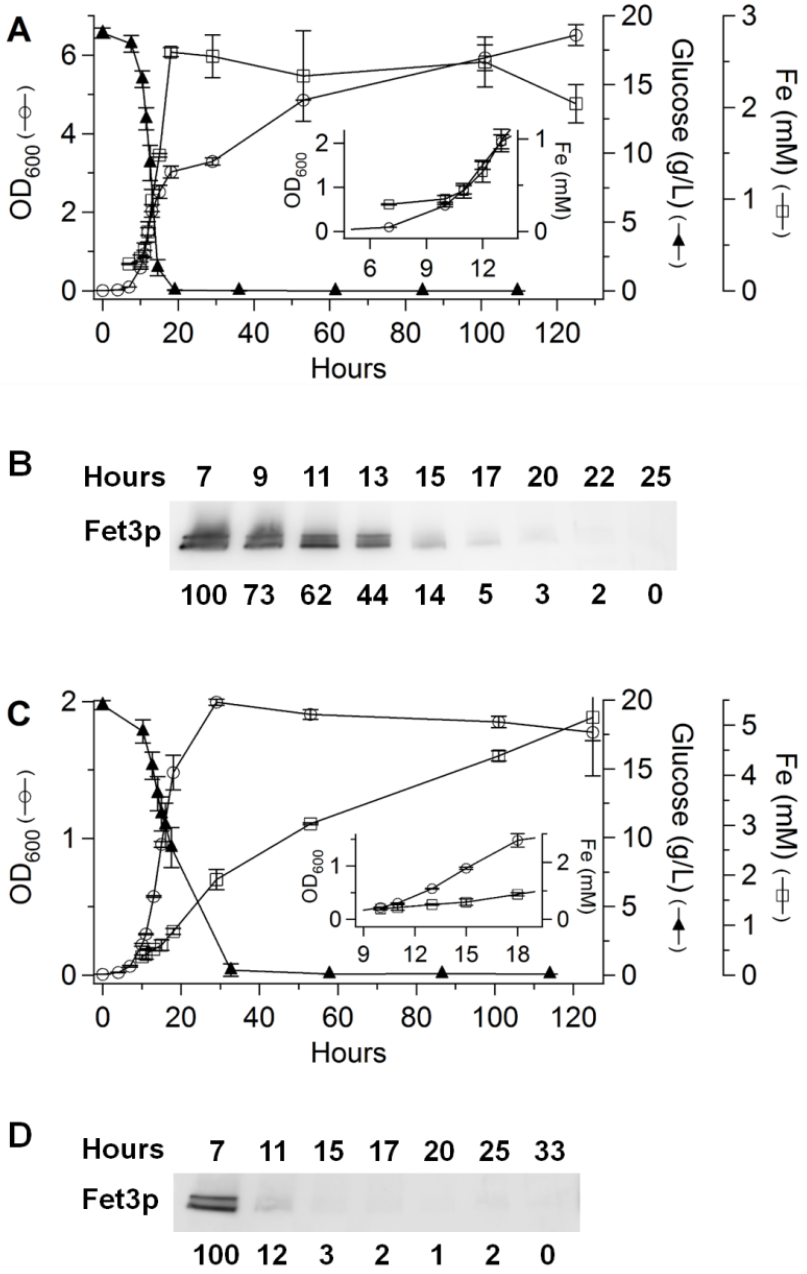

Figure III-1. Chronological profile of nutrient, growth and Fe-associated parameters for cells grown in batch culture on YPAD (A and B) and MM (C and D). A, OD (circles), glucose concentration (triangles), and cellular Fe concentration (squares); B, Fet3p expression level; C and D, same as A and B but for MM. *Insets* in A and C are close-up views of 5-13 hr (for A) and 9-18 hr (for B) regions. Reported iron(glucose) concentrations were the average of two(three) independent experiments. Bars indicate standard error. Relative band intensities in B and D are indicated below the blots.

The concentration of Fe in the growing cell was also monitored, starting 4 doublings (~7 hr) after inoculation (Figure III-1A, squares). The Fe concentration during exponential growth was *ca*. 300 μM (measured at OD = 0.1) and stayed at the similar level throughout to 11 hr (400 μM at OD = 1.0, Figure III-1A, *inset*). It increased during the transitionary period at a rate of *ca*. 300 μM Fe/hr and then plateaued at 2 – 2.5 mM in the slow-growth state. With a DT of ~ 100 hr, this implies a constant slow-growth Fe import rate of ~ 30 μM/hr.

We hypothesize that the accumulation of Fe during the transitionary period arose from a mismatch of Fe import and cell growth rates. Accordingly, during exponential growth, the rates were matched such that the cellular Fe concentration was constant. During the transitionary period, the Fe import rate(s) declined slower than the cell growth rate declined, resulting in the accumulation of Fe. Once in the slow-growth mode, the rates were again matched, resulting in slow-growing cells with a time-independent Fe concentration.

Our hypothesis accounts for the results *semi-quantitatively*. If exponentially growing cells contained 300 μM Fe, and their DT was 1.5 hr, the Fe import rate should be 200 μM Fe/hr. If cells stopped growing while the Fe import rate remained unchanged, they should accumulate Fe at this rate (not at 300 μM/hr as measured). If cells grew with a DT > 1.5 hr, they should still accumulate excess Fe but at a slower rate. Despite these minor discrepancies, we favor this hypothesis because of its simplicity; alternatives would seem to require that Fe import rates increase during the transitionary period and

then decrease during the following slow-growth state; we find such complicated scenarios unappealing.

The Fet3p expression level, which reflects the activity of the high-affinity Fe import system, was also monitored. Expression was maximal during exponential growth (7 hr) but it declined gradually during the transitionary period and became undetectable during the slow-growth period (Figure III-1B). These changes can also be explained by our hypothesis, by assuming that Fe enters exponentially growing cells primarily through the high-affinity plasma-membrane Fe import system. Since Fet3p is essentially not expressed in slow-growth cells, the slow-growth Fe import rate probably reflects the low-affinity Fe import system.

Fe accumulation in minimal medium (MM)-grown cells

The same parameters were monitored for cells grown on MM. These cells grew more slowly during exponential phase (DT ≈ 2.0 hr) (Figure III-1C, circles). They transitioned at an $OD_{600} \approx 2$ to a true stationary state rather than to a slow-growth state. MM-grown cells consumed glucose more slowly, but the development of the transitionary period still correlated with a decline in glucose concentration (Figure III-1C, triangles). The Fe concentration in exponentially growing MM cells (400-600 μM at OD 0.2-1.0, Figure III-1C, *inset*) was slightly higher than that observed for YPAD-grown cells while the rate of maximal Fe import during the transitionary period (100 μM/hr) was lower (Figure III-1C, squares). Our hypothesis can again account for these results semi-quantitatively. However, a DT of 2 hr and a Fe concentration of 400 μM in

exponentially growing cells imply an Fe import rate of 200 μM/hr, double the observed rate. Nevertheless, we continue to favor our hypothesis because alternatives are less appealing.

The Fe concentration of MM-grown cells that just entered the stationary state was 2-3 mM, similar to that of YPAD-grown cells. Unlike YPAD-grown cells, ***MM-grown cells continued to accumulate Fe when in the stationary state***, such that they contained *ca*. 5 mM Fe after ~ 100 hr in this state. This corresponded to an average rate of 40 μM Fe/hr. This *stationary-state Fe import rate* was similar to the slow-growth Fe import rate of YPAD-grown cells. Both probably originated from Fe entering via the low-affinity Fe import system which likely dominates during post-exponential growth modes.

Fet3p expression in MM-grown cells was maximal during exponential growth (at 7 hr) and declined rapidly thereafter (Figure III-1D). With 40 μM Fe in the medium, we find it remarkable that the high-affinity Fe import system was expressed at all; no Fet3p expression was previously observed in MM-grown cells harvested during late exponential or early transitionary phase (OD ~ 1.2).[19] When cells are grown in Fe-adequate medium, the high-affinity system might only be expressed during early exponential growth. Our hypothesis can explain the faster rate of FET3 shutdown along with the slower rate of growth shutdown and a similar concentration of Fe in YPAD- and MM-grown cells at the end of the transitionary period. Accordingly, the high-affinity transporter is proposed to shut-down in closer synchronization with the decline in growth rate. This might be due to a more gradual decline in growth rate in MM-grown

cells such that the slow kinetics involved in shutting-down the high-affinity Fe import system would not create a significant mismatch in rates.

Zn efflux from the cell during the growth

This buildup of Fe in these cells was specific for Fe as neither Cu, Mn nor Zn ions accumulated. However, the concentration of Zn declined during the transition from exponential to stationary growth modes (Figure III-2). The decline was gradual in YPAD- grown cells (Figure III-2, squares) but dramatic in MM-grown cells (Figure III-2, circles). If yeast cells contain a Zn efflux pump (e.g. homologous to ZnT1, a mammalian Zn efflux protein[99]) it may activate during post-exponential growth. Alternatively, Zn influx pathways may shut-down as cell growth slows.

Whole cell Mössbauer spectra of yeast

We next used Mössbauer (MB) spectroscopy to evaluate the form(s) of Fe that accumulated in yeast grown to high culture densities on YPAD and MM. The 5 K low-field MB spectrum of YPAD-grown cells harvested in late exponential phase (OD = 2.1) (Figure III-3A) was dominated (79% of spectral intensity) by a sextet assigned to a mononuclear HS Fe^{III} species located in vacuoles.[46] The brown line above the spectrum simulates this feature.

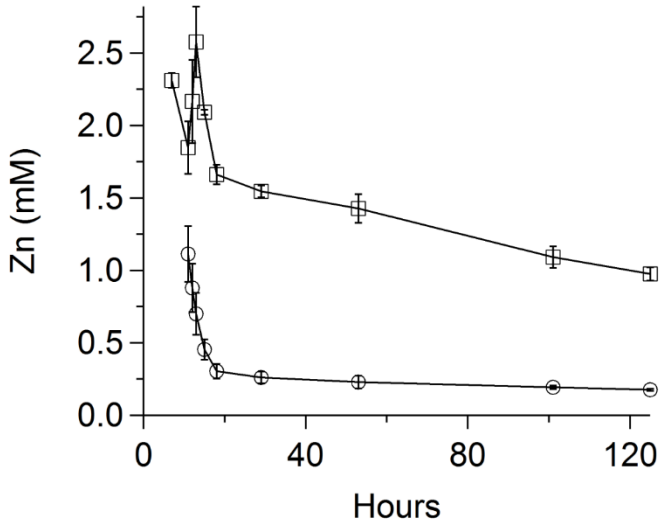

Figure III-2. Chronological profile of Zn concentrations in cell (sqaure, YPAD; circle, MM). Reported Fe concentrations are the average from two independent experiments (matched with Fe data) and error bars indicate standard error.

The spectrum also exhibited a quadrupole doublet from nonheme high-spin (NHHS) Fe^{II} ions (8%, purple line) and the so-called *central doublet* or CD (9%, green line). The latter feature arises from S = 0 $[Fe_4S_4]^{2+}$ clusters plus low spin (LS) heme Fe^{II} ions (the two types of species cannot be distinguished).[35] A minor contribution from HS Fe^{II} hemes (3%, yellow line) could also be discerned. The CD and heme components are due primarily to mitochondrial respiratory complexes. The location of the NHHS Fe^{II} species has not been established. Fitting parameters and associated cellular Fe concentrations are given in Table III-1.

The MB spectrum exhibited by YPAD-grown cells harvested in the transitionary period (at OD = 3.2) exhibited the same general features (Figure III-3B), as well as a

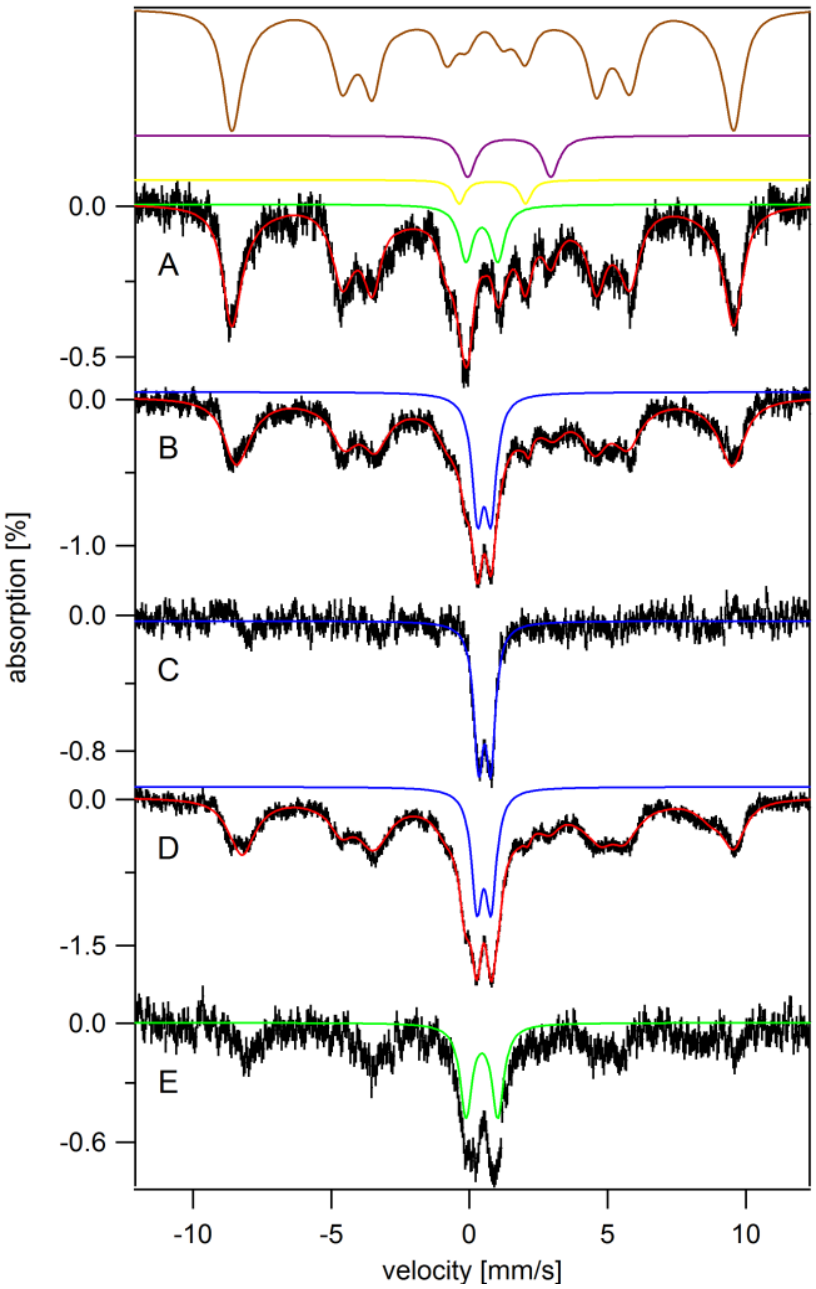

Figure III-3. 5 K Mössbauer spectra of whole yeast cells grown on YPAD and harvested at various time points. A 40 mT field was applied parallel to γ-rays. A, exponential phase (OD 2.1); B, transitionary phase (OD 3.2); C, B-minus-A difference spectrum; D, post-diauxic growth phase (OD 8.0); E, D-minus-B difference spectrum. Red lines simulate collectively the spectral features associated with HS Fe^{III}, NHHS Fe^{II}, HS Fe^{II} heme, CD, $[Fe_2S_2]^{2+}$, and Fe^{III} nanoparticles. Brown, purple, yellow, green and blue lines are simulations of HS Fe^{III}, NHHS Fe^{II}, HS Fe^{II} heme, the central doublet, and Fe^{III} nanoparticles, respectively.

Table III-1. Isomer shift (δ, mm/s), quadrupole splitting (ΔE_Q, mm/s), line width (Γ, mm/s) and percentage of Fe species as determined from Mössbauer spectra used in Chapter III. For HS Fe^{III}, A_{iso}, D, E/D, η values were also listed. Parameters were averaged from all spectra presented in this paper, but some parameters ($\delta/\Delta E_Q/\Gamma$) were listed separately if they were apart from the averaged numbers. *Percentages of signals with broad range of A values (Fe aggregates) was estimated based on the intensity left after subtracting all assignable signals from original spectra. Bold-style parameters were fixed when simulated.

Spectrum (**Total [Fe]**)	Non-heme HS Fe^{III}	Non-heme HS Fe^{II}	HS Fe^{II} heme	Central doublet	Fe^{III} nano-particles
A_{iso} (kG)	232 ± 2	-	-	-	-
δ (mm/s)	0.55	1.39 ± 0.05	0.91 ± 0.05	**0.45**	**0.53**
ΔE_Q (mm/s)	0.42	3.02 ± 0.10	2.31 ± 0.09	**1.15**	**0.50**
Γ (mm/s)	0.34	0.70 ± 0.11	0.32 ± 0.11	**0.60**	**0.46**
D (cm^{-1})	0.15	-	-	-	-
E/D	0.21	-	-	-	-
η	1.3	-	-	-	-
YPAD/OD 2.1 Fig. 2A **(700 µM)**	79%	8%	3%	9%	-
YPAD/OD 3.2 Fig. 2B **(1000 µM)**	67%	7%	-	3%	19%
Fig. 2B – 2A Fig. 2C **(~ 300 µM)**	37%	-	-	-	63%
YPAD/OD 8.0 Fig. 2D **(1500 µM)**	66%	5%	-	9%	19%
Fig. 2D – 2B Fig. 2E **(~ 500 µM)**	53%	-	-	29%	18%
MM/OD 0.2 Fig. 3A **(430 µM)**	76%	3%	3%	15%	-

Table III-1. Continued

Spectrum (**Total [Fe]**)	Non-heme HS Fe^{III}	Non-heme HS Fe^{II}	HS Fe^{II} heme	Central doublet	Fe^{III} nano-particles
MM/OD 1.2 Fig. 3B **(620 µM)**	73%	8%	-	13%	4%
MM/OD 1.8 Fig. 3C **(1500 µM)**	68%	11%	-	10%	10%
Fig. 3C – 3B×2 Fig. 3D **(~ 300 µM)**	32%	39%	-	-	29%
MM/OD 1.8 /5 days Fig. 3E **(8100 µM)**	72%	-	-	-	12%
400Fe/OD 2.2 /5 days Fig. 3F **(28.4 mM)**	9%	-	-	-	0.54/0.65/0.80 53% (< 30%)*
MM/OD 1.7 /5 days/6 T Fig. 4A **(4900 µM)**	72%	-	-	-	Unknown parameters 15%
Same as Fig. 3F, but at 6 T Fig. 4B **(28.4 mM)**	9%	-	-	-	Unknown parameters > 90%
MM/OD 1.8 /5 days mitochondria Fig. 4 **(220 µM)**	-	-	-	15% ($[Fe_2S_2]^{2+}$, 30%)	0.54/0.60/0.40 40%

new quadrupole doublet (19%, blue line) with parameters ($\delta \approx 0.53$ mm/s, $\Delta E_Q \approx 0.50$ mm/s) typical of Fe^{III} (phosphate/polyphosphate-associated) oxyhydroxide nanoparticles. The Fe concentration of these cells was higher than those harvested at OD = 2.1 (1.0 mM vs. 0.7 mM). The bulk of the additional Fe was present as nanoparticles, as evidenced by the difference spectrum of Figure III-3C.

YPAD-grown cells harvested 3 days later in the slow-growth state (OD = 8.0) exhibited a similar MB spectrum (Figure III-3D) but with ~ 50% higher percent effect, consistent with the higher concentration of Fe in the sample (1.5 mM). The difference spectrum (Figure III-3E, slow-growth minus transitionary) revealed that the additional Fe was mainly in the form of the CD and mononuclear HS Fe^{III}. The absolute concentration of central doublet Fe in YPAD-grown slow-growth cells was two-fold higher than in transitionary cells (Table III-1). The generation of more mitochondrial Fe for cells in the slow-growth phase is consistent with the greater use of respiratory complexes after the diauxic shift.

The MB spectrum of MM-grown cells harvested in exponential phase (OD = 0.2) exhibited a similar distribution of Fe as in YPAD-grown cells, except that the percentage of Fe due to the CD was slightly higher (15% of spectral intensity) (Figure III-4A). MM-grown cells harvested at later stages of exponential growth (Figure III-4B, OD = 1.2) exhibited virtually the same spectrum. This is evidence that *the distribution of Fe in the cell is constant during exponential growth phase*. A similar distribution has been reported for cells harvested towards the end of exponential growth (at OD ~ 1.0).[19,78]

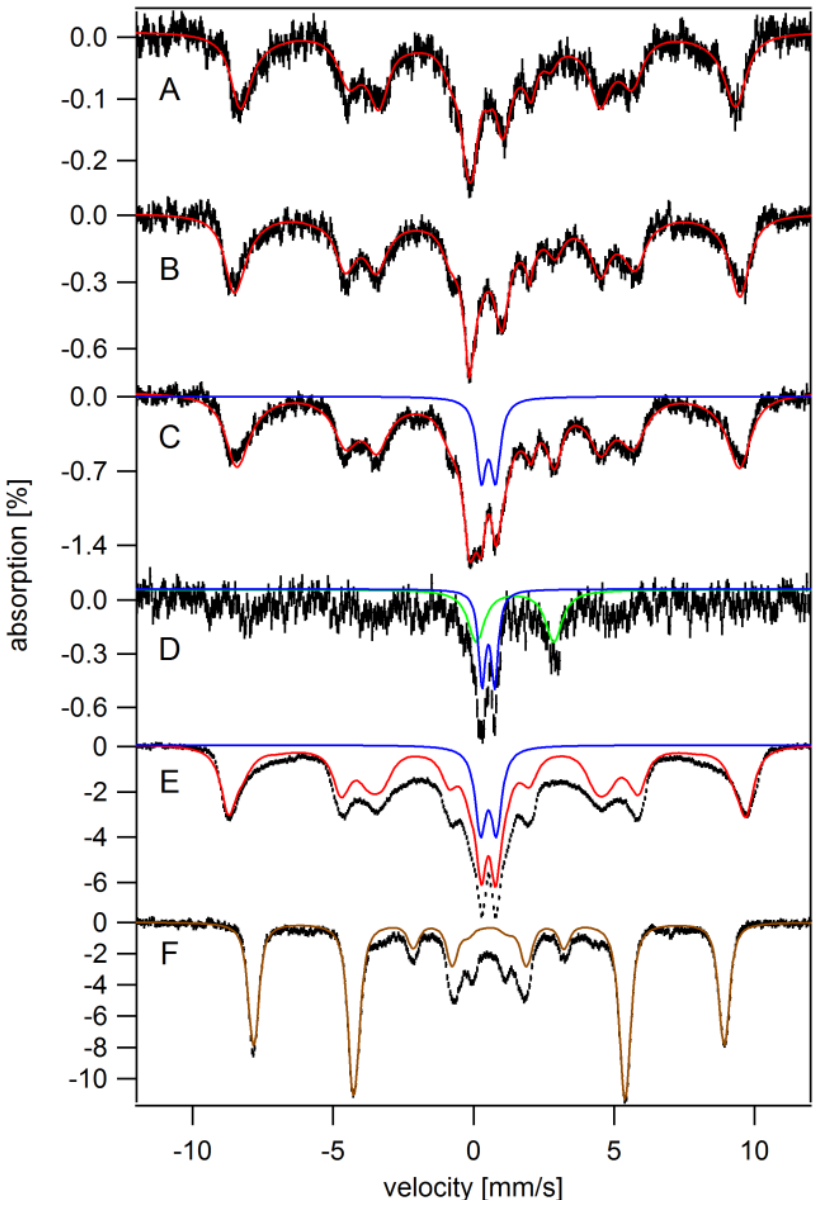

Figure III-4. 5 K Mössbauer spectra of whole yeast cells grown on MM and harvested at various time points. A 40 mT field was applied parallel to γ-rays. A, early exponential phase (OD 0.2); B, exponential phase (OD 1.2); C, transit-ionary phase (OD 1.8); D, C-minus-B difference spec-trum (the spectral intensity of B was doubled and then subtracted from C) E, stat-ionary phase (OD 1.8, 5-day-grown); F, an equivalent sample of E (OD 1.7, 5-day-grown) at 6 T, 4.2 K. Red lines simulate most of the Fe spectral features including HS Fe^{III}, NHHS Fe^{II}, HS Fe^{II} heme, CD, $[Fe_2S_2]^{2+}$, and Fe^{III} nanoparticles. Blue and green lines indicate the simulation of Fe^{III} nanoparticles and HS Fe^{II}, respectively. The brown line simulates HS Fe^{III} assuming $S = 5/2$, $D = 0.15$ cm^{-1}, $E/D = 0.21$, $A_0/g_N \cdot \beta_N = -233$ kG, $\delta = 0.55$ mm/s, $\Delta E_Q = 0.42$ mm/s, and $\eta = 1.3$.

The Fe distribution of MM-grown cells changed as the cells moved into the transitionary phase (Figure III-4C). Overall spectral intensity increased due to the higher Fe concentrations in these cells. The difference spectrum (Figure III-4D, transitionary minus exponential) revealed that the primary forms of Fe that accumulated were Fe^{III} nanoparticles and NHHS Fe^{II} (and some mononuclear HS Fe^{III}). This caused the percentage of Fe due to the CD in these spectra to decline; however, the absolute concentration of the CD increased somewhat.

The MB spectrum of 5-day MM-grown cells in stationary phase (Figure III-4E) was intense, consistent with the tremendous buildup of Fe evident in Figure III-1C at 120 hr. The primary form of Fe that accumulated was mononuclear HS Fe^{III} originating from vacuoles. The absolute concentration of Fe^{III} nanoparticles also increased, but percentagewise there was no increase. After removing the contributions from these two dominating components, the residuals suggested some broad unresolved Fe. We collected a 100 K spectrum in hopes that this feature would collapse into a doublet, as is observed for ferritin iron[100], but it did not (Figure III-5). We collected the low-temperature 6 T MB spectrum of an equivalent sample (Figure III-4F) to overcome any spin-spin interaction due to high Fe concentration and to better characterize this elusive species. However, the spectrum was dominated (72% of overall intensity) by the HS Fe^{III} sextet, such that a low-intensity broad unresolved species could not be discerned.

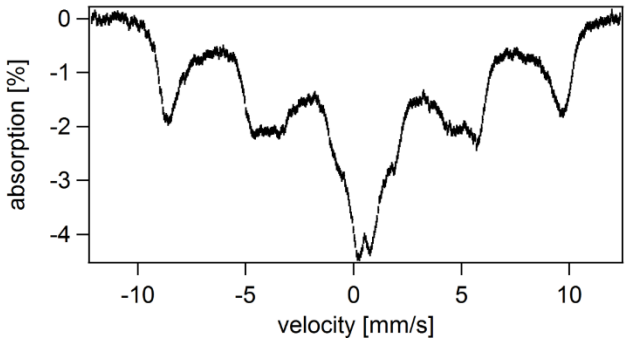

Figure III-5. 100 K Mössbauer spectrum of 5-day-grown cells on MM.

Characterization of the Fe^{III} nanoparticle-like feature

The EPR spectrum of an equivalent sample (5-day old MM-grown WT cells harvested at stationary state) did show some evidence for such a species. The spectrum exhibited a derivative-like feature at g ~ 2.0 along with an intense signal at g = 4.3 (Figure III-6 A). The latter signal arose from a HS Fe^{III} species with rhombic symmetry and is associated with the sextet in the MB spectrum of Figure III-4E. The novel g ~ 2 signal was reminiscent of the broad signal originating from Fe^{III} (phosphate/polyphosphate) oxyhydroxide nanoparticles found in the mitochondria of various ISC mutants.[80,83] However, the lineshape and temperature-dependence were different. The new signal exhibited inverse Curie Law behavior but the effect was less dramatic relative to that observed in previously characterized ISC mutant nanoparticles. Fortunately, the Curie Law behavior of the g = 4.3 signal (the product of intensity•temperature remained constant as the temperature varied) allowed us to use this signal as an internal control. Although we have not characterized this new species further, we suspect that it is a somewhat different form of Fe^{III} nanoparticles relative to

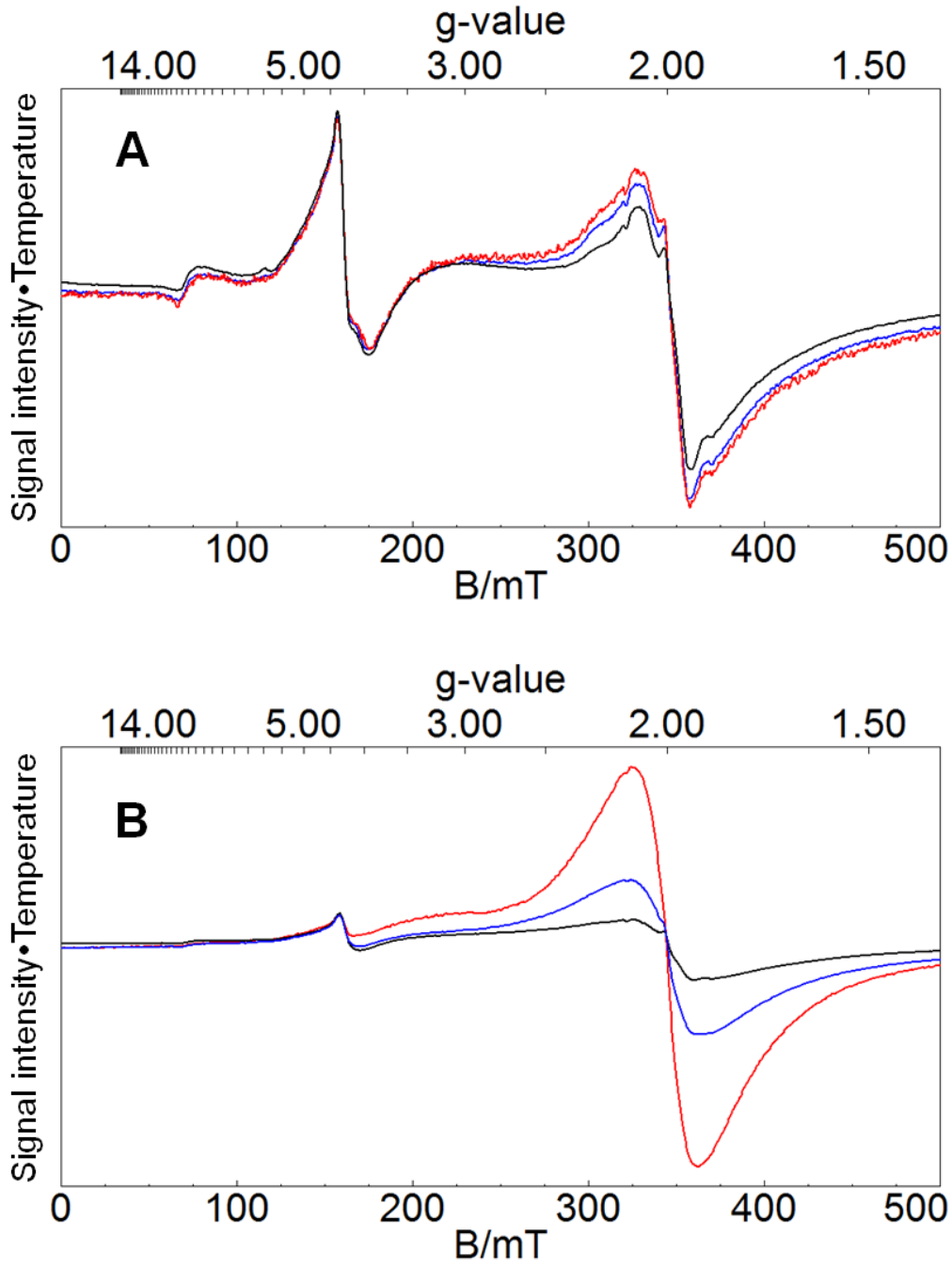

Figure III-6. EPR spectra of 5-day grown cells on MM containing 40 and 400 μM Fe at varied temperatures. A, 40 μM Fe; B, 400 μM Fe. Black, 10 K; blue, 30 K; red, 80 K. Spectra were recorded at 0.05 mW microwave power, 9.64 GHz frequency and 10 Gauss modulation amplitude, and then have been adjusted vertically so that the g = 4.3 resonances are aligned.

that which affords a broad quadrupole doublet in low-field, low-temperature MB spectra of ISC-mutant mitochondria.[80,82,83]

The MB spectrum of cells grown on MM that contained 400 μM ^{57}Fe (10 times normal) was more intense than the corresponding spectrum of cells grown with 40 μM ^{57}Fe in the medium, and the lineshape was different (Figure III-7A). The sample contained ~ 28 mM Fe, *ca*. 3.5 times higher than the Fe concentration of cells grown on MM that contained 40 μM ^{57}Fe. About half of the spectral intensity was present as nanoparticles (recognized by the broad poorly resolved doublet in the center of the spectrum at low field), while only ~ 9% was present as mononuclear HS Fe^{III} (Figure III-7A). Subtracting these two features afforded a broad unresolved magnetic feature between -5 and +7 mm/s representing ~ 30% of the original spectral intensity (Figure III-7B). This is probably similar to the broad low-intensity feature in Figure III-4E that could not be characterized well. The 6 T MB spectrum (Figure III-7C) was broad and poorly resolved. Approximately 90% of spectral intensity arose from Fe^{III} nanoparticles while much of the remaining intensity was due to mononuclear HS Fe^{III}. HS Fe^{III}-subtracted difference spectrum (Figure III-7D) revealed a broad nanoparticle-like feature, distinct from the 6 T MB spectrum of mitochondrial nanoparticles (Figure III-7D, dotted line). We are unable to decompose the spectrum further, but suspect that this sample contains more than one type of Fe^{III} oxyhydroxide nanoparticles.

EPR spectra of equivalent cells also exhibited anti-Curie Law behavior (Figure III-6B). These spectra also had to be normalized based on g = 4.3 signal to observe the increase in the broad g ~ 2.0 signal as the temperature increases. The increase of g ~ 2.0

signal intensity in these spectra was much more dramatic compared with them of cells grown on MM with 40 μM Fe (Figure III-6B vs. III-6A). This implies that the unique anti-Curie Law behavior can be used as a marker for the Fe^{III} nanoparticles formed in aged yeast vacuoles and the increment in the signal intensity is proportional to the concentration of the nanoparticles.

MB spectrum of mitochondria isolated from aged cells

Mitochondria were isolated from 5-day-old MM-grown cells in stationary state to determine whether they contained nanoparticles. The yield was low because cell walls were thick and difficult to break. The sample exhibited the MB spectrum shown in Figure III-7E. The overall percent effect was very low, with about 40% of spectral intensity due to nanoparticles and about 45% due to CD and possibly $[Fe_2S_2]^{2+}$ clusters.[19] This indicates that nanoparticle do not accumulate in stationary-state WT mitochondria to anywhere near the extent that they do in mitochondria from Fe/S cluster mutant strains.[80,82,83] The majority of nanoparticles present in MM-grown whole WT cells harvested in stationary stage are probably *NOT* located in mitochondria.

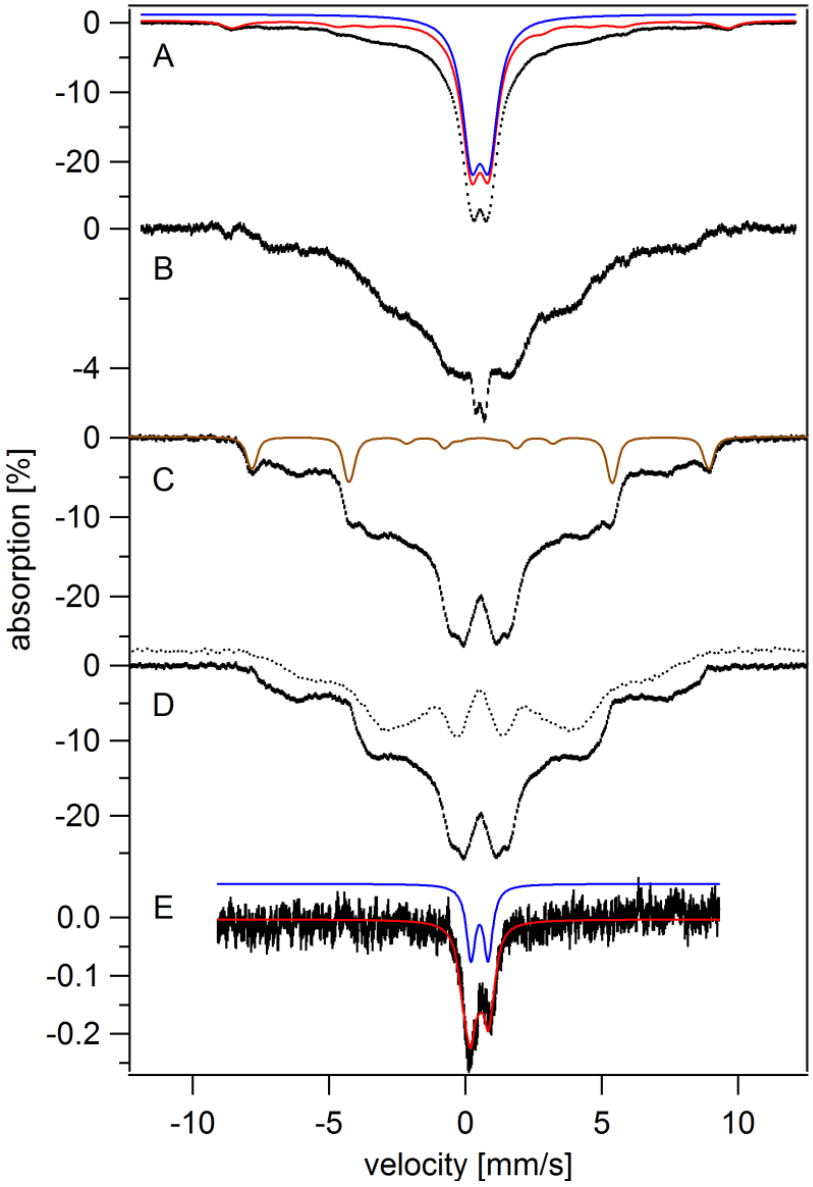

Figure III-7. Mössbauer spectra of MM-grown yeast cells and isolated mitochondria at stat-ionary phase. Top, Mössbauer spectra, A, 400 μM Fe-cont-aining MM-grown cells at stat-ionary phase (OD 2.2, 5-day-grown) at 40 mT, 5 K; B, same as in A but HS Fe^{III}- and Fe^{III} nanoparticles-subtracted; C, same as in A but at 6 T, 4.2 K; D, same as in C but HS Fe^{III}-subtracted; E, mitochondria isolated from 5-day MM (40 μM Fe)-grown cells (OD 2.2). Dotted line is MB spectrum of isolated mitochondria from Aft1-1^{up} cells.[81] Applied fields in A and E were parallel to the γ-radiation, while one in C was perpendicular to the radiation. Brown and blue lines indicate HS Fe^{III} and Fe^{III} nanoparticles, respectively. The red line simulates the most of Fe spectral intensity including HS Fe^{III}, Fe^{III} nanoparticles, CD and $[Fe_2S_2]^{2+}$.

Oxidative stress in post-exponentially grown cells

Cells grown on YPAD for 5 days exhibited a similar level of oxidative damage compared with cells grown on the same medium for 1 day (Figure III-8A, lane 2 vs. 1). This was unexpected given the higher Fe concentration in the 5-day-old cells. More surprisingly, cells grown on MM for 5 days experienced 3-times ***less*** oxidative damage than comparable 1 day old cells (Figure III-8A, lane 4 vs. 3). This was unexpected because MM-grown cells in stationary state contained much higher Fe concentrations than did MM-grown cells harvested in exponential and transitionary phases. We conclude that *Fe concentration alone is not an accurate predictor of ROS damage*. The growth medium and duration of growth on the medium may also play important roles.

We considered that the higher ROS level in slow-growing YPAD cells resulted because these cells were respiring (and thus generating more ROS), whereas 5-day old MM-grown cells were less metabolically active; perhaps MM-grown cells were unable to undergo the diauxic shift and respire due to a lack of essential nutrients found in YPAD. Cellular Sod2p levels are up-regulated during the diauxic shift.[101] To examine whether MM-grown cells also undergo this shift, we quantified the level of Sod2p in YPAD-grown *vs*. MM-grown cells. Over the course of 5 days of growth, Sod2p band intensities in both YPAD- and MM-grown cells gradually increased (Figure III-8B). The Sod2p level in YPAD-grown cells in stationary state was increased 10-fold relative to the same cells during exponential growth (Figure III-8B, YPAD, 120 *vs*. 9 hr). The Sod2p level in MM-grown cells also increased, in this case 7.5-fold, between exponential and stationary phases (Figure III-8B, MM, 120 *vs*. 9 hr). We conclude that

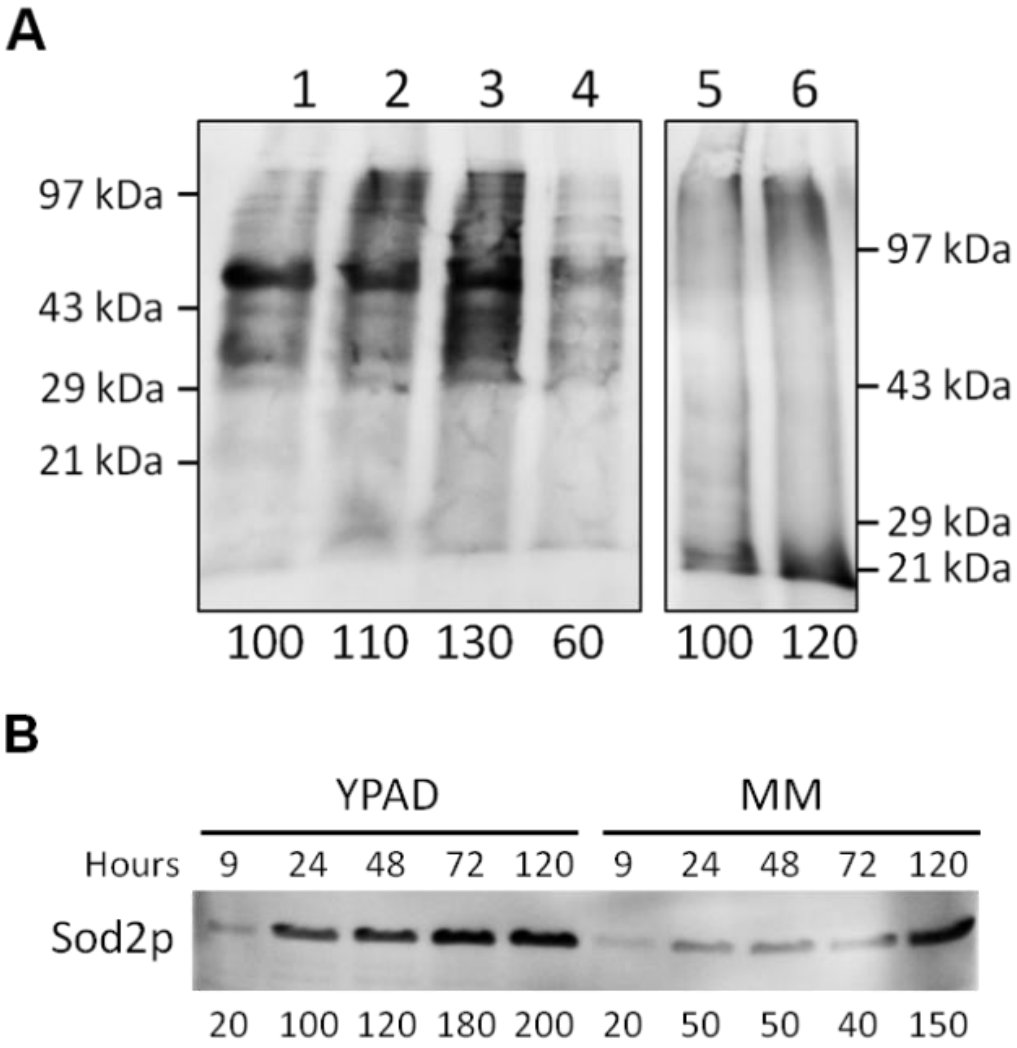

Figure III-8. Oxyblot assay and Western blot against Sod2p of whole cells and mitochondria harvested at different conditions. A, Oxyblot assay. Lane 1-2, YPAD; lane 3-4, MM; lane 5-6, MM/mitochondria; odd-numbered lanes, 1-day-grown cells; even-numbered lanes, 5-day-grown cells. Band intensities relative to that of the MM/1 day blot are shown on the bottom of each lane. B, Western blot against Sod2p. Lane 1-5, YPAD; lane 6-10, MM; growth hours labeled on the top of each lane. Band intensities relative to that of the YPAD/1 day blots are shown on the bottom of each lane. Each lane was developed with 4 (Oxyblot for whole cell lysates), 15 (Oxyblot for mitochondrial extracts) and 16 (Western blot against Sod2p for whole cell lysates) μg of protein.

like YPAD-grown cells, MM-grown cells also shift their metabolism from fermentation to respiration when glucose is depleted. This is supported by the slightly increased level of oxidative stress in mitochondria isolated from 5- vs. 1-day-old MM cells (Figure III-8A, lane 6 vs. 5).

Model development for cellular Fe regulation and trafficking

We have developed 2 mathematical models to explain our results. In both, Fe is imported into the cell via *HI* (high affinity) and *LO* (low affinity) pathways, with corresponding import fluxes R_{HI} and R_{LO}. As illustrated in Figure III-9, Fe from the growth medium can enter the cell through either pathway. Imported cytosolic Fe (Fe_C) is trafficked exclusively to mitochondria and vacuoles, at independent rates. The cellular location of the nanoparticles that form in WT cells is uncertain, with either vacuolar or cytosolic location assumed by each model. The model in which nanoparticles are generated in the cytosol is called "C" while that in which they form in the vacuoles is called "V".

The rate of Fe import via *LO* is considered to be constant under all growth conditions. *HI* is homeostatically regulated by the surrogate function *Reg*.

$$\mathrm{Re}\,g_{-} = \frac{1}{1+\left(\frac{[Fe_c]}{K_I}\right)^s}$$

such that the import rate is reduced when $[Fe_C]$ exceeds a setpoint concentration called K_I. Fe_C can be viewed as binding cooperatively to a negative effector site on an *HI* import protein. In that case, K_I would represent the dissociation constant associated with

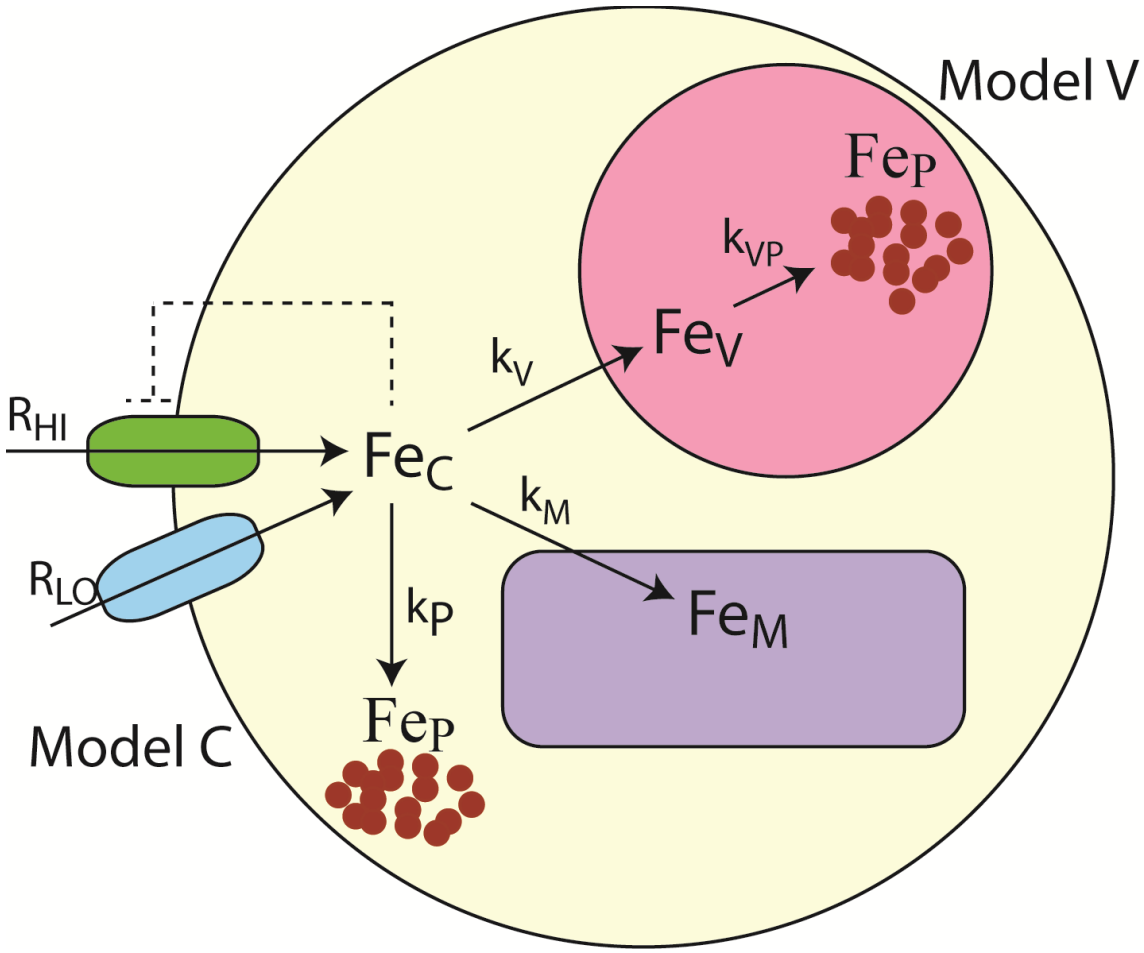

Figure III-9. Model of Fe metabolism in yeast cells. For model V, Fe^{III} nanoparticles were assumed to form in vacuole. For model C, Fe^{III} nanoparticles were assumed to form in cytosol. Fe_C, cytosolic Fe; Fe_V, vacuolar Fe; Fe_M, mitochondrial Fe; Fe_P, Fe^{III} nanoparticles; R_{HI}, high affinity Fe uptake rate; R_{LO}, low affinity Fe uptake rate; k_V, vacuolar Fe influx rate-constant; k_M, mitochondrial Fe influx rate-constant; k_P, Fe^{III} nanoparticle formation rate-constant in cytosol; k_{VP}, Fe^{III} nanoparticle formation rate constant in vacuole. Dotted line indicates the negative feedback of high affinity Fe uptake system by cytosolic Fe.

that process. Alternatively, K_I could reflect a transcription factor (e.g. Aft1p) binding to, for example, the iron regulon promoter in an Fe-dependent fashion. The developed models cannot distinguish these possibilities.

Cellular Fe concentration is determined by a balance between the rate of Fe import via the two transport systems and the cell growth rate α. For simplicity, α was assumed to equal 1/DT. The ordinary differential equation (ODE) describing changes in $[Fe_{cell}]$ is

$$\frac{d[Fe_{cell}]}{dt} = R_{HI}\left(\frac{1}{1+\left(\frac{[Fe_C]}{K_I}\right)^s}\right) + R_{LO} - \alpha[Fe_{cell}]$$

where *s* is a sensitivity factor (set to 3 in our calculations). When $[Fe_C] > K_I$, import is inhibited relative to when $[Fe_C] = K_I$; when $[Fe_C] < K_I$, import is stimulated. Under stationary state and slow-growth conditions, the models assume that *LO* dominates Fe import such that

$$\frac{d[Fe_{cell}]}{dt} \approx R_{LO} - \alpha[Fe_{cell}]$$

For slow-growth on YPAD, we have $0 \approx R_{LO} - \frac{1}{100}[2500]$ such that R_{LO} ~ 25 μM Fe/hr. For stationary state on MM, $40 \approx R_{LO} - 0$ such that R_{LO} ~ 40 μM/hr. These values are approximations; for simplicity, we assumed R_{LO} ~ 30 μM Fe/hr. Assuming that both *HI* and *LO* operate during exponential phase and that $[Fe_C] = K_I$,

$0 = R_{HI}\left(\frac{1}{2}\right) + 30 - \frac{1}{1.5}[300]$ so $R_{HI} \approx 340$ μM/hr. For MM-grown cells, a similar calculation affords a similar value of R_{HI}.

Cellular Fe (Fe_{cell}) was divided into 4 components, including cytosolic, vacuolar (Fe_V), mitochondrial (Fe_M) and nanoparticles (Fe_P); thus $[Fe_{cell}] = [Fe_C] + [Fe_V] + [Fe_M] + [Fe_P]$. In Model V, nanoparticles are generated in the vacuole from Fe_V whereas in Model C, nanoparticles are generated in the cytosol from Fe_C. For Model V

$$\frac{d[Fe_C]}{dt} = R_{HI}\left(\frac{1}{1+\left(\frac{[Fe_C]}{K_I}\right)^s}\right) + R_{LO} - \left(k_V + k_M + \alpha\right)[Fe_C]$$

$$\frac{d[Fe_V]}{dt} = k_V[Fe_C] - (k_{VP} + \alpha)[Fe_V]$$

$$\frac{d[Fe_M]}{dt} = k_M[Fe_C] - \alpha[Fe_M]$$

$$\frac{d[Fe_{VP}]}{dt} = k_{VP}[Fe_V] - \alpha[Fe_{VP}]$$

A similar set of ODE's was constructed for Model C (Figure III-11). Both sets were solved numerically using Maple 17 (Maplesoft Inc) software. Parameters k_V, k_M, k_P, and α were manually adjusted to match the concentrations indicated by the MB spectra shown in Figures III-3, 4 and 7, and to match the kinetic behavior and Fe concentrations of Figure III-1. Final parameter values and simulated concentrations for different conditions are given in Table III-2. Simulations for exponential growth on both YPAD

and MM media, as well as for slow-growth conditions on YPAD and stationary state conditions on MM are shown in Figure III-10.

Although simple, the models capture essential behavior of global Fe metabolism in *S. cerevisiae* cells. They illustrate the relationship between growth rate, cellular and organelle import rates, cellular Fe concentrations, and predict the distribution of that Fe into four major groups observed by MB. Model parameters indicate that the rate-constants for Fe import into mitochondria and vacuoles are reduced 10 - 100 fold. These reductions occur in synchrony with the slowing of the growth rate from a DT of ~ 2 hr to ~ 100 hr or longer (i.e, stationary state). Thus, ***the cell appears to regulate these import rates in accordance with its overall growth rate***. The rate of nanoparticle formation behaves oppositely. During exponential phase, nanoparticles did not form whereas during slow or stationary growth modes, the rate of nanoparticle formation was significant.

The two models exhibited similar (but not identical) behavior in this regard and so neither can be cleanly eliminated. However, we favor Model V for the following reasons. First, nanoparticles have been observed in MM-grown WT cells in vacuoles[46] whereas there is no clear evidence that nanoparticles form in the cytosol. Secondly, the simulations of nanoparticle concentration *vs*. growth time by Model V (Figure III-10, brown lines) showed a time-delay whereas the analogous simulations by Model C (Figure III-11, brown lines) did not. This delay allowed Model V to more accurately simulate the data.

Table III-2. Parameters for simulations. For both models, R_{HI} = 340 μM/hr, K_I = 30 and *s* = 3. Subscripts: D = composite data, V = Model V, and C = Model C. Concentrations are in μM.

	$[Fe_{cell}]$	$[Fe_V]$	$[Fe_M]$	$[Fe_C]$	$[Fe_P]$	k_V (hr^{-1})	k_M (hr^{-1})	k_{vp} (hr^{-1})	R_{LO} ($\mu M/hr$)	α (hr^{-1})
YPAD, Early Exp.	300_D 303_V 339_C	236_D 227_V 235_C	40_D 47_V 77_C	24_D 29_V 27_C	0_D 0_V 0_C	5.3_V 5.8_C	1.1_V 1.9_C	0_V 0_C	20_V 30_C	0.66_V 0.66_C
YPAD, Late Exp	700_D 654_V 663_C	550_D 520_V 479_C	90_D 107_V 157_C	56_D 29_V 28_C	0_D 0_V 0_C	5.3_V 5.8_C	1.1_V 1.9_C	0_V 0_C	20_V 30_C	0.30_V 0.33_C
YPAD, Slow-growth	1500_D 1480_V 1450_C	990_D 984_V 960_C	150_D 130_V 140_C	75_D 66_V 77_C	285_D 282_V 273_C	0.65_V 0.41_C	0.066_V 0.060_C	0.010_V 0.120_C	20_V 30_C	0.033_V 0.033_C
MM, Exponential	430_D 436_V 454_C	327_D 323_V 330_C	90_D 86_V 88_C	13_D 27_V 27_C	0_D 0_V 0_C	6.0_V 6.0_C	1.6_V 1.6_C	0_V 0_C	20_V 30_C	0.50_V 0.50_C
MM, Stationary 30 hrs	2000_D 2000_V 1980_C	1360_D 1518_V 1270_C	230_D 192_V 121_C	210_D 64_V 75_C	200_D 226_V 515_C	0.74_V 0.42_C	0.055_V 0.015_C	0.008_V 0.230_C	20_V 30_C	0.00_V 0.00_C
MM, Stationary 120 hrs	6800_D 6610_V 6500_C	4110_D 3800_V 4120_C	230_D 510_V 223_C	210_D 64_V 75_C	2250_D 2236_V 2080_C	0.74_V 0.42_C	0.055_V 0.015_C	0.008_V 0.230_C	20_V 30_C	0.00_V 0.00_C

One discrepancy between the behavior of the models and that of real cells was the rate of Fe accumulation in cells during the transitionary phase. The observed rate was much faster than could be simulated. Observed accumulation levels could only be achieved by slowing the growth rate in simulations *without* simultaneously reducing the organelle Fe import rates (*See* dashed lines in Figures III-10B and III-11B). We conclude that the more rapid increase of cellular Fe as real cells transition from exponential to slow-growth or stationary states arises because the growth rate of those cells is reduced more rapidly than Fe import rates are reduced; i.e. *there is a delay in reducing the Fe import rates after cell growth slows*.

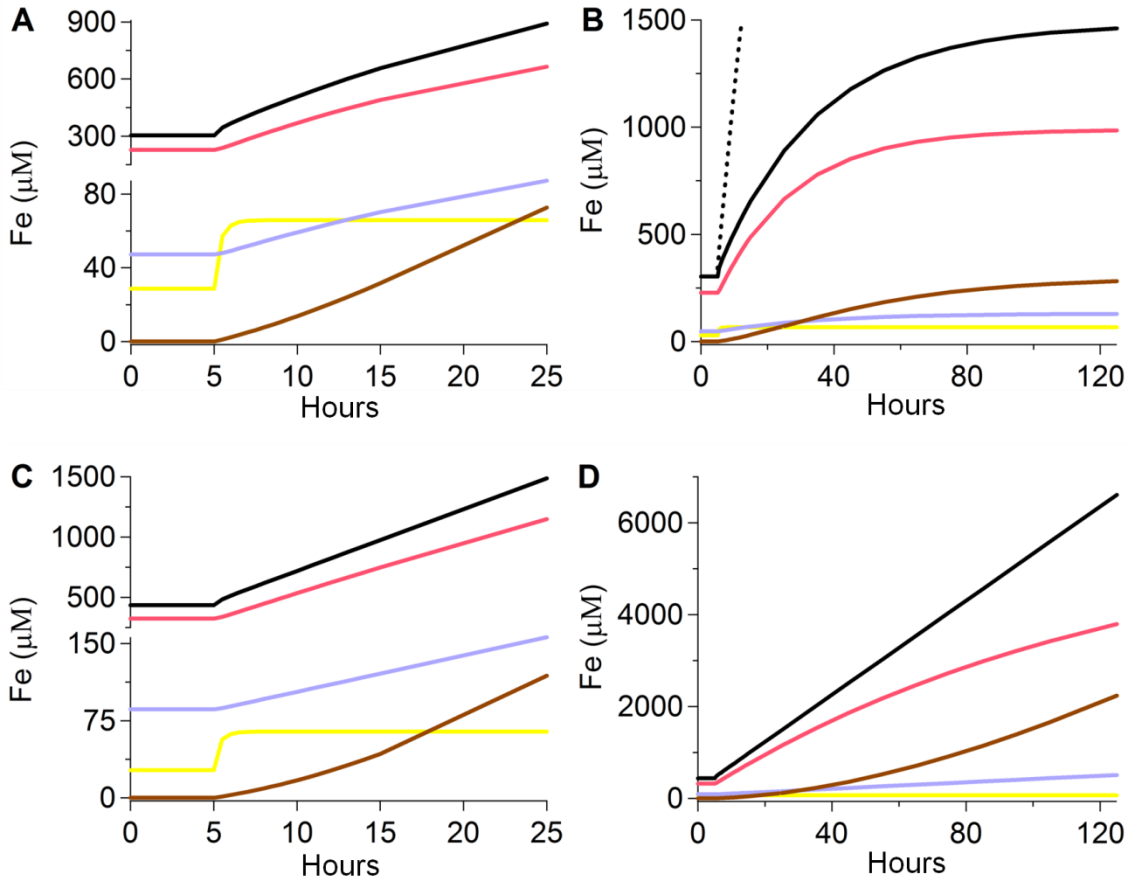

Figure III-10. Simulated kinetics of Fe uptake and trafficking in yeast cells. A, YPAD, 1-day-growth scale; B, YPAD, 5-day-growth scale; C, MM, 1-day-growth scale; D, MM, 5-day-growth scale. The first 5 hr reflects exponential growth conditions, the final distribution at 120 hr reflects the post-exponential phase, and intervening times reflect the transitionary period. Black, pink, cyan, yellow, and brown lines indicate [Fe_{cell}], [Fe_V], [Fe_M], [Fe_C], and [Fe_P], respectively. Dashed line simulates [Fe_{cell}] when cell growth shuts down immediately while the high-affinity Fe import rate remains unchanged.

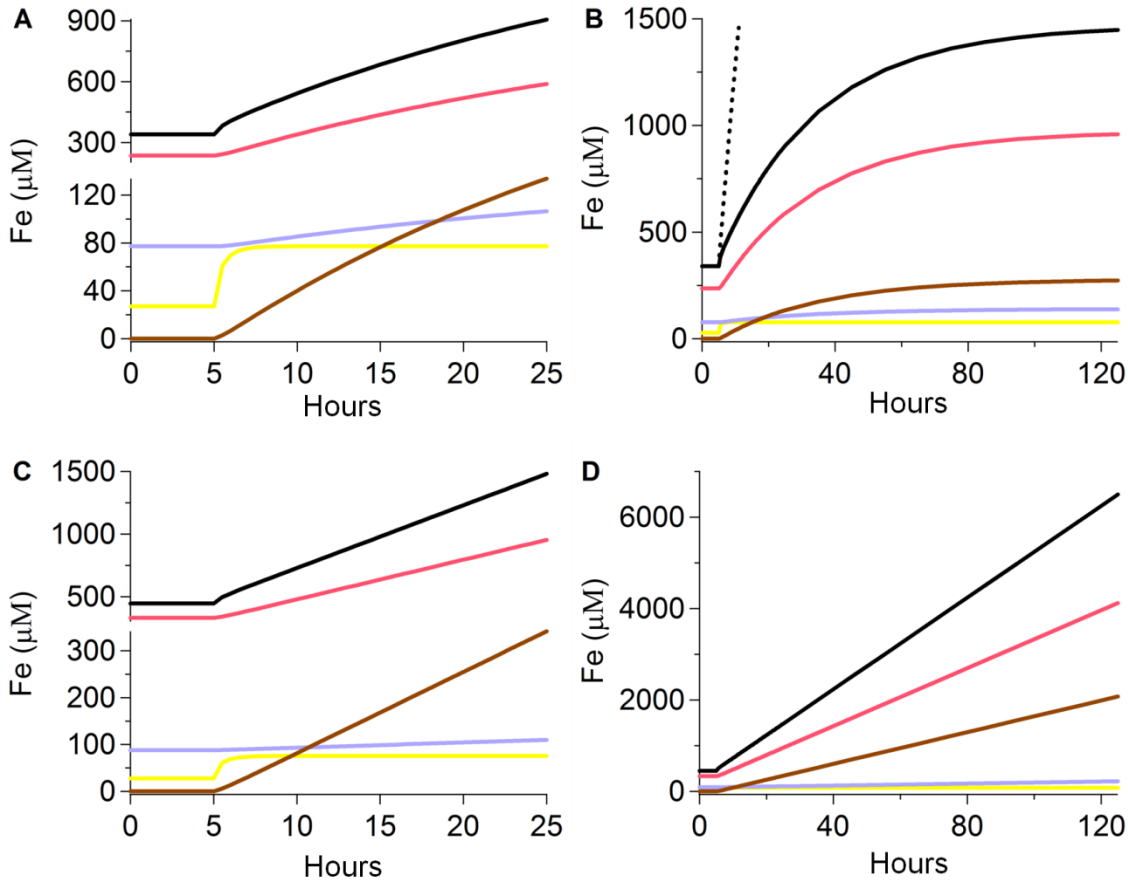

Figure III-11. Simulated kinetics of Fe import and trafficking in yeast cells using Model C. *See* legend of Figure III-10 for details.

R_{LO} contributed 20-30 μM/hr of Fe import under all growth conditions, whereas the contribution of R_{HI} varied significantly due to changes in the *Reg*_ term. Under YPAD and MM exponential conditions, our simulations show that R_{HI} imported Fe at a rate of ~ 180 μM/hr $\left(180 = 340 \cdot 1/\left(1+\left(28.8/30\right)^3\right)\right)$ corresponding to ~ 90% of total Fe influx, whereas during slow-growth or stationary phases, simulations indicate that R_{HI} imported Fe at a rate of ~25 μM/hr $\left(25 \approx 340 \cdot 1/\left(1+\left(70/30\right)^3\right)\right)$, representing *ca*. 45%

of total Fe import flux. These changes in Fe influx reflect the extent of regulation which is controlled in our model by the concentration of Fe_C (Table III-2).

The concentration of Fe_C in exponentially growing cells did not depend strongly on growth rate (e.g. varying α from 0 – 0.7 hr^{-1} caused $[Fe_C]$ to vary from 28.9 to 27.7 μM), but it did depend strongly on flow rates into the organelles (which varied with growth rate). When the rate-constants associated with organelle import were reduced from those associated with exponential growth to those associated with slow-growth or stationary conditions (with α invariant), $[Fe_C]$ increased from 28 $\rightarrow$ 70 μM. The opposite happened when these import rates were increased. These organelle-import rates rather than cell growth rates *per se* dictate high-affinity Fe import rates. These effects can be rationalized from the chemical model of Figure III-9 by considering how the cytosolic Fe concentration would be affected by changing various organelle Fe import rates.

Discussion

Our results and mathematical analysis demonstrate that Fe import in yeast is effectively unregulated when cells are grown in batch culture to post-exponential growth states. This includes a post-diauxic state (for growth on YPAD medium) in which cells grow slowly, and a true stationary state (for growth on MM medium). Such cells accumulate excess Fe to an extent dependent on the duration of post-exponential growth, the nature of the growth medium, and the concentration of Fe in the medium. These results are surprising, given the abundant evidence and common understanding that all

metabolites and components of a cell are tightly regulated. Fe appears to be an exception to this rule.

There may be several molecular-level phenomena that collectively give rise to this lack of regulation. The low-affinity Fe import pathway dominates in post-exponential cells and it does not depend strongly on the growth rate of the cell. Thus, even as cells slow or stop growing, they continue to import Fe through this pathway. The high-affinity Fe import pathway is tightly regulated but it shuts-down during post-exponential growth more slowly than the cell's growth rate declines. As a result of this mismatch, the cell accumulates Fe. Some of this excess imported Fe is converted into nanoparticles, a process that is probably not regulated by the cell because the cell is unable to sense these aggregated precipitates. In fact, our results show that the extent of nanoparticle formation is "contra-regulated" – meaning that as the rate of Fe import declines in post-exponentially grown cells in response to cellular regulation, the rate of nanoparticle formation increases!

The situation is different for cells growing exponentially. Here Fe import and trafficking are well regulated and controlled. The high-affinity pathway dominates the import flux of Fe, and nanoparticles are not formed. Fe uptake and cell growth rates are matched such that cellular Fe concentration is basically invariant. The high-affinity Fe uptake system (as monitored by Fet3p expression) is functioning during this phase, even with an Fe concentration of 40 μM in the medium. A previous study found that Fet3p was not expressed in cells grown on 40 μM MM and harvested early in the transitionary

period.[19] This is consistent with the shutdown of the high-affinity system as cells transition into the slow-growth state.

The low-affinity system may involve Fet4p, a divalent metal transporter on the plasma membrane, and/or Smf1. Since Fet4p is still active when cells are grown with 1 mM Fe-containing media,[22] Fet4p appears to be responsible for Fe uptake in cells grown on high [Fe] media; under these conditions, cells express almost no Fet3p.[19] The variation of Fet4p expression with changes in growth mode needs to be evaluated, but we suspect that Fet4p is the major Fe importer during post-exponential growth.

We report here a second type of nanoparticles in WT cells grown to post-exponential states. These nanoparticles differ in terms of structure or composition relative to those formed in the mitochondria of ISC mutant strains, but further studies are required to define these differences. The MB and EPR signatures associated with these nanoparticles are broad and unresolved, making any such characterization difficult. Nor do we know the location of these or the previously characterized type of nanoparticles that form in WT cells under post-exponential conditions. A small proportion is present in mitochondria (as evidenced in MB spectra of isolated WT mitochondria), but the quantity present there is low relative to the overall concentration of nanoparticles present in these cells. The quantity present is far less than that which accumulates in mitochondria in ISC mutant strains. The majority of nanoparticles that form in post-exponentially grown WT cells are non-mitochondrial.

Two locations for nanoparticles seem likely, namely vacuoles and the cytosol, but at this point we cannot distinguish between them. Nishida *et al*. have identified

nanoparticles in vacuoles[46,79] and we have found that the Fe in vacuoles is susceptible to nanoparticles formation.[33] The source of this susceptibility is uncertain, but Fe^{III} polyphosphate (which is closely related to vacuolar Fe) forms nanoparticles at high pH (e.g. 7). The vacuolar lumen is acidic, with values between 4.5 and 5.5 typical. For these reasons, we favor a vacuolar location for the majority of nanoparticles in post-exponential WT cells.

A recent report indicates that aging and mitochondrial dysfunction are associated with an increase of vacuolar pH.[102] Post-exponential cells are old, raising the intriguing possibility that decreased acidity in vacuoles causes mononuclear HS Fe^{III} species in vacuoles to precipitate as nanoparticles. Losing a proton from a coordinated water could help generate a bridge between two mononuclear complexes. This process, occurring repeatedly throughout a population of HS Fe^{III} complexes, could cause nanoparticles to form. Since nanoparticles are precipitated aggregates, this process might be sensed by the cell as a *decline* of vacuolar Fe (despite the fact that Fe is accumulating). This may or may not prompt additional Fe to be imported into the organelle.

Fe is generally considered to be deleterious to the cell when in excess, because it can catalyze the formation of hydroxyl radicals and other ROS.[5] Indeed, we and others have linked ROS damage in mitochondria to nanoparticle formation in that organelle.[80,83,103] In our current study, we found no correlation between ROS formation and Fe accumulation, suggesting that the lack of Fe regulation may not be especially critical for the health of such cells. Our results show that vacuoles have an enormous capacity to store Fe. Perhaps the sequestration of Fe in vacuoles prevents ROS from

being generated. The same may not hold true for mitochondria; this organelle in WT cells appears to be more strictly regulated in terms of Fe, such that it does not normally accumulate massive quantities of nanoparticles. Nanoparticles generated in other compartments may not significantly damage the cell, suggesting that in a non-mitochondrial context, nanoparticles should be viewed more of a nuisance than as a danger. Another consideration is that in slow-growing (or stationary state) cells, Fe-associated ROS may have been eliminated (by the ROS-response machinery of the cell) faster than it was generated during Fe accumulation/nanoparticle formation.

In our previous studies, cells grown in medium containing Fe concentrations as high as 10 mM did not show as high cellular Fe concentrations as we have observed here.[19] However, in those studies, cells were harvested in late exponential phase (OD = 1.2); this is before the Fe accumulation phenomenon becomes severe. Our current study reveals that the mode of growth *near the time of harvesting* is critically important in dictating the extent of Fe accumulation.

The time-dependence of regulation has not been highlighted in previous studies of cellular Fe metabolism. In most published studies, the exact growth mode and growth rate at the time of harvesting are often not determined or mentioned. Our results highlight the importance of this information in interpreting the phenotype of various Fe-associated mutant strains. The excess Fe that accumulates in yeast cells during post-exponential growth periods could confuse such interpretations and obscure the primary function of the mutated protein, a typical objective of such studies. In the future, those studying Fe metabolism in yeast should ideally focus on the Fe content of *exponentially*

growing cells to provide insight into Fe-related metabolism and into the primary function of associated proteins.

Such cases of poor regulation rarely occur in a cell because virtually all cellular reactions are enzyme-catalyzed and thus genetically (and allosterically) regulated by the cell. Enzyme catalyzed reactions are typically orders-of-magnitude faster than non-catalyzed reactions. Iron evades such controls because nanoparticles can form rapidly via non-enzymatically catalyzed reactions. Moreover, the cell has no means of directly sensing the quantity of nanoparticles that it contains. Nanoparticle formation depends on very general chemical properties of the cell such as pH and redox status. Thus, in the case of Fe the cell simply tolerates a bit of chaos. Fortunately, the reactions are not lethal as they do not generate toxic levels of ROS. Although we cannot state unequivocally that this lack of cellular regulation is unique for Fe, such an occurrence for another cellular component would require a similar combination of reaction chemistries which we regard as unlikely.

CHAPTER IV

EFFECT OF NUTRIENT STATUS ON THE IRON CONTENT IN *SACCHAROMYCES CEREVISIAE*

Introduction

Iron (Fe) plays many critical roles in cellular biochemistry. As a redox-active transition metal ion, it functions in enzyme catalysis, electron transfer processes, and small-molecule binding and activation.[1] It is found in numerous forms, including as Fe/S clusters (ISCs), heme centers, nonheme mono- and dinuclear complexes, among others. Certain Fe complexes promote Fenton chemistry which is detrimental to the cell; such complexes help generate reactive oxygen species (ROS) which can damage DNA, proteins, and membranes. Thus, Fe trafficking and regulation must be tightly controlled by the cell.

The molecular-level details of Fe trafficking and regulation are best understood in budding yeast *Saccharomyces cerevisiae*. Mitochondria and vacuoles are major "traffic hubs" of these cells, but the plasma membrane, cytosol and nucleus also play critical trafficking roles.[9,10] The plasma membrane comprises numerous proteins that import Fe from the environment. The membrane-bound Fet3p/Ftr1 (ferroxidase/permease) complex constitutes the "high affinity" Fe importer.[14] The genes encoding these and about 20 other Fe-related proteins in the cell are regulated by Aft1p.[6] This transcription factor is activated (via a partially known mechanism) by low concentrations of an unknown Fe-containing species (possibly an ISC-containing

protein) in the cytosol.[8] The plasma membrane protein Fet4p constitutes the low-affinity pathway for Fe^{II} import.[21]

Mitochondria are the major site of Fe/S cluster assembly and heme biosynthesis. Cytosolic Fe is imported via the inner-membrane proteins Mrs3p/4p; these proteins constitute the "high affinity" mitochondrial Fe import pathway. Poorly characterized low-affinity pathways are also present.[31,32] Many of the assembled ISCs and hemes are installed into the mitochondrial respiratory complexes and other mitochondrial proteins involved in respiration.

Vacuoles, the other major Fe trafficking hub in *S. cerevisiae*, store and sequester Fe, and mobilize it as needed by the cell. The dominant form of Fe in the organelle is a mononuclear HS Fe^{III} complex with polyphosphate-related ligands.[46] Under Fe-replete growth conditions (> 10 μM Fe), vacuolar Fe constitutes ~ ¾ of total cellular Fe.[19]

In a recent study, we found that the Fe content of yeast cells growing exponentially on minimal medium (MM) was approximately invariant with time, but that the cellular Fe concentration increased as the cells transitioned into steady-state.[104] The mode and rate of growth at the time of harvesting dramatically affected cellular Fe content. A mathematical model of Fe metabolism in a growing cell was developed, including: a) Fe import via a regulated high-affinity pathway and an unregulated low-affinity pathway; b) Fe import from the cytosol into vacuoles and mitochondria; and c) nanoparticle formation. The model captured essential behavior and demonstrated that the cell regulates its Fe import rate in accordance with its overall growth rate. The lack of

regulation of Fe in yeast is perhaps unique relative to the tight regulation of other cellular metabolites. This phenomenon likely derives from the unique chemistry of Fe.

During the course of these studies, we also discovered that the components of the growth medium affect the Fe content (distribution and speciation) of *S. cerevisiae* cells. In this report, we describe these effects. We grew cells on minimal medium (MM) modified with different combinations of nutrients, including glucose, amino acids, and nitrogenous bases. We monitored cellular Fe content using Mössbauer (MB), EPR and electron absorption spectroscopies and ICP-MS. We also examined the effect of inhibiting the *Target of Rapamycin Complex 1* (TORC1). TOR is an incompletely defined metabolic system the inhibition of which is associated with the starvation response including increased lifespan.[61]

Results

Effect of adenine deficiency

Strain W303 possesses a mutation in *ADE2* which is essential for adenine biosynthesis. MM contains 100 μM adenine which is sufficient for normal cell growth. Cells deficient in adenine can grow but are pink due to an intermediate in adenine biosynthesis that accumulates.[70,105] Cells grown on medium containing 12 μM adenine (called A↓ medium) grew at the same rate as MM-grown cells during exponential phase (DT ≈ 2.0 hr) but slowed earlier than MM-grown cells as they reached stationary phase (compare the OD plot in Figure IV-1A to that in Figure III-1C). The final OD_{600} was ~ 75% of that of equivalent MM-grown cells. Compared to MM-grown cells, A↓-grown

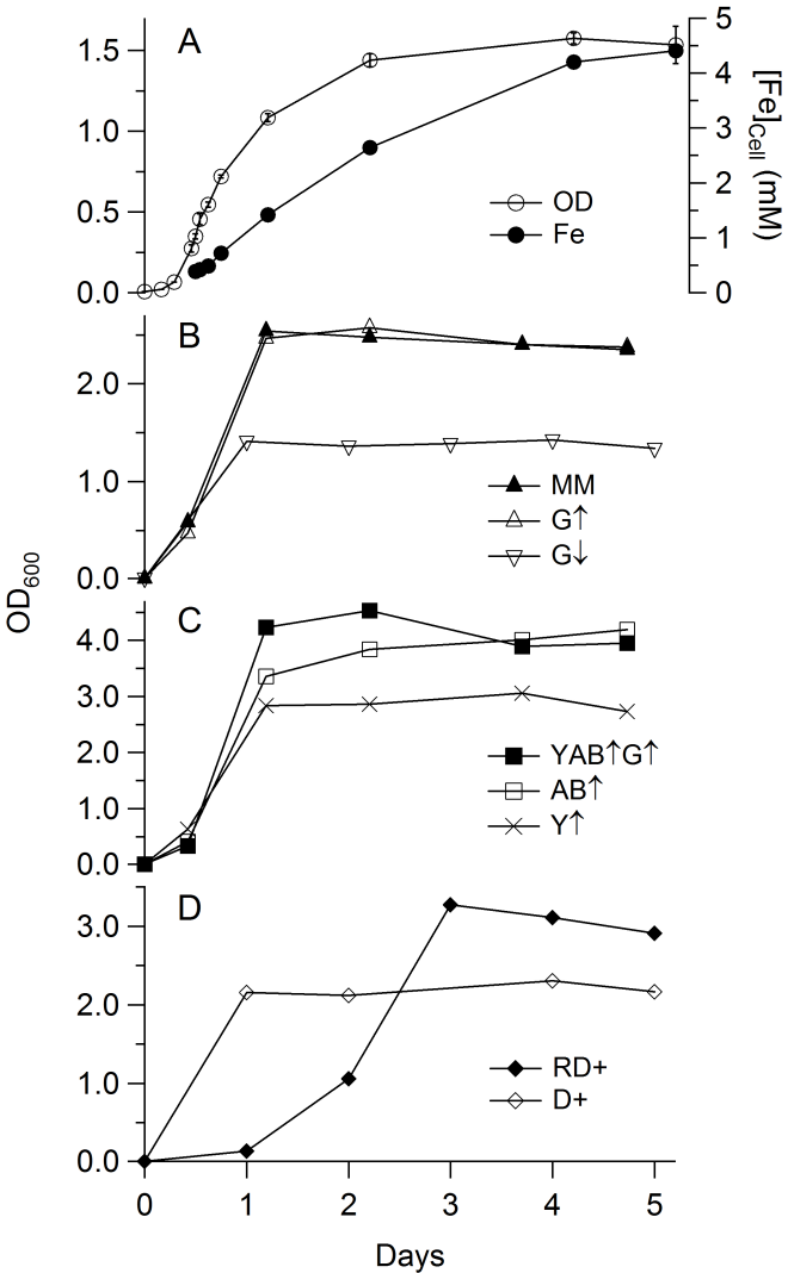

Figure IV-1. Growth plots of W303 cells on various MM-based media, monitored at OD_{600}. A, growth (open circles) and Fe concentration (filled circles) plots of cells grown on A↓ medium. Plots are the averages of two independent experiments; vertical bars indicate standard error. B – D, growth plots of cells grown on MM (filled triangles), G↑ (open triangles), G↓ (inverted open triangles), YAB↑G↑ (filled squares), AB↑ (open squares), Y↑ (×), RD+ (filled diamonds), D+ (open diamonds) media, respectively. Each plot represents the average of three independent experiments. Relative standard error for each point was ≤ 15%.

cells accumulated Fe at a slower rate as cells transitioned from exponential growth to stationary state (~ 70 *vs*. 100 μM/hr). They accumulated Fe at a similar rate during stationary state (~ 25 *vs*. 30 μM/hr) (compare the Fe concentration plot in Figure IV-1A to that in Figure III-1C). We previously hypothesized that MM-grown cells accumulated large quantities of Fe as they transitioned from exponential growth mode to stationary state because the rate of Fe import declined slower than the growth rate of the cell declined during this transitionary period.[104] The more modest accumulation of Fe in adenine-deficient cells probably arises because these two rates are synchronized more closely.

A↓-grown cells harvested during early exponential phase (OD = 0.2) contained 290 μM Fe and exhibited a low-temperature low-field Mössbauer (MB) spectrum similar to that of MM-grown cells harvested during the same phase (Figure IV-2A *vs*. Figure III-4A). Dominating the spectrum was a sextet due to vacuolar HS Fe^{III} (Figure IV-2A, purple line) and the central doublet (CD, Figure IV-2A, green line) due to $[Fe_4S_4]^{2+}$ clusters and low spin (LS) Fe^{II} hemes. The purple and green lines simulate these species, using parameters given in Table IV-1. Such cells were not pink, indicating adenine sufficiency. An electronic absorption spectrum of equivalent cells exhibited peaks due to reduced heme centers (Figure IV-3A, *inset*).

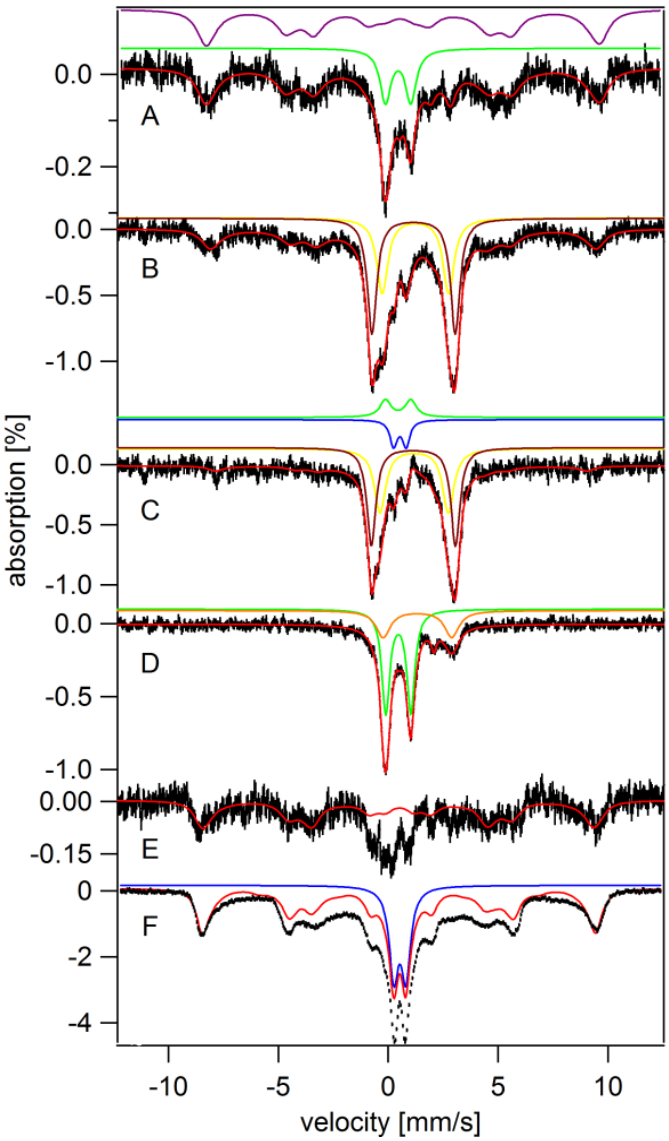

Figure IV-2. 5 K, 0.05 T Mössbauer spectra of mitochondria, vacuoles, and whole yeast cells grown on A↓ medium and harvested at different growth phases. A, cells harvested during exponential phase (OD_{600} = 0.2); B, cells harvested during transitionary phase (OD_{600} = 0.9); C, B-minus-A difference spectrum; D, mitochondria from cells isolated during transitionary phase (OD_{600} = 0.9); E, vacuoles isolated from cells harvested during transitionary phase (OD_{600} = 0.9); F, 5-day-old cells harvested in stationary phase (OD_{600} = 0.9). Red lines are composite simulations that include HS Fe^{III}, NHHS Fe^{II}, NHHS Fe^{II} heme, CD, and Fe^{III} nanoparticle features. The purple, green and blue lines are simulations of the HS Fe^{III}, CD and Fe^{III} nanoparticles spectral features, respectively. Maroon and yellow lines in B and C are simulations of the NHHS Fe^{II} species. The orange line in D is a simulation of the NHHS Fe^{II} species in mitochondria.

In contrast, A↓-grown cells harvested during transitionary phase (OD = 0.9) were pink, indicating adenine-deficiency. The electronic absorption spectrum of the such cells contained absorption maxima at 490 and 540 nm cells (Figure IV-3B), as previously observed of adenine-deficient.[105] Perhaps these cells transitioned out of exponential growth mode as they depleted the adenine available in the medium. They contained 780 μM Fe - slightly lower than cells grown on MM for an equivalent period (24 hr, ~ 1.1 mM). A↓-grown cells exhibited a MB spectrum dominated (with ~56% spectral intensity) by a broad NHHS Fe^{II} doublet (Figure IV-2B). A sextet originating from vacuolar HS Fe^{III} ions was also present, but at an intensity (31%) that was *ca*. half of that observed in spectra of adenine-sufficient cells harvested at about the same OD. In previous studies, the concentration of NHHS Fe^{II} in yeast cells ranged from 20 – 70 μM.[19,78,81] In contrast, the concentration of such species in A↓-grown cells in the transitionary state was about 430 μM! In MM-grown cells, there was also a buildup of Fe during the transitionary period, but the Fe that accumulated was primarily Fe^{III} nanoparticles (and a small amount of NHHS Fe^{II}).

Among 4 different batches of A↓-grown cells that were examined (containing 12 or 25 μM adenine in the media, Figure IV-2B, IV-4 and Table IV-1), the percentage of the NHHS Fe^{II} doublet in MB spectra was as high as 84% while that of the NHHS Fe^{III} sextet was as low as 7%. The difference spectrum (Figure IV-2C) reveals that the Fe which accumulated during the transitionary growth period was mainly NHHS Fe^{II} (85%, maroon and yellow lines), along with a small contribution of Fe^{III} nanoparticles (10%, blue). There appears to have been a slight decline in the CD concentration as adenine-

Table IV-1. Isomer shift (δ, mm/s), quadrupole splitting (ΔE_Q, mm/s), line width (Γ, mm/s) and percentage of Fe species as determined from Mössbauer spectra used in Chapter IV. For HS Fe^{III}, isotropic hyperfine coupling constant, A_{iso} values (kG) were also listed. Parameters were averaged from all spectra presented in this paper, but some parameters ($\delta/\Delta E_Q/\Gamma$) were listed separately if they were apart from the averaged numbers. *Percentages of signals with broad range of A values (Fe aggregates) was estimated based on the intensity left after subtracting all assignable signals from original spectra. Bold-styled parameters were fixed when simulated.

Spectrum (**Total [Fe]**)	Non-heme HS Fe^{III}	Non-heme HS Fe^{II}	HS heme Fe^{II}	Central doublet	Fe^{III} nano-particle
A_{iso} (kG)	229 ± 4	-	-	-	-
δ (mm/s)	-	1.34 ± 0.05	0.85 ± 0.03	**0.45**	0.53 ± 0.01
ΔE_Q (mm/s)	-	3.06 ± 0.05	2.38 ± 0.07	**1.15**	0.52 ± 0.04
Γ (mm/s)	-	0.65 ± 0.07	0.39 ± 0.10	**0.60**	0.45 ± 0.10
MM-AD/OD 0.2 Fig. 2A **(290 µM)**	61%	10%	3%	19%	3%
MM-AD/OD 0.9 Fig. 2B **(780 µM)**	31%	1.23/3.04 /0.61, 24% 1.15/3.79 /0.51, 32%	2%	3%	8%
Fig. 2B - 2A Fig. 2C (**~ 500 µM**)	12%	1.19/3.08 /0.61, 36% 1.15/3.82 /0.49, 49%	3%	-10%	10%
MM-AD/OD 0.9 Mitochondria Fig. 2D **(760 µM)**	-	26%	7%	0.46/1.14 /0.43, 56%	**0.52**/**0.63** /0.25, 3%

Table IV-1. Continued

Spectrum (**Total [Fe]**)	Non-heme HS Fe^{III}	Non-heme HS Fe^{II}	HS heme Fe^{II}	Central doublet	Fe^{III} nano-particle
A↓/OD 0.9 Vacuole Fig. 2E **(200 µM)**	80%	-	-	-	-
A↓/OD 0.9 /5 days Fig. 2F **(6800 µM)**	46%	-	-	-	21% (30%)*
G↓ OD 1.5, 5 days Fig. 4A **(1200 µM)**	63%	4%	2%	-	25%
MM OD 2.3, 5 days Fig. 4B **(3400 µM)**	65%	7%	2%	-	15% (6%)*
G↑ OD 1.9, 5 days Fig. 4C **(4000 µM)**	65%	6%	2%	-	15% (6%)*
G↑Fe↑ OD 1.8, 5 days Fig. 4D **(18.5 mM)**	15%	-	-	-	0.54/0.56 /0.66, 70% (10%)*

Table IV-1. Continued

Spectrum (**Total [Fe]**)	Non-heme HS Fe^{III}	Non-heme HS Fe^{II}	HS heme Fe^{II}	Central doublet	Fe^{III} nano-particle
RD+ OD 2.7, 5 days Fig. 4E **(890 µM)**	57%	17%	2%	3%	21%
YAB↑ OD 3.8, 5 days Fig. 6A **(1800 µM)**	91%	-	3%	6%	-
YAB↑G↑ OD 5.2, 5 days Fig. 6B **(2700 µM)**	89%	-	3%	6%	2%
AB↑ OD 4.0, 5 days Fig. 6C **(990 µM)**	50%	30%	2%	6%	10%
Y↑ OD 2.2, 5 days Fig. 6D **(4500 µM)**	67%	-	3%	-	14% (10%)*
A↓ (5 mg/L Ade) OD 1.2 Fig. S2A	8%	1.27/3.08 /0.75, 53% 1.15/3.93 /0.46, 31%	-	6%	-

Table IV-1. Continued

Spectrum (**Total [Fe]**)	Non-heme HS Fe^{III}	Non-heme HS Fe^{II}	HS heme Fe^{II}	Central doublet	Fe^{III} nano-particle
A↓ (10 mg/L Ade) OD 1.3 Fig. S2B	13%	1.18/2.98 /0.65, 28% 1.11/3.78 /0.48, 43%	5%	4%	4%
A↓ (10 mg/L Ade) OD 2.1 Fig. S2C	14%	1.33/3.07 /0.66, 51% 1.15/3.92 /0.50, 26%	-	3%	4%
A↓ (10 mg/L Ade) OD 1.5, 5 days Fig. S2D	45%	1.40/2.90 /0.75, 10% 1.11/3.85 /0.75, 4%	3%	5%	13% (15%)*
YAB↑G↓ OD 1.6, 5 days Fig. S5 **(390 µM)**	53%	23%	1%	7%	14%

deficient cells entered transitionary phase (Figure IV-2C, green line), but this may also be because the two samples from which the difference spectrum was obtained were from different batches. Since the MB spectrum of mitochondria isolated from A↓-grown cells exhibited a strong CD (Figure IV-2D, green line), it is unlikely that adenine-deficient cells would contain less CD-associated Fe than are present in adenine-sufficient cells.

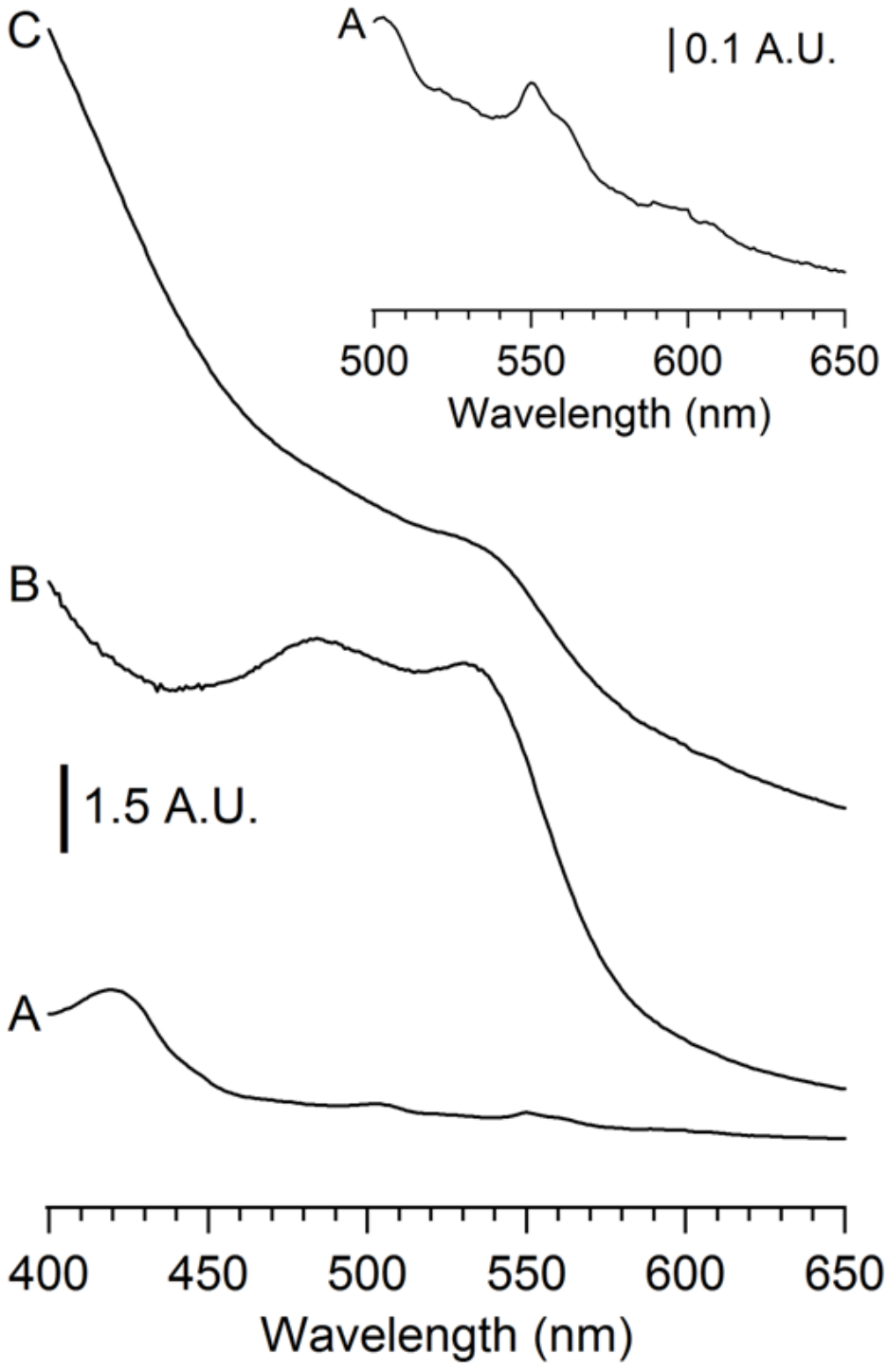

Figure IV-3. Electronic absorption spectra of A↓-grown cells (12 μM adenine). A, OD 0.2, 8 hours; B, OD 1.3, 1 day; C, OD 2.1 (10-fold diluted, 2-fold amplified), 5 days. *Inset*, same as A but magnified to show heme signals.

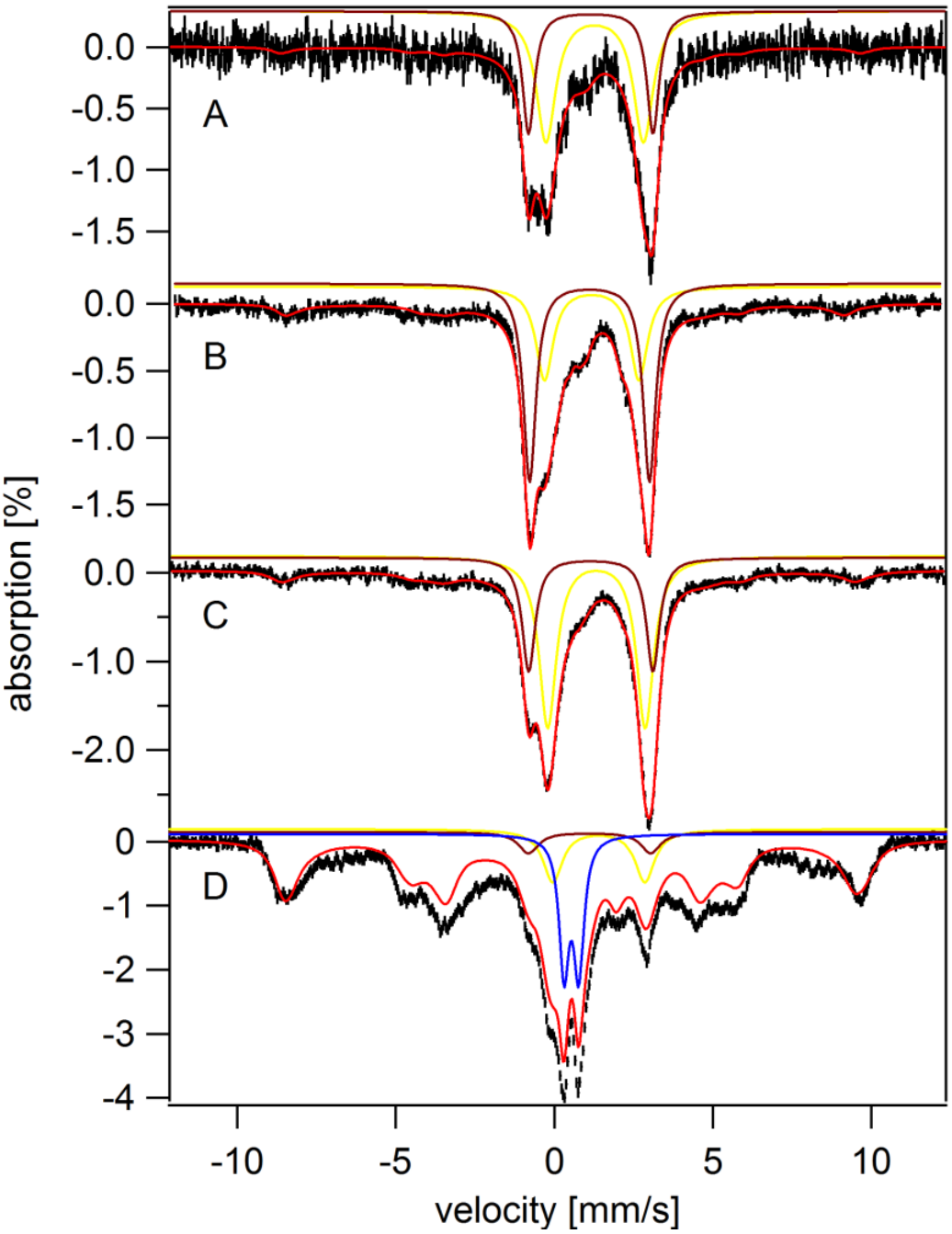

Figure IV-4. Mössbauer spectra of A↓-grown cells at transitionary state. A, A↓ (12 μM adenine), OD 1.2; B, A↓ (25 μM adenine), OD 1.3; C, A↓ (25 μM adenine), OD 2.1; D, A↓ (25 μM adenine), OD 1.5, 5 days. Red lines simulate most of iron features in spectra; HS Fe^{III}, HS Fe^{II}, HS Fe^{II} heme, CD, Fe^{III} nanoparticles. Blue line simulates Fe^{III} nanoparticles, and yellow and maroon lines simulate two types of HS Fe^{II}, respectively.

Unfortunately UV-Vis spectroscopy could not be used to address this question, as the pink color of these cells obscured the heme features.

The broadness of the NHHS Fe^{II} doublet suggested more than one component. In spectra from two independent preparations (Figure IV-4, B and C), the resolution was sufficient to unambiguously demonstrate the presence of at least 2 species. Specie *a* had $\delta = 1.12 \pm 0.03$ mm/s and $\Delta E_Q = 3.85 \pm 0.05$ mm/s while specie *b* had $\delta = 1.25 \pm 0.05$ mm/s and $\Delta E_Q = 3.05 \pm 0.05$ mm/s. Both sets of parameters suggest NHHS Fe^{II} complexes dominated by 5 – 6 O donor ligands; 1-2 N and/or S donor ligands are possible. Species *a* and *b* may reflect pentacoordinate and octahedral complexes, respectively.[106]

Since the Fe concentrations of adenine-deficient and adenine-sufficient cells harvested at this OD were approximately the same, adenine deficiency can be (naively) viewed as causing NHHS Fe^{III} (vacuolar Fe) to be replaced by (or converted into) NHHS Fe^{II}. The simplest interpretation is that an adenine deficiency causes the cell to be more reduced such that vacuolar Fe^{III} (and/or Fe^{III} nanoparticles) is/are reduced to two (or more) Fe^{II} species. However, we have no definitive evidence that the observed NHHS Fe^{II} species are derived *directly* from the reduction of vacuolar Fe^{III} or nanoparticles; e.g. ligand replacement may accompany reduction.

We sought to determine the location of the NHHS Fe^{II} species *a* and *b*. MB spectra of vacuoles isolated from A↓-grown cells did not include the NHHS Fe^{II} doublets (Figure IV-2E), suggesting (but not proving) that *a* and *b* are located in another

organelle. Conceivably, these species could have been present in the vacuoles inside of the cell but exported during the isolation procedure.

The NHHS Fe^{II} doublet in the MB spectrum of isolated mitochondria (Figure IV-2D, simulated by the yellow line) was more intense than usual, but not intense enough to be responsible for the dominating NHHS Fe^{II} doublet observed in the whole-cell spectrum (mitochondria represent only *ca*. 3% of the volume of a cell[107]). We conclude that the majority of the NHHS Fe^{II} species in the cell are *not* located in mitochondria or probably not in vacuoles; we favor the cytosol as a possible location.

Like 1-day-old A↓-grown cells, 5-day old A↓-grown cells harvested in stationary state were pink (Figure IV-3C) but they contained far more Fe (6.8 mM) than did 1-day-old A↓-grown cells. This is slightly less than the Fe concentration of adenine-sufficient MM-grown cells harvested at an equivalent age (8.1 mM).[104] The MB spectrum of 5-day old A↓-grown cells (Figure IV-2F) was dominated by a sextet due to vacuolar HS Fe^{III} and a doublet due to Fe^{III} nanoparticles. MM-grown cells in stationary state exhibited virtually an identical spectrum (Figure III-4E). Curiously, the reducing effect of adenine-deficiency was transient, in that the NHHS Fe^{II} species was re-oxidized in stationary state and returned to the redox status characteristic of MM-grown cells – namely Fe^{III}. In one batch of 5-day-old A↓ cells, the dominating HS Fe^{II} doublet was still observed by MB, indicating some batch-to-batch variation in the extent of re-oxidation (Figure IV-4D). Re-oxidation may reflect a change in metabolism as the cells undergo the diauxic shift.

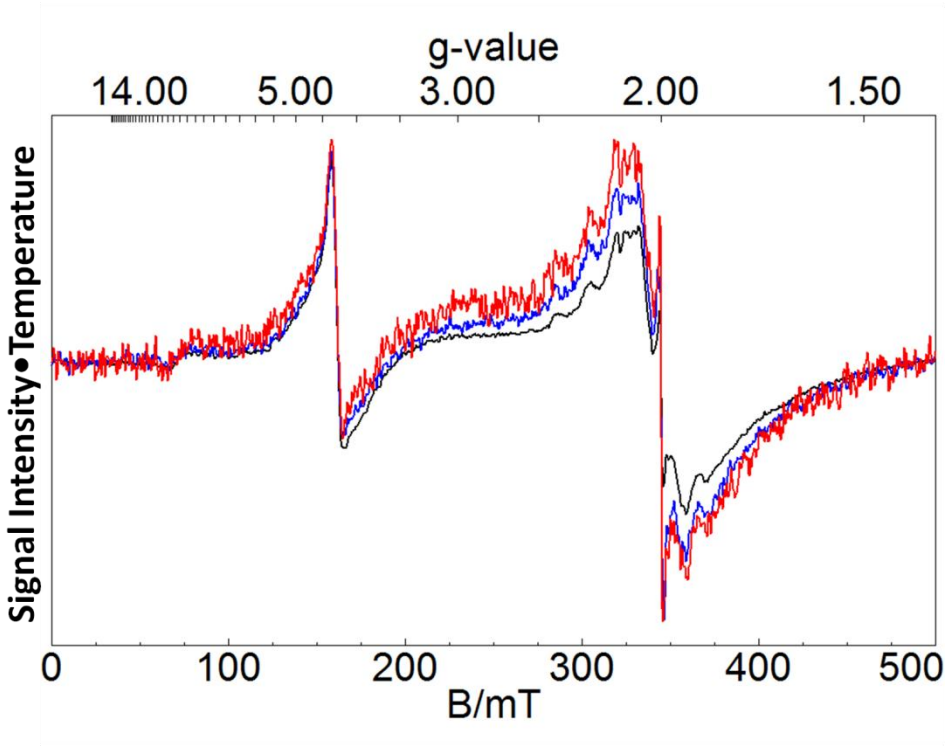

Figure IV-5. EPR spectra of A↓-grown cells at stationary phase. Black, 10 K; blue, 30 K; red, 70 K. Spectra were recorded at 0.05 mW microwave power, 9.64 GHz frequency and 10 Gauss modulation amplitude, and then have been adjusted vertically so that the g = 4.3 resonances are aligned.

The spectrum of 5-day old A↓-grown cells harvested in stationary state also contained a broad unresolved magnetic feature representing ~ 30% of the spectrum, again similar to that observed in the MB spectrum of 5-day-old MM-grown cells.[104] EPR of a corresponding A↓-grown sample exhibited a broad signal at g = 2.0 (Figure IV-5), similar to that observed in MM-grown cells (Figure III-6A). This feature originated from nanoparticles with somewhat different properties than those found in mitochondria of yeast strains that have ISC defects.[80,82,83]

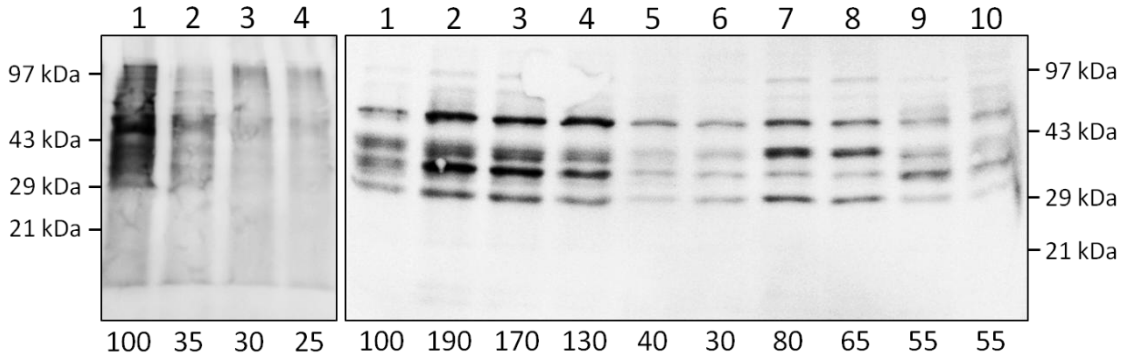

Figure IV-6. Oxyblot assay of whole cells grown on different media and harvested during different phases. Left panel, lane 1, MM, 1 day; lane 2, MM, 5 days; lane 3, A↓, 1 day; lane 4, A↓, 5 days. Right panel, lanes 1-5, 1 day-grown cells; lanes 6-10, 5 day-grown cells; lanes 1 and 6, MM; lanes 2 and 7, G↑; lanes 3 and 8, G↑Fe↑; lanes 4 and 9, AB↑; lanes 5 and 10, RD+. Percent band intensities relative to the blot from MM/1 day cells for each panel are displayed at the bottom of the image. Each lane was developed with 4 µg of whole cell lysate protein.

A↓-grown cells harvested both at 1 and 5 days exhibited *lower* levels of oxidative stress relative to analogous MM-grown cells (Figure IV-6, left panel, lane 3 and 4 vs. lanes 1 and 2). The diminished degree of oxidative damage in the 1-day-old A↓-grown cells is consistent with a more reducing environment of these cells, but inconsistent with our expectation that high concentrations of NHHS Fe^{II} ions should *promote* oxidative damage. Such ions typically have labile ligands and can participate in Fenton chemistry.[97] This is clearly not occurring here, suggesting that the coordination environments of these NHHS Fe^{II} ions are either *not* highly labile or that adenine-deficient cells protect against oxidant damage by producing a stronger ROS response. They might also sequester the NHHS Fe^{II} ions from ROS. Also, it is unclear whether the reducing environment is important in ROS damage, since 5-day old cells (which were

more oxidizing from an Fe-based perspective) showed low oxidative damage. Perhaps the level of oxidative stress is more closely correlated to the growth rate of the cell rather than to redox state or Fe concentration.

Glucose effect

Of all the nutrients contained in MM, glucose exerts perhaps the greatest influence on the metabolism of yeast.[47] Thus, we wondered whether changing the glucose concentration in the medium would affect the distribution and/or speciation of cellular Fe. Increasing the glucose concentration 3-fold (G↑ medium) did not affect the growth rate (Figure IV-1B, open *vs*. filled triangles) nor did it affect the Fe concentration in cells harvested in stationary state (Table IV-2, G↑ vs. MM). In contrast, *lowering* the glucose concentration 10-fold (G↓ medium) resulted in a ~ 40% lower culture density in the stationary state (Table IV-2, G↓ vs. MM and Figure IV-1B, inverted triangles vs. filled triangles) and a 7-fold lower final cellular Fe concentration (Table IV-2, G↓ vs. MM). We conclude that the glucose concentration limited growth in G↓ medium whereas one or more nutrients other than glucose limited growth in G↑ medium. Below we argue that these growth-limiting nutrients are particular amino acids (A = Leu, His, and Trp) and/or nucleotide bases (B = adenine and uracil).

Neither increasing nor decreasing the glucose concentration in MM strongly affected the cellular Fe *speciation* (Figure IV-7, A - C, Table IV-1 and Table IV-2). Under all three glucose conditions (G↓, MM and G↑), cells in stationary phase were dominated by the vacuolar HS Fe^{III} species (60 - 65% intensity) followed by Fe^{III}

Table IV-2. The final OD_{600} and [Fe_{cell}] after 5 days of growth. [a] standard error; [b] number of batches; [c] cells grown on A↓ media used 1 L of media in 3.8 L flasks whereas cells in all other media used 200 mL of media in 1 L flasks. Cells grown on 1 L of MM in 3.8 L flask accumulated 5.2 mM Fe.

Abbreviation	Description	Final OD_{600}	[Fe_{cell}] (mM)
MM	Minimal medium	2.3 ± 0.1[a] (4[b])	7.0 ± 1.7 (4)
A↓	8× less adenine	1.5 ± 0.1 (2)	4.4 ± 0.1 (2)[c]
G↑	3× more glucose	2.3 ± 0.2 (4)	7.6 ± 1.6 (4)
G↓	10× less glucose	1.4 ± 0.1 (4)	1.0 ± 0.1 (4)
Fe↑	10× more Fe^{III}-citrate	2.3 ± 0.2 (3)	22 ± 5 (3)
G↑Fe↑	3× more glucose 10× more Fe^{III}-citrate	2.1 ± 0.3 (2)	21 ± 3 (2)
Y↑	3× more YNB	2.6 ± 0.2 (4)	5.0 ± 0.3 (4)
YAB↑	3× more YNB 3× more Leu, His, Trp ("amino acids") 3×more adenine and uracil ("bases")	3.8 ± 0.1 (2)	1.8 ± 0.1 (2)
AB↑	3× more amino acids 3× more bases	4.1 ± 0.3 (4)	2.8 ± 0.9 (4)
YAB↑G↑	3× more amino acids, 3× more bases 3× more glucose	4.3 ± 0.5 (4)	4.1 ± 0.7 (4)
YAB↑G↓	3× more amino acids 3× more bases 10× less glucose	1.6 ± 0.1 (2)	0.42 ± 0.03 (2)
RD+	200 μM rapamycin dissolved in DMSO and then added to media at 20 nM final concentration	2.9 ± 0.2 (3)	1.2 ± 0.2 (3)
D+	DMSO was added at the same concentration as in RD+ medium (0.01% v/v, final concentration).	2.1 ± 0.1 (2)	-

nanoparticles (15 - 25%). Thus, the *extent* of Fe accumulation in the cell, but not the *distribution* of that Fe into different groups, was roughly proportional to the MM glucose concentration in the range 0.2% → 2%.

An exception to this last statement might involve mitochondrial Fe. The relative intensity due to the CD was difficult to quantify in these experiments because it was obscured by the broad nanoparticle doublet and the strong sextet feature in that region of the spectrum. However, UV-Vis spectra of these glucose-varied cells (Figure IV-8, A-C) indicated that heme levels (which primarily reflect mitochondrial respiratory complexes and associated heme-containing proteins) were greater in the G↓-grown cells (Figure IV-7A) than in MM- (Figure IV-7B) or G↑-grown cells (Figure IV-7C). This makes sense because G↓-grown cells must rely on respiration for growth whereas G↑-grown cells especially rely on fermentation.[47]

In MM-grown cells, more than half of the cellular Fe accumulated during the stationary state. This does not appear to have occurred with G↓-grown cells. One-day-old G↓-grown cells, which spent a large percentage of their growth in exponential phase, accumulated nearly the same amount of Fe as 5-day old G↓-grown cells (940 *vs*. 1000 μM). However, after 5 days of growth, the Fe concentration of these cells was 7-fold less than in the corresponding MM-grown cells. This implies that the Fe import rate in G↓-grown cells at stationary state was lower than in MM-grown cells, and that this (low-affinity) pathway is glucose-dependent. In contrast, the rate of Fe import during exponential phase did not exhibit a glucose-effect.

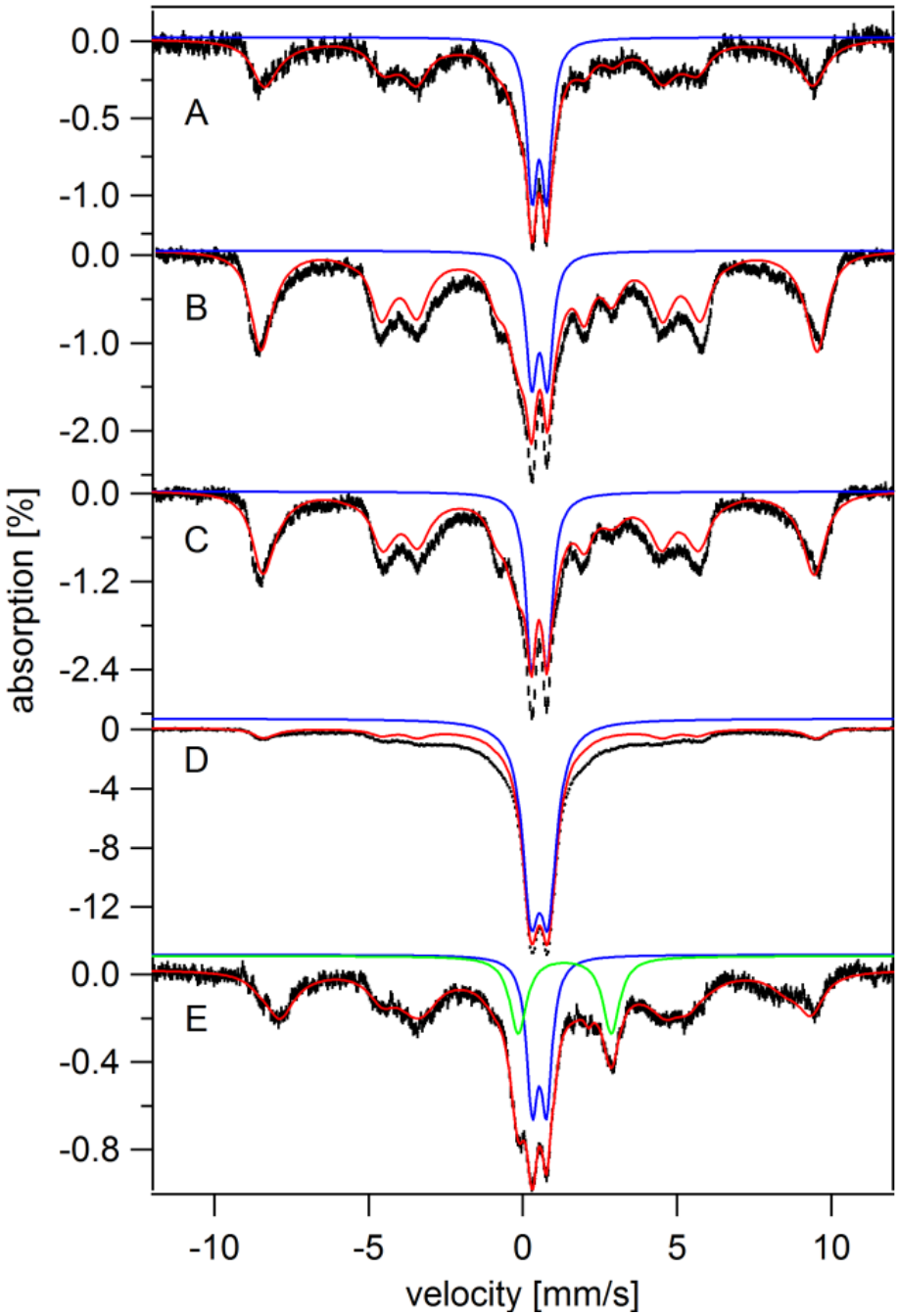

Figure IV-7. 5 K 0.05 T Mössbauer spectra of whole yeast cells grown for 5 days on different media. A, G↓; B, MM; C, G↑; D, G↑Fe↑; E, RD+. Red lines are composite simulations of HS Fe^{III}, HS Fe^{II}, HS Fe^{II} heme, CD, and Fe^{III} nanoparticles. Blue and green lines are simulations of spectral features from Fe^{III} nanoparticle and NHHS Fe^{II}, respectively.

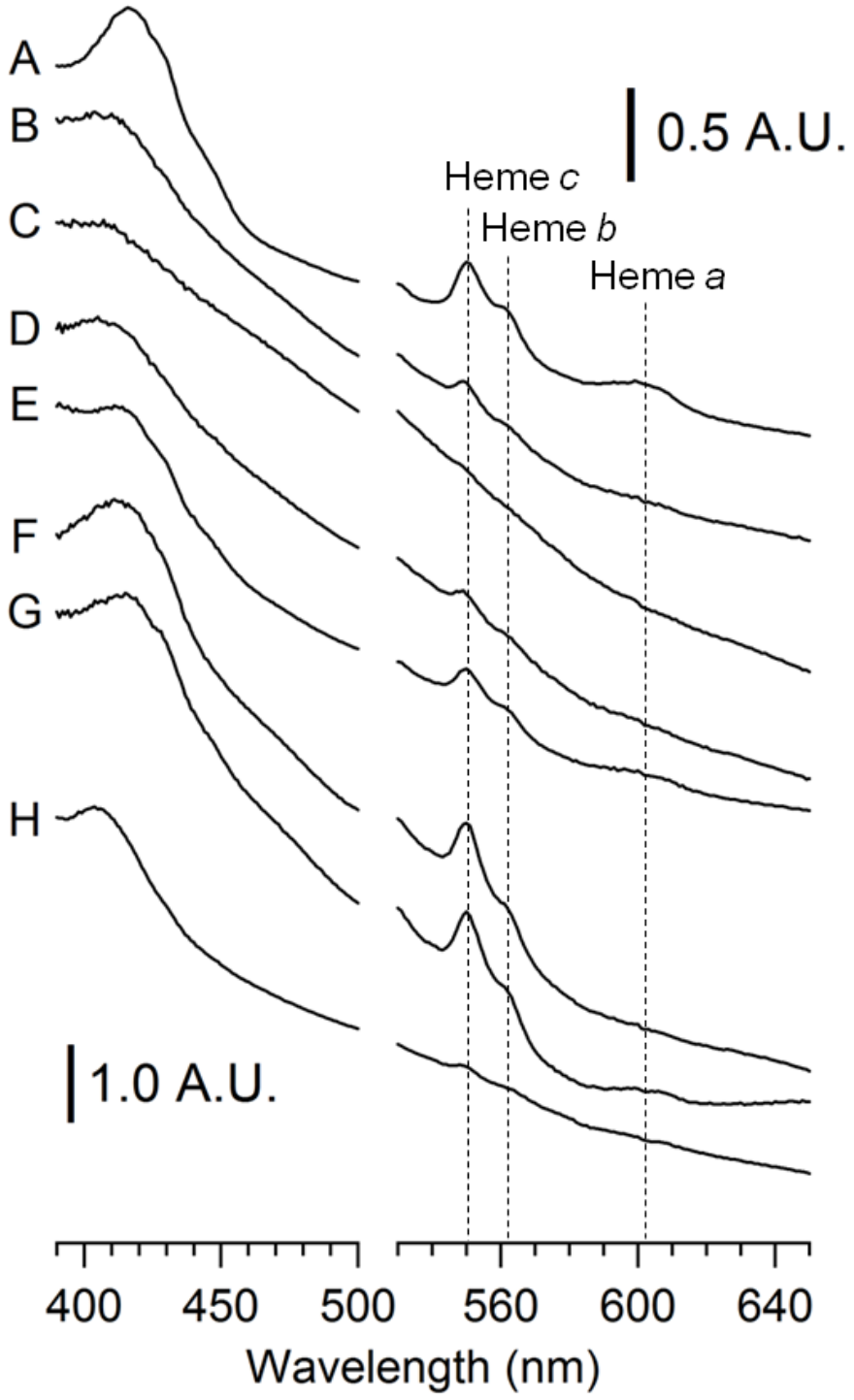

Figure IV-8. Electronic absorption spectra of 5 day-old cells grown on different media. A, G↓; B, MM; C, G↑; D, D+; E, RD+; F, YAB↑; G, AB↑; H, Y↑.

Cells grown for both 1 and 5 days on G↑ medium exhibited about 2-fold higher levels of oxidative damage relative to comparable MM-grown cells (Figure IV-6, right panel, compare lanes 2 vs. 1 for 1-day growth and lanes 7 vs. 6 for 5-day growth). Conversely, cells grown for both 1 and 5 days on G↓ medium displayed only *ca*. 30% of the oxidative damage observed in 1-day-old MM-grown cells (Figure IV-9). These results are consistent with previous reports that *the level of glycolysis determines oxidative stress of the cells*.[67,108,109]

We also grew cells in medium that contained 3 times the normal level of glucose (6% vs. 2%) and 10 times the normal level of Fe (400 *vs*. 40 μM). Cells grown on this G↑Fe↑ medium or on Fe↑ medium contained nearly 3 times more Fe relative to cells grown on G↑ medium (Table IV-2). The 5 K MB spectra of G↑Fe↑- (Figure IV-7D) and Fe↑-grown cells (Figure III-7A) were dominated by nanoparticles (50 - 70% spectral intensity) and HS Fe^{III} (10 - 15% intensity). Thus, adding extra Fe to the medium caused a massive increase of nanoparticles in the cell, but adding extra glucose in addition to the extra Fe did not cause any significant effect.

Amazingly, the extent of oxidative damage suffered by the nanoparticle-packed G↑Fe↑- grown cells after both 1 and 5 days of growth was about the same (or slightly less) than the oxidative damage in G↑-grown cells. In Figure IV-6, right panel, compare lanes 3 vs. 2 for 1 day growth and lanes 8 vs. 7 for 5 days growth. Again, the damage associated with 5 days of growth was *less* than in 1 day-old cells. This experiment demonstrates that *the formation of nanoparticles makes no detectable contribution to the extent of oxidative damage suffered by these cells*. The extent of damage might be

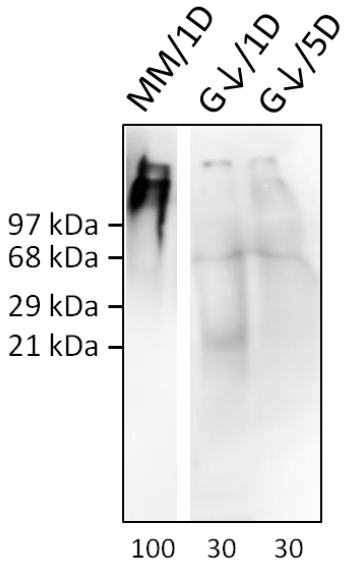

Figure IV-9. Oxyblot assay of whole cells grown on MM and G↓. MM/1D, 1-day old MM-grown cells; G↓/1D, 1-day old G↓-grown cells; G↓/5D, 5-day old G↓-grown cells. Band intensities were normalized based on MM/1D and displayed on the bottom of the blot. The image of MM/1D lane was cropped from the same membrane image and combined with images of G↓ lanes for easy comparison.

related to the location of the nanoparticles within the cell.

In previous studies, cells grown in medium containing as high as 10 mM did *not* show such high cellular Fe concentrations.[19] However, those cells were harvested towards the end of exponential phase (OD = 1.2). This suggests that the high Fe concentrations observed here arose because the stationary-state Fe import rate is sensitive to the Fe concentration in the growth medium; i.e. *this import process does not appear to be regulated in terms of Fe homeostasis*. In contrast, the Fe content of exponentially grown cells is tightly regulated.[104]

Rapamycin effect

Rapamycin dissolved in DMSO (200 μM) was added to MM (20 nM final concentration), affording the medium called RD+. RD+-grown cells grew slowly for 2 days (Figure IV-1D, filled diamonds), probably due to G0 arrest.[110] However, in the next 3 days rapamycin-treated cells reached a stationary state that had *ca*. 25% higher culture density ($OD_{600} \approx 2.9$) than MM-grown cells (Table IV-2). Control cells grown on MM spiked with DMSO (D+ medium) did not show any differences relative to the growth pattern of MM-grown cells (Figure IV-1D, open diamonds).

The Fe concentration of 5-day-old RD+ cells was ca. 7-fold less than that of MM-grown cells harvested at a similar age. This suggests that the Fe import rate of RD+-grown cells at stationary state was lower, relative to that of MM-grown cells. A similar effect on Fe import rate was implicated in cells grown on G↓ medium. In this respect, rapamycin and glucose exhibited opposite cellular responses.

The MB spectrum of RD+-grown cells exhibited a more intense NHHS Fe^{II} doublet relative to that of MM-grown cells (Figure IV-7E vs. Figure III-4E). The parameters associated with this doublet were within ± 0.1 mm/s of those used to simulate specie *b* in spectra of A↓-grown cells. The percentage of magnetic Fe in the sample (affording the HS Fe^{III} sextet and Fe^{III} nanoparticle doublet) was comparable to that of MM-grown cells. However, the overall Fe concentration was less. Considered together, these results confirm a previous report that inhibiting TORC1 lowers the magnetization in yeast cells.[63] It does this by reducing the amount of Fe that enters the cells and by shifting the Fe that does enter into non-magnetic forms.

The NHHS Fe^{II} doublet was not as intense in the spectrum of RD+-grown cells as it was in the spectrum of AB↑-grown cells (Figure IV-10D) while the Fe^{III} nanoparticle feature was twice as intense (Table IV-1). AB↑ medium contains three times the normal level of A (Leu, His, and Trp) and B (adenine and uracil) (*See* below). We don't understand the metabolic factors that control these Fe-associated effects. Naively, RD+-grown and AB↑-grown cells would appear to have more reducing cellular environments than MM-grown cells, with the difference more extreme with AB↑-grown cells.

Another interesting effect of inhibiting TORC1 was a reduced level of oxidative damage (Figure IV-6, lanes 5 and 10). The level of oxidative damage in 1-day old RD+ -grown cells was 2 – 4 times less than in cells grown on any other medium studied here. The extent of oxidative damage in 5-day old R↑-grown cells was also extremely low. In this respect, rapamycin and glucose again exhibited opposite effects, in that the extent of oxidative damage in G↑-grown cells was greatest of any condition studied here.

Effect of YNB, amino acids and nucleotide bases

Besides adenine, strain W303 is unable to synthesize uracil and 3 amino acids (Leu, His, and Trp) and so these were included in MM. Another requirement of these cells is YNB (which contains $(NH_4)_2SO_4$, vitamins, trace elements and salts). We modified MM such that the concentrations of YNB, amino acids, and bases were tripled relative to that in MM. The concentration of glucose in the resulting YAB↑ medium was also varied from 0.2% to 6%.

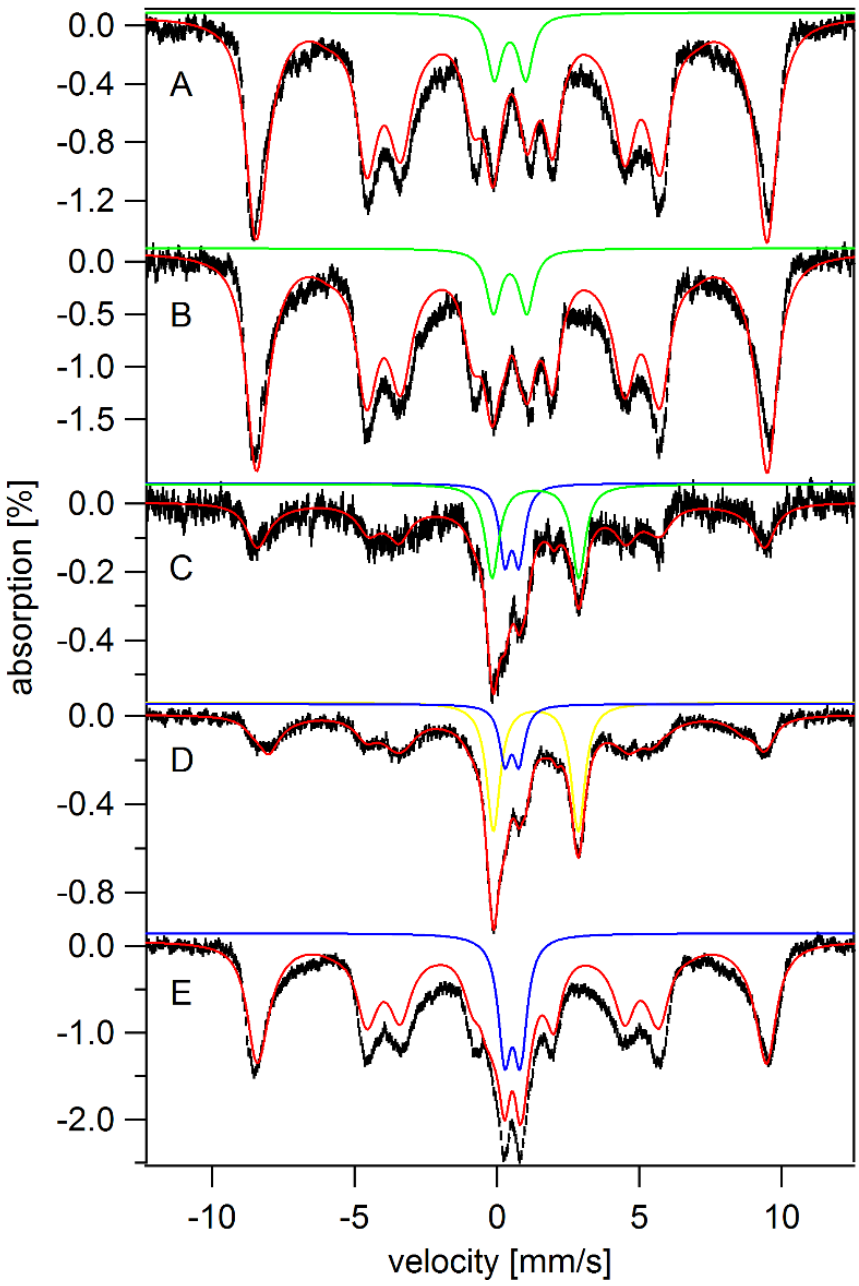

Figure IV-10. 5 K, 0.05 T Mössbauer spectra of whole yeast cells grown for 5 days on different media. A, YAB↑G↑; B, YAB↑; C, YAB↑G↓; D, AB↑; E, Y↑. Red lines are composite simulations including HS Fe^{III}, NHHS Fe^{II}, HS Fe^{II} heme, CD, Fe^{III} nanoparticle features. Blue, yellow and green lines are simulations of the Fe^{III} nanoparticle, NHHS Fe^{II} and CD features, respectively.

The density of YAB↑-grown cells at stationary state was proportional to the glucose concentration (Table IV-2), with YAB↑G↓-grown cells reaching densities ca. *40%* of that obtained by YAB↑-grown cells. Increasing the glucose concentration further did not stimulate cell growth much (ca. 10%). The Fe concentration in these cells also increased with the glucose concentration, yielding 420 μM, 1.8 mM, and 3.8 mM concentrations for YAB↑G↓-, YAB↑-, and YAB↑G↑-grown cells, respectively. These results suggest that either Y, A, or B limit the growth of G↑ cells.

MB spectra of YAB↑-grown (Figure IV-10A) and YAB↑G↑-grown (Figure IV-10B) cells were essentially identical in terms of Fe speciation. Approximately 90% of the intensities of both spectra consisted of the vacuolar HS Fe^{III} sextet, with no evidence of nanoparticles. Most of the remaining spectral intensity originated from the CD (Figure IV-10A and IV-10B, green line). This corresponds to a CD concentration of 110 – 160 μM Fe. Nanoparticles tend to form under neutral and basic pH conditions, so their absence here along with the dominance of vacuolar HS Fe^{III} suggests that the *vacuoles in YAB↑ cells are more acidic than those in MM-grown cells.* These vacuoles may also contain a high concentration of phosphate (and/or polyphosphate) which might allow more HS Fe^{III} to form.

The dominance of vacuolar HS Fe^{III} suggests that highly acidic vacuoles (or perhaps vacuoles containing high phosphate/polyphosphate levels) can "hold" HS Fe^{III} ions at a higher concentration than was previously assumed[19,46] and that they can occupy a greater percentage of the cell volume than had been assumed. We previously estimated a maximum [Fe] of 1.2 mM and that vacuoles could occupy a maximum of 25% of the

cell's volume. According to these ideas, filled vacuoles could contribute a maximum of ~ 300 μM to the total cellular Fe concentration. Contrasting this, YAB↑G↑ cells at stationary state contained 2.7 mM Fe, 90% of which was vacuolar HS Fe^{III} (Figure IV-10B and Table IV-1). If the vacuoles occupied 100% of the cell's volume, they would contain 2.4 mM Fe; if they occupied 25%, the Fe concentration in the vacuoles would be nearly 10 mM! Our previous estimate that the maximum [Fe] of vacuoles was clearly an underestimate.

The MB spectrum of YAB↑G↓-grown cells (Figure IV-10C) was less intense than that of YAB↑G↑-grown cells, consistent with a lower Fe concentration. More importantly, the effect of the additional YNB, amino acids and nucleotide bases (i.e. the hyper-accumulation of HS Fe^{III}) was essentially absent in cells grown on low-glucose medium.

In what ended up being a futile effort to identify the particular nutrient factor(s) responsible for the intriguing effect observed by growing cells on YAB↑ and sufficient glucose (i.e. 90% HS Fe^{III} and no nanoparticles), we prepared a MM-based medium containing only an excess of amino acids and nucleotide bases (AB↑). The growth rate of cells on AB↑ was similar to that using YAB↑ or YAB↑G↑ (Figure IV-1C, open *vs.* filled squares, and Table IV-2), while the Fe concentration of YAB↑-grown cells was less than that in AB↑-grown cells. Also, Y↑ cells accumulated less Fe than MM cells (5 mM vs. 7 mM). Thus, "Y" had little effect on cell growth but had a moderate negative effect on Fe accumulation.

In contrast, "Y" had a large effect on Fe speciation. The 5 K MB spectrum of AB↑ cells (Figure IV-10D) was substantially different from that exhibited by YAB↑ cells (Figure IV-10B). The AB↑ spectrum included the HS Fe^{III} sextet (50% spectral intensity), but the NHHS Fe^{II} doublet (30%) and the nanoparticle doublet (10%) also contributed significantly to overall intensity (Table IV-1). The parameters used in simulating this NHHS Fe^{II} doublet were again within ± 0.1 mm/s of those used to simulate specie *b* in the spectrum of A↓-grown cells.

AB↑-grown cells contained 990 μM Fe, suggesting a concentration of ~ 300 μM for the NHHS Fe^{II} species (Figure IV-10D and Table IV-1). This is substantially higher in absolute concentration than the equivalent component in MM-grown cells and is closer to what was seen for A↓-grown cells at transitionary state (~ 440 μM) or in RD+-grown cells (~ 150 μM). We have no compelling explanation for the observed Fe distribution; perhaps the vacuoles in AB↑-grown cells are more reducing and less acidic than those grown on YAB↑ medium.

Although these cells are expected to have a more reducing cellular environment, AB↑-grown cells suffered greater oxidative stress relative to MM-grown cells (Figure IV-6, right panel, lane 4, 9 *vs*. lane 1, 6). Faster-growing AB↑ cells may consume glucose faster (Figure IV-1C, open squares) to produce ROS at a higher rate. AB↑-grown cells, RD+-grown cells, and A↓-grown cells during the transitionary state contained unusually large concentrations of HS Fe^{II}, but the RD+- and A↓-grown cells were not as oxidatively stressed. The ROS response of AB↑-grown cells is undoubtedly

substantial, but not as strong as that of RD+- and A↓-grown cells. We conclude that the ROS response is stimulated by a process other than HS Fe^{II} formation.

We then prepared a medium that contained 3-fold more yeast nitrogen base and normal levels of amino acids and nucleotide bases. Cells did not grow as fast in the resulting medium (Y↑) as they did in YAB↑ and AB↑ media, but they grew slightly faster than in MM (Figure IV-1C, crossmarks vs. IV-1B, filled triangle and Table IV-2). The Fe concentration in Y↑-grown cells was higher than in cells grown on YAB↑ and AB↑ media (Table IV-2), implying that the additional amino acids and nucleotide bases in the latter media reduced the Fe import rate by increasing the growth rate.

The 5 K MB spectrum of Y↑ cells (Figure IV-10E) was nearly indistinguishable from that of 5-day-old MM-grown cells (Figure III-4E). Both exhibited an intense HS Fe^{III} sextet (67% of total spectral intensity) and an Fe^{III} nanoparticle doublet. Thus, the extra "Y" in the medium had no significant effect on Fe speciation. The spectrum of Y↑-grown cells was comparable to that YAB↑-grown cells (Figure IV-10B), in that the dominant species in both cases was the sextet. However, the nanoparticle doublet and the unresolved magnetic nanoparticle feature contributed substantially to the Y↑ spectrum but not to the YAB↑ spectrum. Unfortunately, we are unable to explain these effects on the molecular level. The extra "A" and "B" concentrations in the medium somehow suppress nanoparticle formation (perhaps by making vacuoles more acidic or more reducing). The lesson here is that the metabolic effects of increasing Y and AB in MM medium are not additive, undoubtedly due to the complexity of cellular metabolism.

Heme levels in cells under different nutrient status

Under typical growth conditions, the majority (65 – 75%) of cellular Fe is associated with vacuoles.[19,78,81] Thus, much of the variations in Fe content observed in this study reflect Fe chemistry occurring within this organelle. Mitochondria also play an important role in Fe metabolism, but typically only ~ 20% of cellular Fe is associated with this organelle. Thus, observing changes in mitochondrial Fe by MB spectroscopy is difficult, especially under conditions in which nonmitochondrial spectral features (e.g. the nanoparticle doublet) obscure the CD. We therefore used electronic absorption spectroscopy to estimate the mitochondrial Fe level - by measuring the intensity of heme spectral features. The majority of heme centers in the cell are associated with mitochondrial respiration-related proteins.

Using this reporter, we found that mitochondrial Fe appears to have been affected significantly by nutrient status (Figure IV-8). As the initial level of glucose in media increased, reduced heme levels in 5-day-old cells decreased dramatically (Figure IV-8A-C). Additional "YAB" (Figure IV-8F) and "AB" (Figure IV-8G) increased cellular reduced heme concentrations (consistent with the intense CD in MB spectra of cells grown under these conditions) while additional Y (Figure IV-8H) alone did not (consistent with the lack of CD in the corresponding MB spectrum). Rapamycin treatment (Figure IV-8E *vs.* IV-8D) promoted high reduced heme levels, consistent with an increased dependence on respiration. Curiously, the percentage of the CD in the RD+ MB spectrum was only ~ 3% (which seems low relative to the intensity of the heme

signals). Collectively, the effect of nutrient changes and rapamycin on mitochondrial Fe appears to be as significant as their effect on vacuolar Fe.

Discussion

The effect of glucose on yeast Fe metabolism suggests that the low-affinity Fe importer (probably involving FET4)[21] is regulated (directly or indirectly) by the glucose concentration in the cell. High glucose concentrations *increase* the rate of Fe import while lower glucose concentrations *decrease* that rate. Since glucose concentrations do not affect the rate of cell growth, this leads to an accumulation of Fe in the cell under high glucose levels. Glucose also represses cellular respiration[47] which explains the decline of Fe/S clusters and heme centers that are generally associated with mitochondria. The extent of oxidative stress is also modulated by the initial level of glucose in media. The more glucose, the more the cells were oxidatively stressed.

Similar effects of glucose on the Fe concentration and oxidative stress of cells have been reported by Reverter-Branchat *et al*.[67] They grew cells on rich media supplemented with 2% (w/v) and 0.5% (w/v) glucose and monitored for [Fe] and oxidative stress during two months and 16-18 generations. They observed stronger oxidative stress and higher [Fe] in cells fed more glucose. They concluded that the pro-oxidant effects due to the increased Fe caused the enhanced damage. We demonstrated here that the oxidative stress is not directly related to the level of cellular Fe, but more closely related to glucose metabolism.

How glucose promotes ROS generation in yeast is not known yet, but multiple biochemical pathways in which glucose metabolism can generate ROS in mammalian cells have been reported, including glyceraldehyde autoxidation, protein kinase C activation and oxidative phosphorylation.[111] Glucose suppresses a nutrient-dependent protein kinase (Rim15p) that regulates the expression of genes involved in antioxidant defense such as *SOD1* and *SOD2*, thereby increasing cellular ROS damage.[112]

The effects of adenine deficiency can also be explained somewhat on the molecular/cellular level. Yeast cells that are mutated in ADE2, grown under adenine-deficient conditions, and harvested during the transition from exponential growth to the stationary state lack HS Fe^{III} and contain high concentrations of at least two NHHS Fe^{II} complexes. These complexes may simply be the reduced forms of the NHHS Fe^{III} species whose spectral intensity declined. Ligands may have also exchanged during reduction. The location(s) of the NHHS Fe^{II} complexes is(are) also unknown. Our previous model[46] included vacuolar Fe^{III} species exiting the vacuole once the lumen of the organelle was reduced. Assuming this, the NHHS Fe^{II} species observed here should be located in the cytosol. Alternatively, vacuoles may become more reducing under adenine-deficient conditions and the NHHS Fe^{II} species might remain in the vacuole. Our experiments cannot distinguish these possibilities.

The reduction of vacuolar HS Fe^{III} may involve the glutathione (GSH)-mediated detoxification pathway which is up-regulated when the adenine precursor phosphoribosylaminoimidazole (AIR) accumulates in the cytosol.[70] Since the ADE2 gene-product converts AIR to AIR carboxylate (CAIR), adenine-deficient W303 cells

accumulate toxic AIR in the cytosol which activates this pathway. GSH forms a "conjugate" with AIR, which then is transported into vacuoles via the glutathione-conjugate (GS-X) pump.[70] Once in the vacuole, AIR polymerizes to form a red pigment. A degradation product of the glutathione conjugate (conceivably cysteine) may reduce the vacuolar lumen, including the vacuolar Fe^{III} contained therein. The reduced Fe may be exported via Smf3p, a divalent metal transporter located on the vacuolar membrane.[113] Further studies are required to establish this mechanism.

After the transition to stationary state, the NHHS Fe^{II} species (in most batches) reoxidized back to the Fe^{III} state, including both HS Fe^{III} and Fe^{III} nanoparticles, as is also observed in adenine-sufficient cells. Why vacuoles should get more oxidized as the cell goes into stationary state is unclear. The cysteine concentration in the vacuole might decline in stationary state cells, in that cellular metabolism might be less active and less AIR might be produced. This would slow the Fe export from the vacuole to cytosol, resulting in an accumulation of HS Fe^{III} in the vacuole. Vacuolar pH might rise in stationary state cells,[102] promoting nanoparticle formation.

Understanding the effects of adenine-deficiency and other nutrient effects reported here can be enhanced using the thermodynamic box shown in Figure IV-11. This box represents hypothetical transformations of Fe that may occur within yeast vacuoles. Two factors control those transformations, including redox state and the pH of the vacuole. Starting at the upper-left corner, Fe^{II} enters the vacuole in a protonated state (in which a ligand to the Fe, rather than the Fe itself, is protonated). This species can become oxidized to $Fe^{III}(H^{+})$, in accordance with a half-cell reduction potential

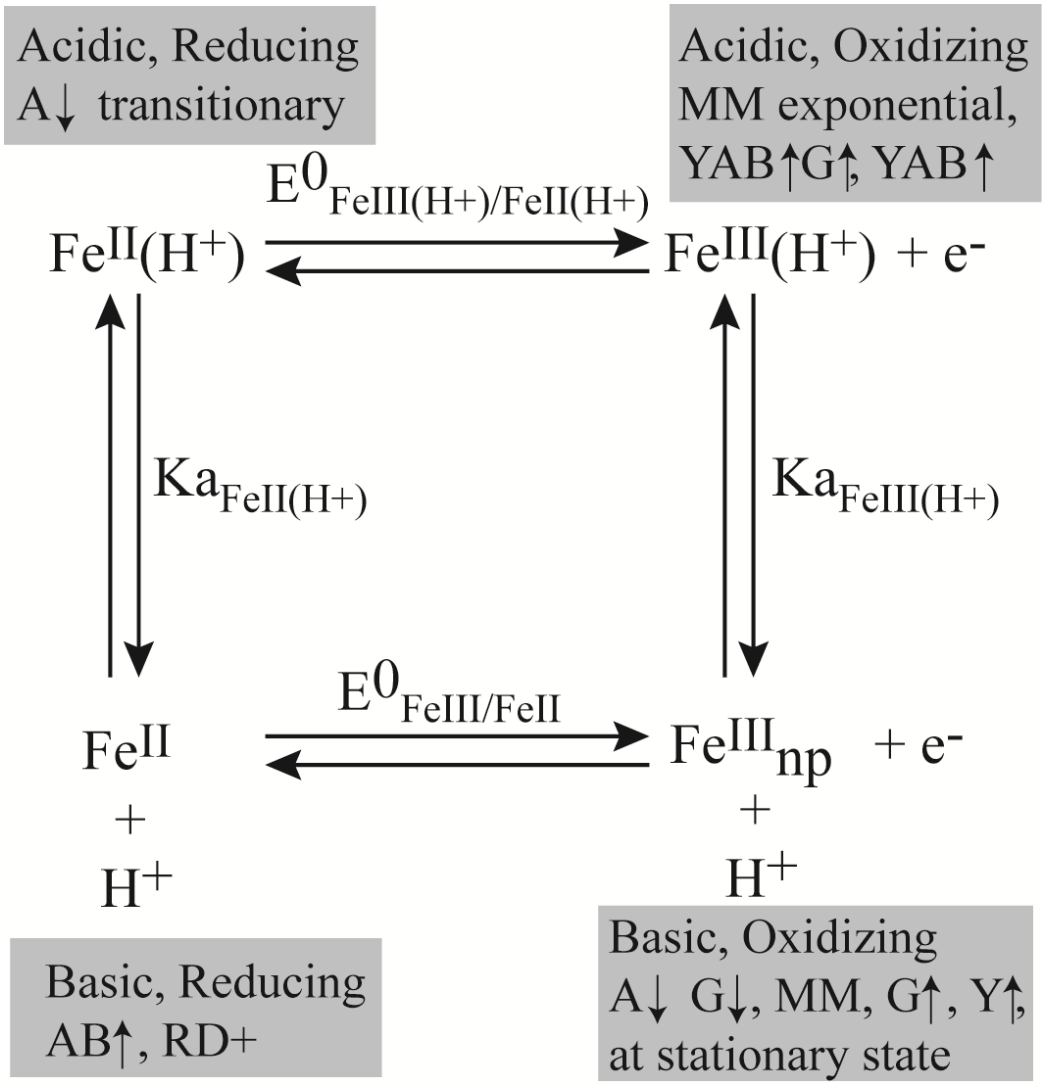

Figure IV-11. Model of Fe transformations in yeast vacuoles. $Fe^{II}(H^+)$ and $Fe^{III}(H^+)$ correspond to NHHS Fe^{II} and vacuolar HS Fe^{III} , respectively, with protonated ligand(s). Fe^{II} and Fe^{III}_{np} represent NHHS Fe^{II} with deprotonated ligand(s) and Fe^{III} nanoparticles, respectively. $E^0_{Fe^{III}(H^+)/Fe^{II}(H^+)}$ and $E^0_{Fe^{III}/Fe^{II}}$ are half-cell reduction potentials of vacuolar HS $Fe^{III}(H^+)$/NHHS $Fe^{II}(H^+)$ and Fe^{III} nanoparticles/NHHS Fe^{II}. $Ka_{Fe^{II}(H^+)}$ and $Ka_{Fe^{III}(H^+)}$ are acidity equilibrium constants of $Fe^{II}(H^+)$ and $Fe^{III}(H^+)$. More acidic and oxidizing conditions increase the percentage of $Fe^{III}(H^+)$ (MM-grown cells at exponential phase, YAB↑G↑ and YAB↑-grown cells at stationary phase). Less acidic but more oxidizing conditions increase the percentage of Fe^{III}_{np} (A↓, G↓, MM, G↑, and Y↑-grown cells at stationary phase). Less acidic and more reducing conditions increase the percentage of Fe^{II} and Fe^{III}_{np} (AB↑, RD+-grown cells at stationary phase). More acidic and reducing conditions increase the percentage of $Fe^{II}(H^+)$ (A↓-grown cells at transitionary phase).

$E^0_{Fe^{III}(H^+)/Fe^{II}(H^+)}$. $Fe^{III}(H^+)$ can deprotonate forming Fe^{III} nanoparticles; the acidity equilibrium constant for this process is $Ka_{Fe^{III}(H^+)}$. Analogous parameters describe the deprotonation of $Fe^{II}(H^+)$ to Fe^{II} ($Ka_{Fe^{II}(H^+)}$) and the oxidation of Fe^{II} to Fe^{III} nanoparticles ($E^0_{Fe^{III}/Fe^{II}}$). These relationships imply that

$$E^0_{FeIII(H+)/FeII(H+)} - E^0_{FeIII/FeII} = \frac{RT}{n\Im} \ln \frac{Ka_{FeIII(H+)}}{Ka_{FeII(H+)}}$$

where n = 1 and R, T and $\Im$ have their usual meanings. Under standard growth conditions (i.e. exponentially grown cells in MM), the dominant species present in the vacuoles is $Fe^{III}(H^+)$. This implies that $E^0_{FeIII(H+)/FeII(H+)} < E^0_{FeIII/FeII}$ and that $Ka_{FeIII(H+)} < Ka_{FeII(H+)}$ (i.e. $Fe^{II}(H^+)$ is a more powerful reductant than Fe^{II} and a stronger acid than $Fe^{III}(H^+)$). Under standard conditions, the vacuoles are acidic, with pH ~ 5.[39] If $pKa_{Fe^{II}(H^+)}$ and $pKa_{Fe^{III}(H^+)}$ were both >> 5, then the top row of the box would be more populated, such that most vacuolar Fe species would be protonated and few nanoparticles would be present. Under oxidizing conditions, the dominant species present in any substantial amounts would be NHHS $Fe^{III}(H^+)$ – as observed. The effect of adenine deficiency would be to shift the box to more reducing conditions, such that $Fe^{II}(H^+)$ and Fe^{II} would dominate.

The effect of rapamycin is roughly the opposite of glucose but its effect is actually more complicated. Lowering TORC1 activity by rapamycin treatment or knockout of Tco89p, a component of TORC1, is known to reduce the magnetization of yeast grown on high Fe-containing media, cause G0 growth arrest and increase respiration.[61,63,108] Consistent with that, we found that rapamycin inhibited the rate of Fe

import (and inhibited cell growth during a lag period occurring prior to exponential growth) and promoted respiration. These effects are opposite of those caused by glucose. Unlike glucose, rapamycin altered the distribution and speciation of cellular Fe. Viewed from the perspective of the thermodynamic box, rapamycin shifts the vacuole to more basic conditions such that the lower row of the box becomes more populated. In contrast to the top row in which the oxidized state dominates, Fe^{II} is not as strong of a reductant as $Fe^{II}(H^{+})$, such that it and its oxidized counterpart (Fe^{III} nanoparticles) can coexist, as observed. Rapamycin-treated cells may also be more reducing than normal, as was observed in the Tco89p knockout strain,[63] so as to allow the presence of Fe^{II} together with some Fe^{III} nanoparticles.

The rapamycin effect is consistent with previous reports that rapamycin increases life span in many organisms including yeast.[61] The increased final OD_{600} by rapamycin treatment implies an extended replicative life span. Also, the reducing cellular environment induced by rapamycin supports a model in which reduced TORC1 activity promotes chronological life span by increasing Rim15p-dependent and Rim15p-independent expression of environmental stress-response genes such as *SOD1* and *SOD2*.[65,66,114] The decreased level of oxidative stress in rapamycin-treated cells supports this model.

The addition of extra amino acids and nucleotide bases discourages cells from accumulating Fe^{III} nanoparticles and encourages them to form HS Fe^{II} as TOR-inhibition does. This condition reduces the magnetization of the cells grown with high Fe in the medium[63], probably by rendering the redox state of the cell more reducing. This suggests

an explanation for why such cells contain high concentrations of NHHS Fe^{II}. Alternatively, both conditions appear to promote respiration according to the high heme levels (Figure IV-8E and IV-8G). Under such growth conditions, cells usually produce more antioxidants such as GSH,[115] perhaps resulting in a more reducing cellular environment. Both conditions might increase the availability of excess amino acids and nucleotide bases. Lowered TORC1 activity decreases protein synthesis and increases the general amino acid permease on the plasma membrane.[47,61] Such circumstances might allow cells to avoid a particular amino acid synthetic pathway that might promote a more oxidizing environment or an increased vacuolar pH. In this respect, vacuoles play an important role in protein degradation and amino acid recycling.[116]

In summary, we found that the Fe concentration, speciation and distribution in yeast could be altered dramatically by changing the concentrations of nutrients in the growth medium. Cellular metabolism is exceedingly complicated, such that the observed alterations could not be fully explained on the molecular level. Nevertheless, we have developed a model in which the redox status and pH of the vacuole plays a major role in determining the Fe concentration, distribution, and speciation in yeast cells. Our ability to alter Fe metabolism by changing nutrient components illustrates the sensitivity of cellular Fe distribution and speciation on the nutrient composition of the medium. It also highlights the importance of specifying the growth medium and harvesting conditions in reporting and interpreting results involving cellular Fe metabolism.

CHAPTER V

INSIGHTS INTO THE IRON-OME AND MANGANESE-OME OF Δ*MTM1* *SACCHAROMYCES CEREVISIAE*[*]

Introduction

The Mtm1p protein found in the budding yeast *Saccharomyces cerevisiae* is a member of the mitochondrial carrier family.[53,56] Located in the mitochondrial inner membrane (IM), members of this family transport low-molecular-mass (LMM) species between the cytosol and the matrix of the organelle. The substrate transported by Mtm1p has not been identified and so the exact cellular function of the protein is unknown. Carriers can be organized according to whether their substrates are nucleotides, carboxylates, or amino acids, with Mtm1p in the last group.[117] Substrates tend to be negatively charged and carriers often catalyze an exchange in which protons move in opposition to substrates.

Deleting the *MTM1* gene partially inactivates Mn superoxide dismutase (MnSod2p),[53,54] suggesting that Mtm1p might be involved in Mn metabolism. During maturation, apo-Sod2p issent to the mitochondrial matrix where Mn is installed during folding, suggesting that Mtm1p either imports Mn or is a chaperone for that installation.

---

[*] This chapter is reproduced with permission from: "Insights into the iron-ome and manganese-ome of Δ*mtm1 Saccharomyces cerevisiae* mitochondria" by Jinkyu Park, Sean P. McCormick, Mrinmoy Chakrabarti and Paul A. Lindahl, *Metallomics*, 2013, **5**, 656-672, Copyright 2013 The Royal Society of Chemistry

However, the Mn concentration within Δ*mtm1* mitochondria is elevated relative to that of WT mitochondria,[53] discounting the possibility that Mtm1p imports Mn.

Attention shifted to Fe metabolism when Sod2p was found to be inactivated in association with an elevation of Fe in Δ*mtm1* cells.[53,54] Genetic and chromatographic results suggest that an *Apo-Sod2p-Reactive* (ASR) pool of Fe in the matrix (referred to as Fe_{ASR}) competes with Mn ions for installation into the active-site of apo-Sod2p. Indeed, Fe misincorporates into superoxide dismutases, a process that prevents the apo-enzyme from being activated by Mn.[57] The size of the Mn pool in yeast mitochondria varies with the concentration of Mn in the growth medium.[53] The mitochondrial Fe concentration increases under Mtm1p-deficient conditions.

The extent of Fe misincorporation appears related to the Fe concentration in the growth medium, in that Fe-deficient conditions (created by adding the chelator bathophenanthroline disulfonate) prevent both Fe accumulation and loss of SOD2 activity in *Δmtm1* mitochondria.[54] Misincorporation is also prevented by additionally deleting *MRS3/4*, the genes encoding high-affinity Fe transporters on the mitochondrial IM.[54] This suggests that the Fe_{ASR} pool enters the mitochondria through Mrs3p/4p.

A single Mn species, associated with MnSod2p, was identified in fractions obtained by passing WT mitochondrial extracts through an anion-exchange column;[54] no such species was observed with Δ*mtm1* extracts. Replacing this peak in chromatograms of Δ*mtm1* mitochondrial extracts was a dominating Fe peak that co-eluted with Sod2p. This peak, attributed to FeSod2p, was absent in extracts of a Δ*mtm1* Δ*sod2* double-deletion mutant. This was the only Fe-containing peak evident in soluble Δ*mtm1*

extracts, and the peak was absent in WT extracts. This suggested that the majority of the soluble Fe in Δ*mtm1* mitochondrial extracts that eluted through the column was misincorporated into apo-Sod2p.

The situation is actually more complicated in that a deficiency of Mtm1p is not unique in causing Fe to accumulate or misincorporate.[54] Depleting the cell of Ssq1p, Grx5p, and Atm1p also causes Fe to accumulate in mitochondria and Sod2p to partially inactivate. These proteins are involved in mitochondrial Fe metabolism, but they have distinct functions. Ssq1p is a soluble Hsp70-family chaperone that helps install nascent Fe/S clusters into recipient apo-Fe/S proteins.[118] Atm1p is a mitochondrial IM ABC transporter that exports an unknown sulfur-containing species required for cytosolic Fe/S cluster assembly.[52] Grx5p is a monothiol glutaredoxin that binds the scaffold proteins Isa1p/Isa2p.[119] Based on these diverse functions, it would appear that neither apo-Sod2p-misincorporation nor Fe accumulation in mitochondria are *primary* effects of Mtm1p deficiency. Rather, they appear to be *secondary* effects arising in mitochondria lacking Mtm1p, Grx5p, Ssq1p, or Atm1p.

Another complexity is that Fe accumulation and misincorporation appear to be independent of each other. The absence of certain mitochondrial proteins, e.g. yeast frataxin homolog Yfh1p[120] and the scaffold protein Isu1p, cause Fe accumulation but not misincorporation. Interestingly, the proteins which, when depleted in cells, cause Fe to accumulate but NOT misincorporate (e.g. Yfh1p and Isu1p) help *build* Fe/S clusters. In contrast, proteins which, when lacking, cause both Fe accumulation AND misincorporation (i.e. Atm1p, Grx5p, and Ssq1p) may help *transfer* assembled clusters

into recipient apo-proteins.[55] This correlation implies that Mtm1p functions in cluster transfer, not assembly. The misincorporated Fe has been proposed to originate from the Fe/S cluster donated by Isu1p. This is consistent with the increased level of Isu1p in Δ*mtm1* cells relative to in WT cells[55,121] in that the cell may compensate for a deficiency of Fe/S clusters by increasing Isu1p levels.

Another complexity in understanding the Δ*mtm1* phenotype is that the *type* of Fe that accumulates in Atm1p-depleted mitochondria (and in Δ*yfh1* and Yah1p-depleted mitochondria) is ferric oxyhydroxide (phosphate or polyphosphate) nanoparticles.[80,83,122] This insoluble form of Fe seems unlikely to insert into apo-Sod2p; we would expect that soluble Fe^{II} ions insert. Also, the size of the Fe_{ASR} pool is unknown. It should enlarge in strains lacking Mtm1p, Atm1p, Grx5p, and Ssq1p, relative to in WT cells, but there is no certainty that the majority of the Fe that accumulates in the mitochondria of these strains is that particular pool of Fe.

To address this question, X-ray absorption spectroscopy (XAS) was performed on Δ*mtm1* mitochondria as well as on mitochondria from a control mutant (*rho*$^-$) that also accumulates Fe but exhibits normal SOD2 activity when the growth medium is supplemented with 2 mM Fe.[55] No difference in the properties of the accumulated Fe, including oxidation state, geometry, or ligand environment, could be discerned. This suggests that the Fe_{ASR} pool that misincorporates into apo-Sod2p must be quite *small* – so small that it is undetectable by XAS.

Mtm1p has also been suggested to function in heme biosynthesis. One of the five mitochondrial proteins that coexpresses with other proteins involved in heme

biosynthesis in zebrafish is an ortholog of yeast Mtm1p.[121] Silencing this gene prevented Fe incorporation into protoporphyrin IX. This suggests that this Mtm1p-like protein is involved *early* in heme biosynthesis, i.e. prior to insertion by ferrochelatase, perhaps by regulating *d*-aminolevulinate synthase, the committed step in heme biosynthesis.

Previously, we studied the iron-ome of mitochondria from WT and mutant strains related with mitochondrial Fe/S and heme biosynthesis.[35,80,83] The iron-ome of fermenting WT mitochondria is mainly composed of Fe/S clusters, heme centers, HS $Fe^{II/III}$, and Fe^{III} nanoparticles. However, mutant mitochondria commonly exhibit a dominant Fe^{III} nanoparticle feature, and are largely devoid of intact Fe/S clusters and heme centers. In this paper, we describe the iron-ome of mitochondria from Δ*mtm1* yeast using biophysics and liquid chromatography (LC) in conjunction with an on-line inductively coupled plasma mass spectrometer (ICP-MS). Similarly to the previous studies, most of the accumulated Fe is present as Fe^{III} oxyhydroxide nanoparticles, which is unlikely to misincorporate into apo-Sod2p. LMM Mn and Fe species were observed in mitochondrial extracts that could potentially represent the sought-after pools. An Fe-containing protein comigrated approximately with MnSOD-containing fractions, but the relative level of this protein was similar in both WT and Δ*mtm1* mitochondria. We conclude that deleting *MTM1* diminishes SOD2 activity in a manner that does not involve Fe misincorporation, and suggest alternative cellular functions for this protein.

Results

Mitochondria from aerobically grown WT and Δmtm1 cells

Mitochondria were isolated from WT cells grown under fermenting conditions on minimal medium supplemented with 20μM ^{57}Fe. The concentrations of metal ions in the organelle (Table V-1) were similar to previous reports.[35] The samples also exhibited a low-temperature (5 K), low-field (0.05 T) Mössbauer spectrum similar to that reported.[35] The major spectral feature (Figure V-1A and Table V-2) was the central doublet (CD; $\delta \approx 0.44$ mm/s, $\Delta E_Q \approx 1.2$ mm/s) due to S = 0 $[Fe_4S_4]^{2+}$ clusters and low spin (LS) Fe^{2+} hemes. Two minor quadrupole doublets were evident, including one ($\delta \approx$ 1.4 mm/s, $\Delta E_Q \approx 3.2$ mm/s) arising from non-heme high-spin (NHHS) Fe^{II} species and the other ($\delta \approx 0.96$ mm/s, $\Delta E_Q \approx 2.26$ mm/s) arising from high spin (HS) Fe^{II} hemes. The remaining intensity included contributions from Fe^{III}oxyhydroxide (phosphate or polyphosphate) nanoparticles and/or S = 0 $[Fe_2S_2]^{2+}$ clusters, but the resolution was insufficient to distinguish these. The former species has been observed in previous preparations of yeast mitochondria grown under similar conditions. The latter species has been identified recently in mitochondria isolated from Fe-deficient cells,[19] and is probably present (but more difficult to distinguish) in mitochondria from Fe-sufficient cells. The simulation that overlays the spectrum of Figure V-1A includes all of these contributions, with the percentages given in Table V-2.

Table V-1. Properties of mitochondria and whole cells used in this study. [a] Standard error; [b] Number of batches; [c] 200 µM Mn-supplemented medium; [d] mitochondrial suspensions; [e] cell lysates; * Activities and protein expression level were quantified from activity gels and western blotting membranes; ** Specific activity = relative SOD2 activity divide by the relative Sod2p expression level.

	W303/O_2	Δ*mtm1*/O_2	W303/Ar	Δ*mtm1*/Ar	Gal-Yah1/O_2
$[protein]_{mito}$ (mg/ml)	79 ± 14[a] (3)[b]	57 ± 9 (3)	70 ± 5 (2)	59 ± 11 (3)	-
$[Fe]_{mito}$ (µM)	880 ± 250 (3) 620[c]	3500 ± 400 (3) 5200[c]	400 ± 20 (2)	440 ± 70 (3)	-
$[Mn]_{mito}$ (µM)	13 ± 1 (3) 35[c]	26 ± 9 (3) 80[c]	8 ± 0 (2)	19 ± 3 (3)	-
Aconitase[d] (units/mg protein)	1500 ± 45 (2)	350 ± 69 (3)	1500 ± 350 (2)	1100 ± 130 (3)	-
SDH[d] (units/mg protein)	23 ± 4 (2)	2 ± 1 (3)	7 ± 1 (2)	8 ± 3 (3)	-
$[Fe]_{cell}$ (µM)	640 ± 98 (3) 1000[c]	4900 ± 120 (2) 2400[c]	640 ± 13 (2)	660 ± 190 (2)	-
$[Mn]_{cell}$ (µM)	35 ± 8 (3) 110[c]	41 ± 1 (2) 75[c]	39 ± 1 (2)	37 ± 7 (2)	-
Leu1p[e] (units/mg protein)	48 ± 8 (3)	30 ± 13 (3)	100 ± 13 (3)	41 ± 10 (3)	-
Relative SOD2 activity*	100	26 ± 6 (3)	66 ± 7 (3)	14 ± 3 (3)	89 ± 17 (3)
Relative Sod2p expression level*	100	71 ± 12 (3)	77 ± 19 (3)	36 ± 5 (3)	108 ± 28 (3)
Relative Specific SOD2 activity**	100	42 ± 16 (3)	102 ± 34 (3)	42 ± 12 (3)	87 ± 11 (3)

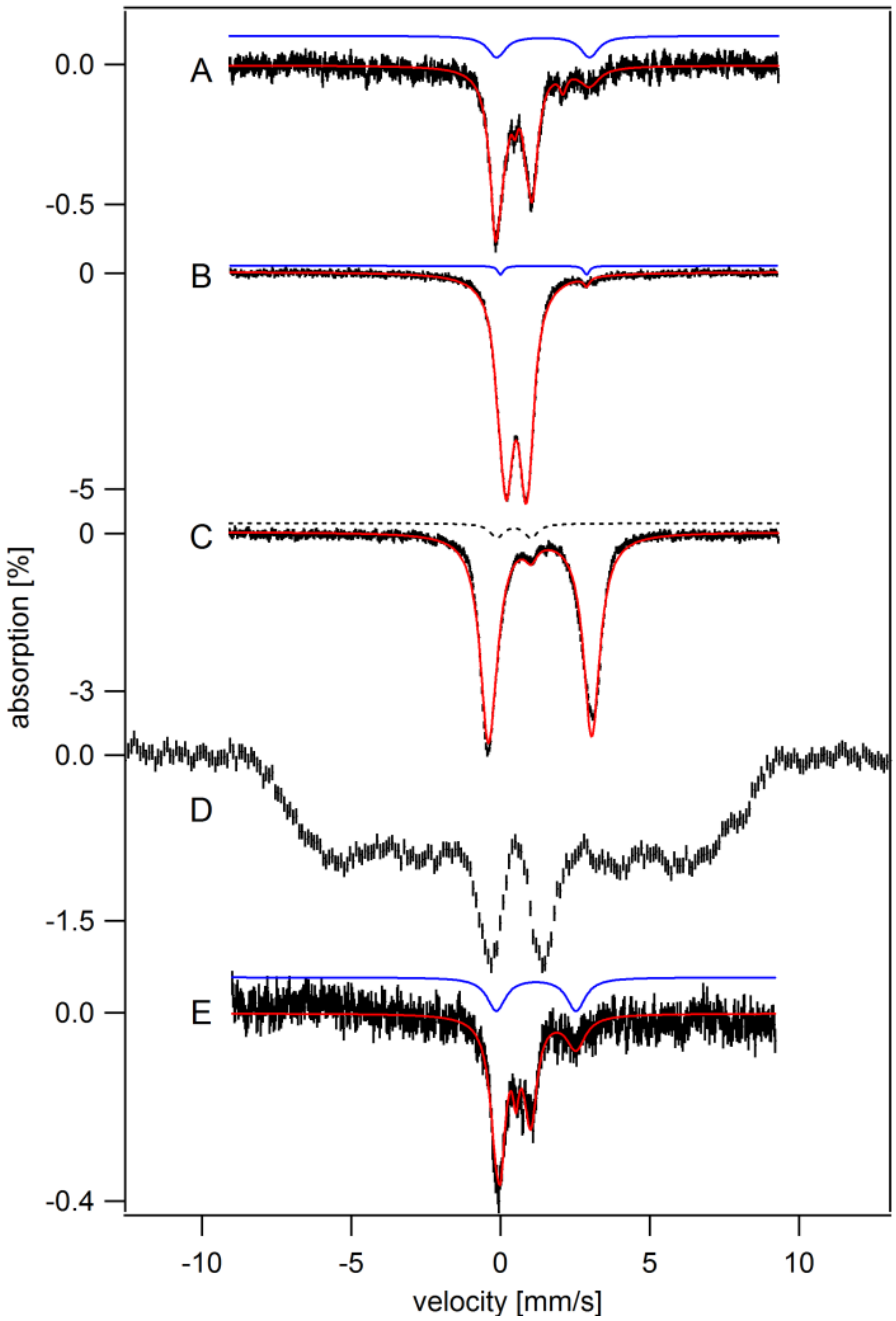

Figure V-1. 5 K Mössbauer spectra of isolated mitochondria from W303 and Δ*mtm1* cells. A, W303/O_2; B, Δ*mtm1*/O_2; C, Δ*mtm1*/O_2/dithionite-reduced; D, same as in B but at 8 T; E, *mtm1*Δ/Ar. Spectra other than D were collected with 0.05 T applied field. Red solid lines are simulations (using components and percentages given in Table S1). Blue solid lines in A, B and E simulate the contribution of NHHS Fe^{II} species. The dashed line in C is a simulation that indicates the contribution of the central doublet.

Table V-2. Isomer shift (δ, mm/s), quadrupole splitting (ΔE_Q, mm/s), line width (Γ, mm/s), and percentage of Fe species as determined from Mössbauer spectra used in Chapter V. Red-colored parameters were fixed when simulated.

Spectrum	Central doublet	NHHS Fe^{2+}	HS Fe^{2+} heme	$[Fe_2S_2]^{2+}$	Fe^{III} nano-particle	HS Fe^{3+}
W303/O_2 mitochondria (Fig. 1A)	0.44/1.23/ 0.47, 59%	1.40/3.17/ 0.79, 15%	0.96/2.26/ 0.27, 5%	0.25/0.46/ 0.25, 8%	0.52/0.63/ 0.26, 6%	7%
Δ*mtm1*/O_2 mitochondria (Fig. 1B)	0.45/1.15/ 0.28, 5%	1.44/2.89/ 0.23, 2%	-	-	0.52/0.67/ 0.58, 93%	-
Δ*mtm1*/O_2 mitochondria, dithionite-reduced (Fig. 1C)	0.45/1.15/ 0.48, 5%	1.32/3.47/ 0.66, 94%	-	-	0.52/0.67/ 0.35, 1%	-
Δ*mtm1*/Ar mitochondria (Fig. 1E)	0.45/1.15/ 0.48, 50%	1.19/2.67/ 0.76, 26%	-	0.27/0.49/ 0.25, 14%	0.52/0.67/ 0.34, 4%	5%
W303/O_2 whole cell (Fig. 5A)	0.45/1.15/ 0.46, 13%	1.30/3.10/ 0.70, 2%	0.83/2.26/ 0.94, 7%	0.27/0.49/ 0.50, 3%	-	75%
Δ*mtm1*/O_2 whole cell (Fig. 5B)	1 ~ 2%	1.36/2.99/ 0.52, 11%	-	-	0.53/0.58/ 0.58, 69%	19%
W303/Ar whole cell (Fig. 5C)	0.45/1.15/ 0.83, 9%	1.29/2.89/ 0.58, 16%	0.83/2.58/ 0.28, 3%	0.27/0.49/ 0.79, 10%	0.52/0.63/ 0.47, 8%	55%
Δ*mtm1*/Ar whole cell (Fig. 5D)	0.45/1.15/ 0.43, 5%	1.32/2.98/ 0.60, 20%	0.83/2.32/ 0.30, 2%	0.27/0.49/ 0.46, 8%	0.52/0.58/ 0.26, 5%	61%
W303/Ar mitochondria (Fig. S1)	0.45/1.15/ 0.43, 45%	1.14/2.77/ 0.27, 12%	-	0.27/0.49/ 0.30, 21%	0.52/0.63/ 0.19, 2%	20%

Mitochondria isolated from Δ*mtm1* cells grown under similar conditions contained 4-times more Fe than did WT mitochondria (Table V-1). The 5 K, 0.05 T Mössbauer spectrum of Δ*mtm1* mitochondria (Figure V-1B) was dominated by a broad quadrupole doublet ($\delta \approx 0.52$ mm/s, $\Delta E_Q \approx 0.67$ mm/s) due to nanoparticles. This was confirmed by the 4.2 K, 8 T spectrum (Figure V-1D) which was indistinguishable from the high-field spectra of other mutant mitochondria whose Fe contents were also dominated by nanoparticles.[80,83] Phosphorus, most likely in the form of phosphate or polyphosphate ions, are associated with nanoparticles in Atm1-depleted, Yah1-depleted, Ssq1-deficient, and Yfh1-deficient cells,[80,83,122,123] and we presume that similar species are associated with the nanoparticles in Δ*mtm1* mitochondria.

The 5 K, 0.05 T Mössbauer spectrum of Δ*mtm1* mitochondria also exhibited a low-intensity quadrupole doublet with a high-energy line at ~ 2.9 mm/s (Figure V-1B, blue line). The low-energy line of this doublet is buried within the nanoparticle doublet, but we estimate parameters of $\delta \sim 1.4$ mm/s and $\Delta E_Q \sim 2.9$ mm/s. These values are typical of nonheme high-spin (NHHS) Fe^{II} species. Similar doublets have been observed in spectra of Atm1- and Yah1-depleted mitochondria.[80,83] Although this doublet corresponded to only 2% of the total spectral intensity, it represented a substantial Fe concentration (~ 70 μM) within Δ*mtm1* mitochondria.

The dominating nanoparticle doublet prevented us from determining whether the CD is included in the spectrum of Figure V-1B. Since Fe^{III} nanoparticles in other yeast strains are reducible by sodium dithionite,[80,83] we treated Δ*mtm1* mitochondria with the detergent deoxycholate followed by dithionite. The resulting Mössbauer spectrum

(Figure V-1C) was dominated by a NHHS Fe^{II} doublet ($\delta \approx 1.3$ mm/s, $\Delta E_Q \approx 3.4$ mm/s $\Gamma \approx 0.5$ mm/s) that represented ~ 95% of spectral intensity. The remaining ~ 5% intensity had the parameters of the CD. Some or all of the species affording the HS Fe^{II} doublet may have leached out of mitochondria and chelated by the EGTA in the buffer. We estimate that all but a few % of nanoparticle Fe^{III} ions were reduced in the process. The concentration of the CD in dithionite-reduced Δ*mtm1* mitochondria (simulated by the dashed line in Figure V-1C) corresponded to ~ 160 μM Fe, *ca*. 3-times lower than that in WT mitochondria (~530 μM). We conclude that *Δmtm1 mitochondria contain ISCs and LS hemes that are collectively ata lower concentration than in WT mitochondria*.

Δ*mtm1* mitochondria exhibited a broad EPR signal near g ~ 2that displayed inverse Curie-Law behavior; i.e. under non-saturating conditions, the signal intensity increased as the temperature increased (Figure V-2, left, top panel, compare A to B). Such behavior reflects superparamagnetism, adding further evidence for the presence of nanoparticles in Δ*mtm1* mitochondria.

The low-field EPR region (Figure V-2, left, bottom panel) exhibited a signal at $g = 4.3$ that arises from mononuclear HS Fe^{III} species with rhombic symmetry. The spin intensities associated with this signal were almost identical in WT and Δ*mtm1* mitochondria, corresponding to concentrations of 1.5 ~ 2.0 μM (Table V-3). The HS Fe^{III} heme signals, with effective g-values of 6.4, 5.3 and 6.0, were more intense in the Δ*mtm1* mitochondrial spectrum than in the WT spectrum, suggesting a more oxidizing environment in Δ*mtm1* mitochondria. The high-field region of both spectra included $g_{av} = 1.94$ and 1.90 signals. These signals have been assigned to S = ½ $[Fe_2S_2]^{1+}$ clusters

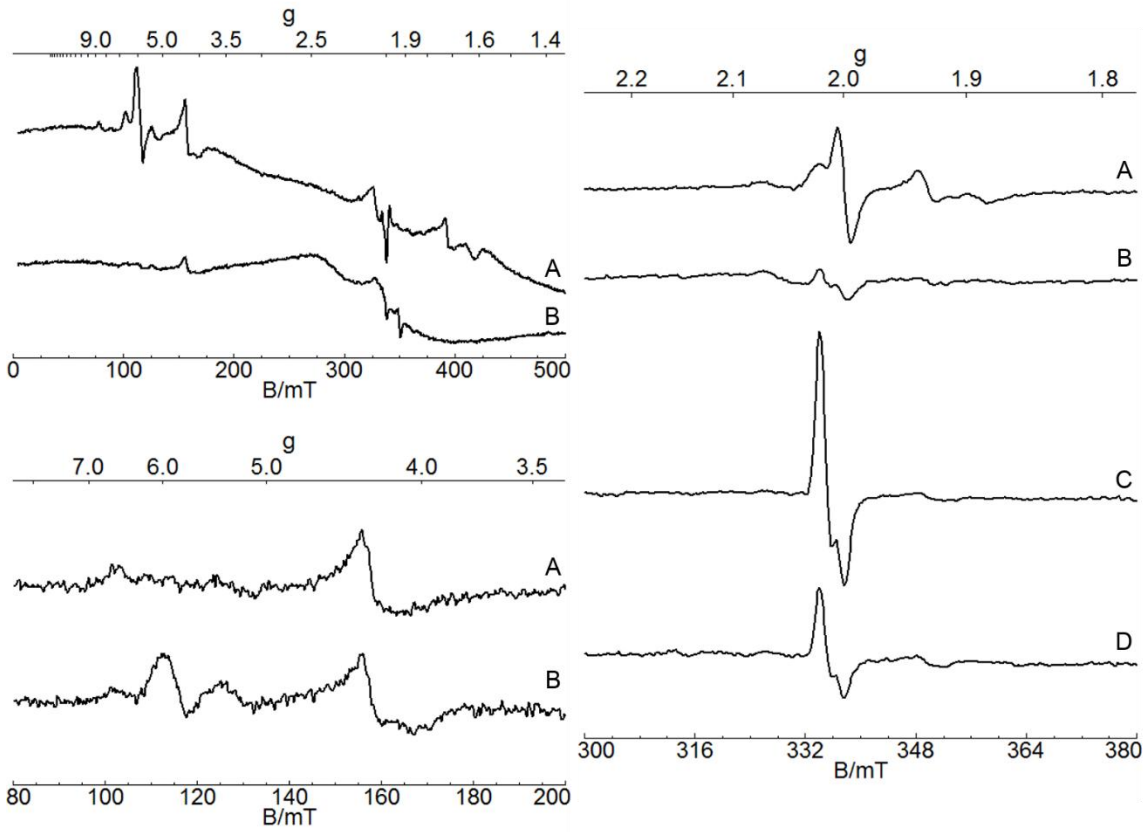

Figure V-2. X-band EPR spectra of isolated packed mitochondria from WT and Δ*mtm1* cells. Left, top panel: A, Δ*mtm1*/O_2 at 10 K; B, same as A, but at 80 K. Microwave power was 20 mW. Left, bottom panel (low-field region): A, W303/O_2; B, Δ*mtm1*/O_2. Temperature and microwave power were 10 K and 0.2 mW, respectively. Right panel (g = 2 region): A, W303/O_2; B, Δ*mtm1*/O_2; C, W303/Ar; D, Δ*mtm1*/Ar. Temperature and power were 10 K and 0.2 mW. Microwave frequency of all spectra was 9.46 GHz.

from Rieske proteins and SDH.[124] They were 3.5-times less intense in Δ*mtm1* than in WT mitochondria (Figure V-2, right panel, compare B to A), consistent with some loss of ISCs in the mutant strain.

The presence of HS and LS Fe^{II} hemes in WT and Δ*mtm1* mitochondria were assessed from UV-vis features in the 500-620 nm region. Under aerobic conditions,

Table V-3. Spin quantification of EPR spectra of W303 and Δ*mtm1* mitochondria. [a] Not determined.

Spectrum	Succinate dehydro-genase g = 2.02, 1.93, 1.91	Rieske protein g = 2.02, 1.89, 1.75	Radical g = 2.00	Aconitase $[Fe_3S_4]^+$ g = 2.02, 2.01, 2.00	Non-heme HS Fe^{III} g = 4.3	HS heme Fe^{III} g = 6.4,5.3, 6.0
W303/O_2	0.9 μM	4.2 μM	0.2 μM	N/D[a]	1.5 μM	< 0.5 μM
Δ*mtm1*/O_2	0.2 μM	1.3 μM	N/D	N/D	2.0 μM	0.9 μM
W303/Ar	0.3 μM	0.3 μM	N/D	0.5 μM	1.9 μM	N/D
Δ*mtm1*/Ar	0.3 μM	0.2 μM	N/D	0.2 μM	13.2 μM	N/D

heme concentrations in Δ*mtm1* mitochondria were 6-fold less than in WT mitochondria (Figure V-3, compare B to A). Mitochondria isolated from Δ*mtm1* cells also had 5-times more oxidative damage relative to WT cells grown under the same conditions, as assessed using the Oxyblot method (Figure V-4A).

Effect of anaerobicity

WT and Δ*mtm1* mitochondria isolated from cells grown under anaerobic conditions will be called WT/Ar and Δ*mtm1*/Ar mitochondria, respectively. The Fe concentrations of these samples were substantially lower than in mitochondria from cells grown aerobically (Table V-1). The intensity of the 5 K, 0.05 T Mössbauer spectrum of Δ*mtm1*/Ar mitochondria was also low (Figure V-1E), consistent with the lower Fe concentration of the sample. Two major features were discerned, including the CD and a NHHS Fe^{II} doublet ($\delta \approx 1.2$ mm/s, $\Delta E_Q \approx 2.7$ mm/s). A significant proportion of Fe

could not be assigned due to the low S/N. However, the lack of a major nanoparticle doublet indicated that the O_2 used in cell growth is required for the formation of these nanoparticles, similar to the situation for Atm1 and Yah1 strains.[80,83] The absolute concentration of CD-associated Fe in mitochondria obtained from cells grown under anaerobic conditions was ~ 200 μM, about half of that present under aerobic conditions and consistent with the lower Fe concentration in the samples.

The high-energy line of the NHHS Fe^{II} doublet in spectra of anaerobically grown Δ*mtm1* mitochondria (~2.5 mm/s) was shifted slightly (by *ca*. 0.4 mm/s) towards lower energy relative to the analogous line in aerobically-grown Δ*mtm1* mitochondria (2.9 ~ 3.0 mm/s). Comparing the spectra from anaerobic *vs*. aerobic WT mitochondria suggested a similar shift (Figure V-5). These results indicate different populations of HS Fe^{II} species depending on the aerobicity of the yeast culture. However, the spectra were noisy, so further studies will be required to confirm this. In contrast, there were no distinguishing differences between the NHHS Fe^{II} species in WT vs. Δ*mtm1* mitochondria, at least to the extent discernible by Mössbauer spectroscopy.

Both WT/Ar and Δ*mtm1*/Ar mitochondria contained hemes at approximately equal concentrations (Figure V-3, C and D), but these concentrations were substantially less than were present in WT mitochondria isolated under aerobic conditions (Figure V-3A). Interestingly, the concentration of O_2 required for aerobic-levels of heme synthesis appears to be quite low. Just prior to harvesting, one batch of Δ*mtm1*/Ar cells were (inadvertently) exposed to a micro-aerobic environment by being stirred for 2 hrs in the sealed bioreactor but not purged with Ar. The heme *b* and *c* concentrations in

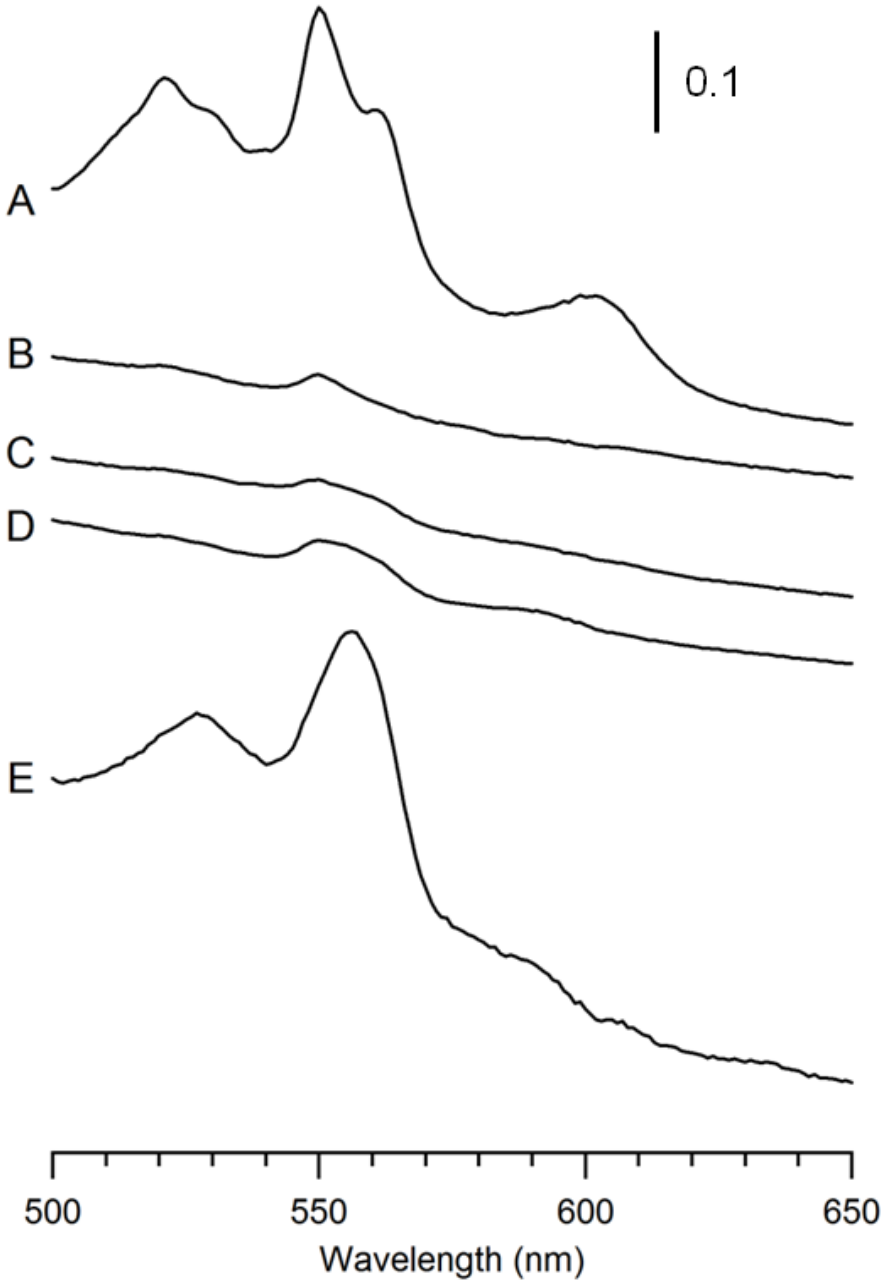

Figure V-3. Electronic absorption spectra of mitochondrial suspensions from WT and Δ*mtm1* cells. A, W303/O_2; B, Δ*mtm1*/O_2; C, W303/Ar; D, Δ*mtm1*/Ar; E, Δ*mtm1*/Ar mitochondria isolated from Δ*mtm1*/Ar cells that had been exposed to microaerobic environment before harvesting. Indicated absorbance change corresponds to that expected had spectra been collected in a 1 cm pathlength cuvette.

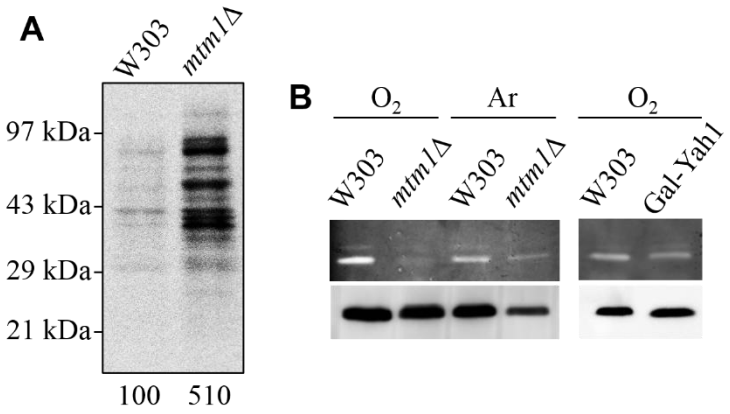

Figure V-4. OxyBlot analysis, SOD activity assays and Western blotting against Sod2p. A, OxyBlot of mitochondria isolated from aerobically grown W303 and Δ*mtm1* cells; B, SOD activity assays and Western blotting against Sod2p for whole cell lysates from aerobically (O_2) and anaerobically (Ar) grown W303, Δ*mtm1* and Gal-Yah1 cells. All cells were grown on glucose.

mitochondria isolated from those cells (Figure V-3E) were almost at WT levels while heme *a* was largely absent. Thus Δ*mtm1* cells are capable of synthesizing WT levels of heme *b* and *c* centers with minimal O_2 exposure. This strongly suggests that the low level of hemes in mitochondria isolated from Δ*mtm1* cells grown under aerobic conditions is not due to the absence of Mtm1p as has been suggested[80,83] and may be due to ROS-promoted damage of such centers. Δ*mtm1* cells can synthesize such prosthetic groups if O_2 and ROS levels are modest.

EPR spectra from mitochondria isolated from both WT/Ar and Δ*mtm1*/Ar cells exhibited g_{ave} = 1.94 and 1.90 signals of approximately equal low intensities (Figure V-2, C and D), suggesting that cells lacking *MTM1* are capable of synthesizing ISCs under anaerobic conditions (Table V-3). Interestingly, mitochondria from both WT and Δ*mtm1*

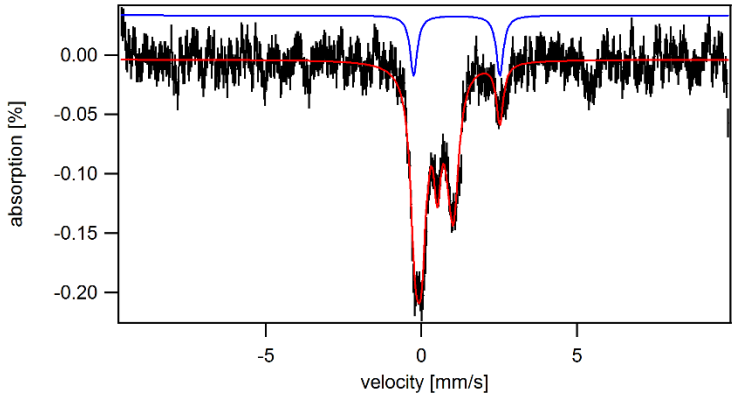

Figure V-5. 5 K, 0.05 T Mössbauer spectrum of mitochondria isolated from anaerobically grown WT cells. The red line is a simulation, assuming terms and parameters given in Table S1. The blue line is a simulation of the NHHS Fe^{II} component.

cells exhibited significant levels (quantifying to 0.2 ~ 0.5 μM) of a g_{ave} = 2.01 signal (g = 2.03, 2.02, 2.00) typical of S = ½ $[Fe_3S_4]^+$ clusters like that found in inactive aconitase. Such signals are generally not found in spectra of mitochondria from aerobically grown cells. Confounding this analysis were significant aconitase activities in WT/Ar and Δ*mtm1*/Ar mitochondria (Table V-1).

Enzyme activities

Activities of other selected ISC-containing enzymes were also determined to further evaluate the Δ*mtm1* phenotype. For cells grown under aerobic conditions, aconitase activity was substantially reduced in Δ*mtm1* mitochondria relative to WT mitochondria (Table V-1). SDH activity in Δ*mtm1* mitochondria was about 10-fold lower than in WT mitochondria; however under anaerobic conditions, SDH activity was

near WT/Ar levels. These results collectively indicate that *deleting MTM1induces oxidative stress in the presence of O_2 that damages hemes and ISCs*.

Leu1p is an ISC-containing enzyme found in the cytosol; its activity is commonly used to monitor the activity of the cytosolic ISC assembly machine known as the CIA.[52] In Δ*mtm1* cells, the activity of Leu1p was ~ 60% of that in WT cells under aerobic growth conditions and < 50% of that in WT cells under anaerobic conditions. This is a different pattern than was observed for the other measured activities, which were reduced under aerobic conditions and near-WT levels under anaerobic conditions. This difference suggests that ROS is *not* responsible for the absence of Leu1 activity in Δ*mtm1* cells. One possibility is that Mtm1p, like another mitochondrial transporter Atm1p, is required for the CIA to function. Alternatively, the expression-level of Leu1 may be reduced in Δ*mtm1* cells *vs*. in WT cells. We are unable to distinguish these possibilities.

SOD2 activity

We measured SOD2 activities and Sod2p protein levels in electrophoretic gel bands. The SOD2 activity of fermenting Δ*mtm1* cell extracts was 26 ± 6% (avg. of 3 trials) of the WT level (Figure V-4B, left panel), whereas the Sod2p protein level in Δ*mtm1* cell extracts was 71 ± 12% of WT (Table V-1). Thus, the average SOD2 specific activity of Δ*mtm1* cell extracts was 42 ± 16% of the WT value. This percentage-decline is similar to data reported for SOD2 specific activities in Δ*mtm1* vs. WT cells.[54] We also examined SOD2 activities in cells grown under anaerobic conditions. Relative to

aerobically grown WT cells, WT/Ar and Δ*mtm1*/Ar cells respectively exhibited 66 ± 7% and 14 ± 3% of SOD2 activity (Figure V-4B, left panel, compare lanes 3 and 4 to lane 1). Sod2p protein expression level in WT/Ar and Δ*mtm1*/Ar cells were 77 ± 19% and 36 ± 5% relative to aerobically grown WT cells. This indicates SOD2 specific activities of 102 ± 34% and 42 ± 12% for WT/Ar and Δ*mtm1*/Ar cells, respectively, relative to the aerobic case. Thus, SOD2 specific activities of Δ*mtm1* cells were about 40% of WT levels, *regardless of whether cells were grown aerobically or anaerobically*. For comparison, the SOD2 activity of Yah1-depleted cells was also examined; these cells exhibited 87 ± 11% of the SOD2 specific activity, relative to aerobically grown WT cells (Figure V-4B, right panel, lane 2 *vs*. 1).

These results indicate that SOD2 inactivation in Δ*mtm1* cells is *not* associated with ROS damage, in contrast to the loss of hemes and ISCs which are ROS-associated. We conclude that a deficiency of Mtm1p is more closely associated with the inactivation of Sod2p or perhaps with the functioning of the cytosolic ISC assembly (CIA) machine than with the accumulation of nanoparticles, the loss of mitochondrial ISC and heme centers, or the generation of ROS.

Whole cells

WT and Δ*mtm1* whole yeast cells were analyzed by Mössbauer spectroscopy and ICP-MS (Tables V-1 and V-2). The dominant feature (Figure V-6A) was a sextet due to a HS Fe^{III} species that resides in vacuoles.[46] Also evident were the CD, a HS heme Fe^{II}

doublet and perhaps a NHHS Fe^{II} doublet ($\delta \approx 1.3$ mm/s, $\Delta E_Q \approx 3.1$ mm/s). The latter feature was barely discernible; it corresponded to only *ca*. 13 μM Fe (2% of 640 μM).

The spectrum of equivalently grown Δ*mtm1* cells (Figure V-6B) was dominated by the Fe^{III} nanoparticle doublet ($\delta \approx 0.53$, $\Delta E_Q \approx 0.58$), but it also contained a sextet arising from vacuolar mononuclear HS Fe^{III} species and a more predominant NHHS Fe^{II} doublet ($\delta \approx 1.4$, $\Delta E_Q \approx 3.0$; simulated by the blue solid line). The intensity of NHHS Fe^{II} species in Δ*mtm1* cells was also significant, corresponding to *ca*. 540 μM (11% of 4900 μM), ~ 40-fold higher than in WT cells. Although the percentage of spectral intensity due to the sextet was small, the absolute concentration of the NHHS Fe^{III} species in Δ*mtm1* cells was actually similar to that in WT cells. The same pattern was observed using Aft1-1^{up} cells,[81] where vacuolar HS Fe^{III} was present along with a dominating nanoparticle species. The pattern was different with Yah1- and Atm1-deficient cells, where only the nanoparticle doublet was present (i.e. vacuolar mononuclear Fe^{III} was absent).[80,81] The reason for this difference is unknown, but vacuoles in Yah1- and Atm1-deficient cells (but not in Aft1-1^{up} or Δ*mtm1* cells) appear devoid of mononuclear HS Fe^{III}.

Mössbauer spectra of WT/Ar and Δ*mtm1*/Ar cells (Figure V-6, C and D) were similar to each other and to spectra of aerobically grown WT cells in that few nanoparticles were present. This indicates that O_2 exposure was required for nanoparticle formation in Δ*mtm1* cells. The spectra of WT/Ar and Δ*mtm1*/Ar cells were different relative to that of WT/O_2 cells, in that the percentage of Fe due to the CD was diminished and the percentage of Fe due to NHHS Fe^{II} species was enlarged. The

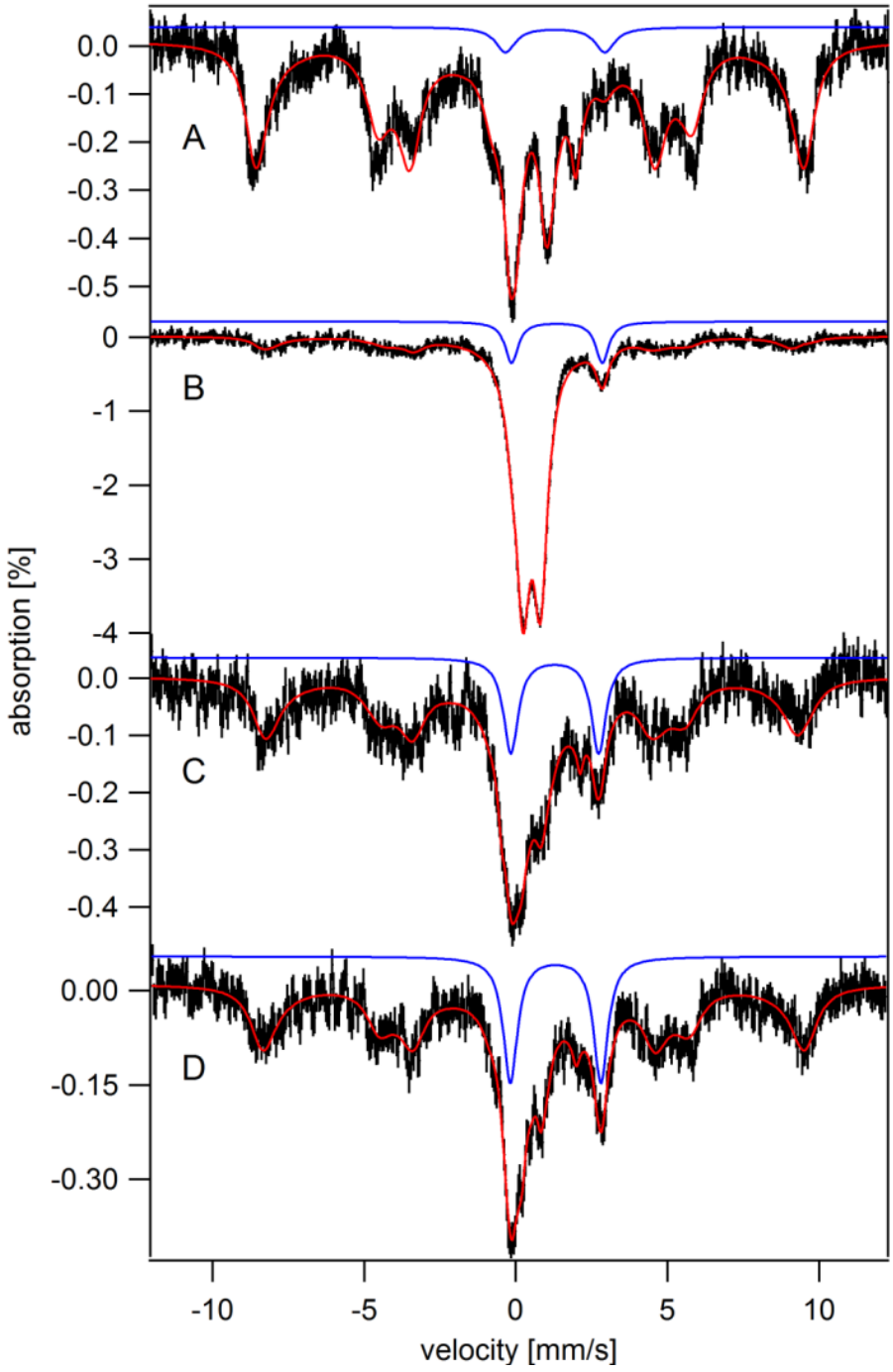

Figure V-6. 5 K, 0.05 T Mössbauer spectra of W303 and Δ*mtm1* cells grown under aerobic and anaerobic conditions. A, WT/O_2; B, Δ*mtm1*/O_2; C, WT/Ar; D, Δ*mtm1*/Ar. Red solid lines are simulations based on percentages in Table S1. Blue solid lines simulate the contribution of NHHS Fe^{II} species in the samples.

reduced CD intensity suggests diminished mitochondrial respiratory complexes under anaerobic conditions. Interpreting the increase of NHHS Fe^{II} species in anaerobically grown cells is difficult because the location and function of these species are uncertain.

Regardless of the origin of this type of Fe, Δ*mtm1* cells accumulated somewhat more HS Fe^{II} than WT cells under both aerobic and anaerobic growth conditions. We considered that this might represent the Fe_{ASR} pool, but the sought-after Fe must be located in the mitochondria since it would incorporate into apo-Sod2p when this protein folds in the matrix. Δ*mtm1* mitochondria do not contain substantial HS Fe^{II} species relative to the level in WT mitochondria.

Effects of deleting MTM1 on mitochondrial manganese

Mn concentrations in mitochondria isolated from Δ*mtm1* cells grown under both aerobic and anaerobic conditions were two-fold higher than in equivalent WT mitochondria (Table V-1). In contrast, Δ*mtm1* whole cells contained about the same concentration of Mn as WT cells, again independent of aerobicity. Taken together, *these results indicate that Δmtm1 mitochondria accumulate cellular Mn.* Whether there was a corresponding decrease in the Mn concentration of the non-mitochondrial portions of the cell could not be determined from these data. An absolute increase of *ca*. 10 μM Mn in Δ*mtm1* mitochondria would have caused only an increase of *ca*. 1 μM in the overall Mn concentration in the cell (the mitochondria occupy *ca*. 10% of the cell volume). Since this Mn concentration increase also occurred under anaerobic conditions, it does not appear to be connected to the accumulation of nanoparticles in Δ*mtm1* mitochondria.

These results raise the possibility that Mtm1p *exports* Mn^{II} ions from the mitochondrial matrix to the cytosol.

Soluble mitochondrial extracts

In 3 independent experiments, WT and Δ*mtm1* mitochondrial fractions were sonicated, spun by centrifugation, and soluble fractions were collected. In the first experiment, the pellet was resuspended and re-sonicated, and the second soluble fraction was combined with the first. In the second experiment, the pellet of the first spin was discarded. In the third experiment the pellet from the first spin was also discarded, but more importantly, the cells were grown in medium containing 200 μM $MnCl_2$.

This procedure solubilized an average of 35% ± 12% (n = 6) of the Mn in WT and Δ*mtm1* mitochondria, with no strain dependence (Table V-4). These soluble fractions contained 25% ± 13% of the protein and 25% ± 12% of the SOD2 activity in the original samples. This procedure also solubilized 21% ± 6% of the Fe in WT mitochondria, whereas only 7% ± 1% of Fe in Δ*mtm1* cells were solubilized. This difference reflects the greater proportion of nanoparticles in Δ*mtm1* mitochondria. Because ofthis low recovery, the contents of the soluble fractions may not faithfully indicate the content of the soluble portions of intact mitochondria.

Table V-4. Preparation of soluble mitochondrial fractions for LC-ICP-MS analysis. Percentages of metal, protein, and SOD2 activity in soluble mitochondrial fractions were measured relative to total mitochondrial contents.

Sample	Mn	Fe	Protein	SOD2 activity
W303-1 1st SEC Figure S2a	44%	24%	39%	23%
W303-2 2nd SEC Figure 6a	32%	25%	18%	32%
W303-3 3rd SEC (200 μM Mn) Figure S3a	15%	14%	7%	10%
W303-4 LMM (detergent-treated, passed 10 kDa cut-off) Figure 6c	17%	16%	-	-
W303-5 1st MonoQ Figure 7	19%	11%	30%	56%
W303-6 2nd MonoQ Figure 8a	26%	13%	29%	49%
Δ*mtm1*-1 1st SEC Figure S2b	48%	7%	39%	11%
Δ*mtm1*-2 2nd SEC Figure 6b	42%	7%	30%	41%
Δ*mtm1*-3 3rd SEC (200 μM Mn) Figure S3b	28%	8%	15%	31%

Table V-4. Continued

Sample	Mn	Fe	Protein	SOD2 activity
Δ*mtm1*-4 LMM (detergent-treated, passed 10 kDa cut-off) Figure 6c	16%	3%	-	-
Δ*mtm1*-5 1st MonoQ Figure 7	29%	20%	34%	43%
Δ*mtm1*-3 2nd MonoQ Figure 8b	38%	8%	40%	24%

LC-ICP-MS experiments

Soluble WT and Δ*mtm1* fractions were subjected to liquid chromatography, and the eluent was monitored for metal ions using ICP-MS. In most experiments, the ICP-MS was configured *on-line*, such that the eluent was split, with a portion flowing into fractions and the remainder to the ICP-MS in real time during the chromatography run. In off-line experiments, the entire eluent was fractionated and subsequently sampled by ICP-MS.

Since a greater proportion of SOD2 activity was in the soluble fraction of Experiment 2, we describe that experiment now (and include the results of Experiment 1 in Figure V-7). The A_{280} trace of the eluent off the Superdex column (not shown) indicated that > 90% of the protein in the soluble samples eluted in the void volume. This volume was *ca*. 46 mL and corresponded to molecular masses > 600 kDa. Also eluting in the void volume was a small proportion of the Mn in the injected sample

(Figure V-8, *a* and *b*). Two major Mn peaks were observed in later fractions, called Mn_{100} and $Mn_{2\text{-}3}$, with molecular masses of *ca*. 100 kDa and < 10 kDa respectively (Figure V-8, *a* and *b,* and Table V-5). Mn_{100} co-eluted with active tetrameric Sod2p while $Mn_{2\text{-}3}$ corresponded to the LMM species.

We have sufficient information to roughly estimate the speciation of Mn in mitochondria. In WT mitos grown on normal medium, *ca*. 64% of the soluble Mn was SOD2-associated. Thus, ~ 24% (0.64×38%) of total Mn ions in the original mitochondrial sample was associated with 27% of SOD2 activity. The similarity of these two numbers suggests that the remaining 73% of MnSod2p in the pellet represented another 65% of the Mn in WT mitochondria. Thus, the majority of the Mn in these organelles (27% + 65% = 92%) is associated with MnSod2p. $Mn_{2\text{-}3}$ represented 32 ± 3% of the soluble Mn in our WT samples, corresponding to 12% (0.32×38%) of total WT mitochondrial Mn. These results indicate that *the Mn in WT mitochondria is distributed into two species – ca. 90% is associated with MnSod2p and ca. 10% is present as soluble LMM species.*

In Δ*mtm1* mitochondria, about 46% of total Mn was soluble. Of this, 89% was LMM and 9% was associated with MnSod2p. Only *ca*. 4% of total Mn in Δ*mtm1* mitochondria was in the form of soluble Sod2p, and this corresponded to 25% of total SOD2 activity. The other 75% of the Sod2p protein (in the pellet) must have included another 12% of the total Mn. Thus, 16% of total Mn in Δ*mtm1* mitochondria (4% + 12%) was probably MnSod2p-associated. The only other species observed in the soluble fraction was $Mn_{2\text{-}3}$, suggesting that > 80% of the Mn in Δ*mtm1* mitochondria arise from

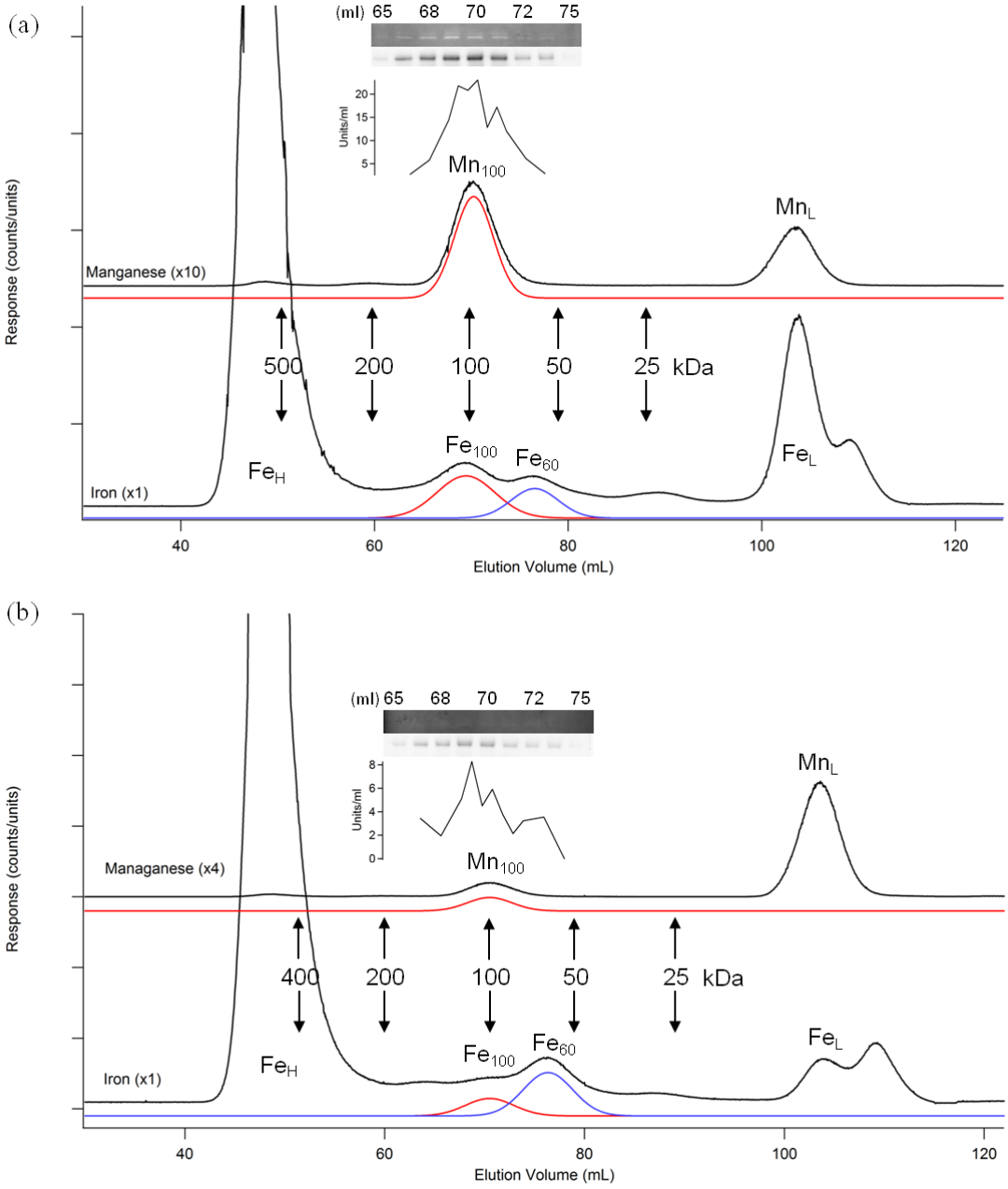

Figure V-7. Mn and Fe traces from Experiment 1 of the first group of LC-ICP-MS studies. The inset shows SOD2 activity gels, Western blots against Sod2p, and SOD2 unit activities. (a) W303; (b) Δ*mtm1*.

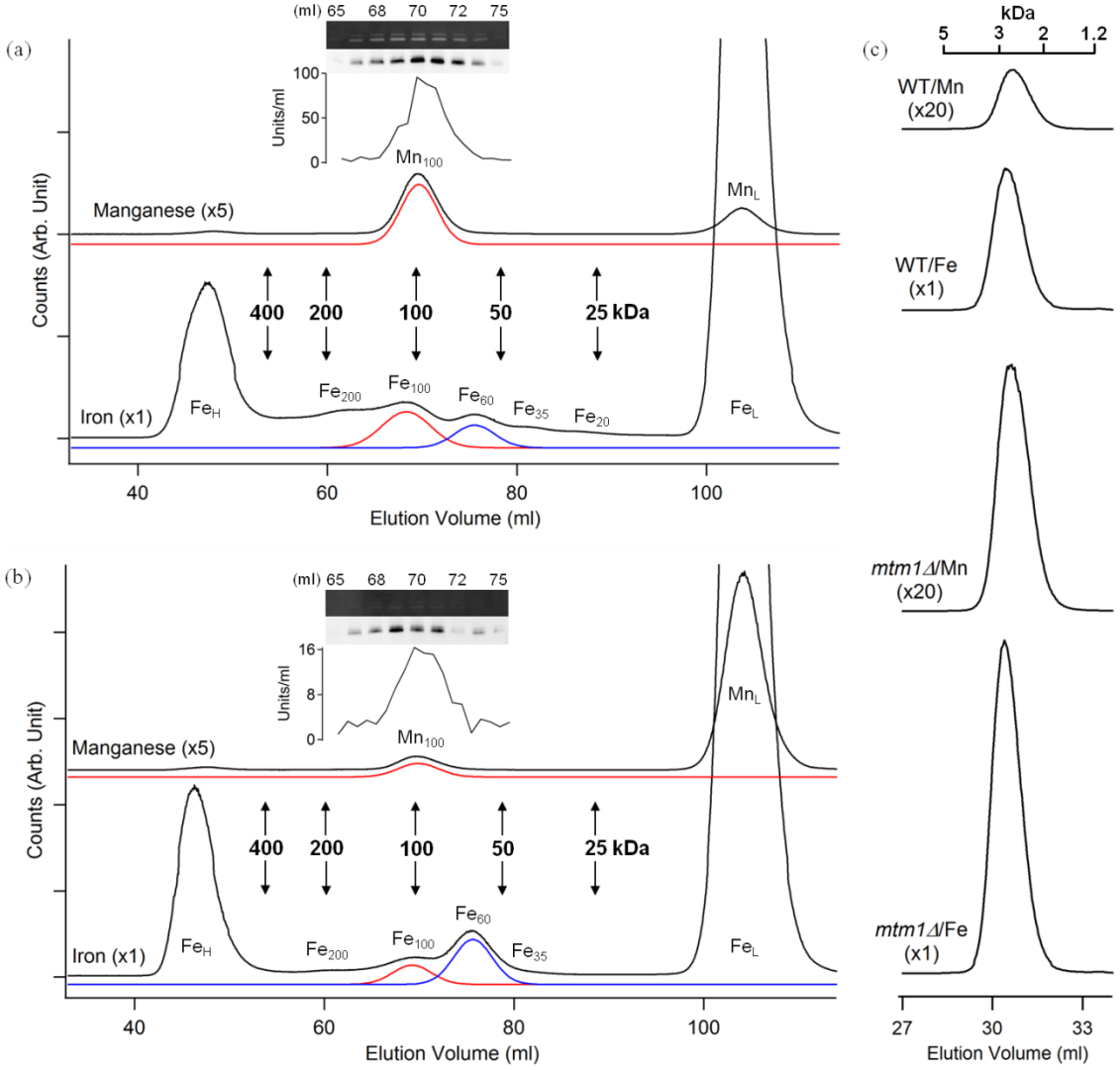

Figure V-8. Mn and Fe traces from SEC-ICP-MS chromatography of soluble fractions of W303 and Δ*mtm1* mitochondria. (a) HMM chromatograms of W303 mitochondria; (b) HMM chromatograms of Δ*mtm1* mitochondria, Experiment 2. Red solid lines simulate Mn and Fe species co-eluted with Sod2p (Table S4). Blue solid lines simulate Fe_{ASR} candidate species. The inset shows images of SOD2 activity gel, Western blot membrane against Sod2p for each fraction labeled with fraction volume, and SOD2 unit activities determined spectrophotometrically. Metal peaks were labeled according to their approximate molecular weight. Molecular weight was determined by using calibration plot for Hi-Load Superdex 200 column. (c) LMM chromatograms of W303 and Δ*mtm1* mitochondria, Experiment 4. Chromatographic intensities were adjusted proportionally to mitochondrial LMW Mn and Fe concentrations, and then WT-Mn and Δ*mtm1*-Mn were amplified 20-fold for easier comparison. Molecular weight was determined by using calibration plot for Superdex Peptide 16 × 300 mm column.

LMM species. As mentioned above, the concentration of Mn in Δ*mtm1* mitochondria was about *twice* that of WT mitochondria. Our analysis indicates that most of the additional Mn in Δ*mtm1* mitochondria was present as $Mn_{2\text{-}3}$. Also, the MnSod2p protein level in Δ*mtm1* mitochondria was diminished relative to WT levels. Assuming 13 μM [Mn] in WT mitochondria, this corresponds to 12 μM MnSod2p and 1 μM $Mn_{2\text{-}3}$. In Δ*mtm1* mitochondria, with 26 μM [Mn], we calculate 4 μM MnSod2p and 22 μM $Mn_{2\text{-}3}$. Thus, *deleting MTM1 caused a 3-fold reduction in active MnSod2p and a 22-fold increase in the size of the LMM Mn pool in the mitochondria*. In the third experiment, for mitochondria isolated from WT cells grown on medium supplemented with 200 μM $MnCl_2$, the Mn trace (Figure V-9a) again showed two major peaks, Mn_{100} (23%) and $Mn_{2\text{-}3}$ (68%). In this case, 15% of the total Mn in the sample was soluble, and of this, 23% corresponded to MnSod2p. This means that 0.23×15% = 3.5% of total Mn in the sample corresponded to 10% of the SOD2 activity. The remaining 90% of the activity must have represented another 31% of total Mn. Thus, nearly 35% (3.5% + 31%) of total Mn in the sample was associated with MnSod2p. The only other species present in the chromatogram was $Mn_{2\text{-}3}$, suggesting that it corresponded to the remaining 65% of the total Mn in WT mitochondria grown on excess Mn. With 35 μM = [Mn], we conclude that 12 μM was MnSod2p and 23 μM was $Mn_{2\text{-}3}$. Thus, the MnSod2p level remained about the same while the LMM Mn pool increased dramatically. Thus, the size of the LMM Mn pool in mitochondria is sensitive to the Mn concentration in the medium.

Finally, we consider the Mn distribution in mitochondria from Δ*mtm1* cells grown on 200 μM Mn (Figure V-9b). In this case, Mn_{100} represented 5% of the Mn in

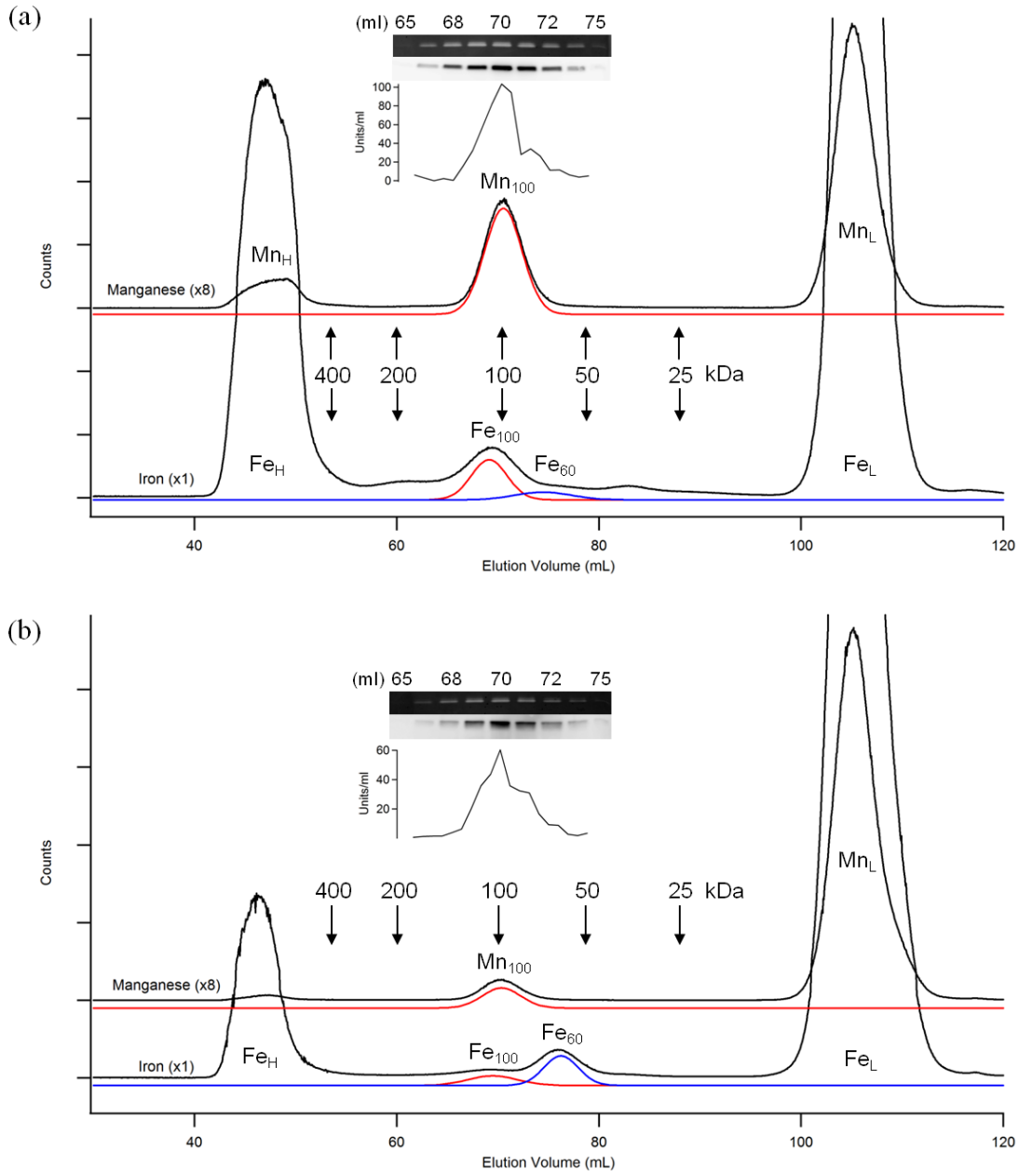

Figure V-9. Mn and Fe traces from Experiment 3 of the first group of LC-ICP-MS studies. The inset shows SOD2 activity gels, Western blots against Sod2p, and SOD2 unit activities determined spectrophotometrically. (a) W303; (b) Δ*mtm1*.

Table V-5. Peak analysis of HMM chromatograms. Percentage of each peak was calculated by fitting chromatograms. The numbers after the semicolon refer to the experiment in which cell were grown in 200 μM Mn in the medium.

Peak	Approximate Molecular mass (kDa)	% of Chromatogram intensity	
		W303	Δ*mtm1*
Mn_H	> 600	3 ; 9	2 ; 1
Mn_{200}	200	1 ; 0	0.4 ; 0
Mn_{100}	100	64 ; 23	9 ; 5
$Mn_{2\text{-}3}$	< 6 (2-3 using LMM column)	32 ; 68	89 ; 94
Fe_H	>600	(67,17) ; 32	(79,15) ; 12
Fe_{200}	200	3 ; 2	2 ; 0
Fe_{100}	100	4 ; 3	2 ; 0.4
Fe_{60}	60	2 ; 1	4 ; 2
Fe_{35}	35	0 ; 1	0.2 ; 0.3
Fe_{20}	20	1 ; 0	1 ; 0
$Fe_{2\text{-}3}$	< 6 (2-3 using LMM column)	(19,74) ; 62	(8,79) ; 84

the chromatogram while $Mn_{2\text{-}3}$ was 94%. 39% of total Mn was soluble, and so (0.05×39% =) 2% of total Mn corresponded to 31% of MnSOD2 activity. The remaining 69% of the SOD activity must correspond to another 4.4% of the total Mn in the sample,suggesting that 6.4% of total Mn was MnSod2p. The sample had 80 μM Mn, and so there was 5 μM (80×0.064) MnSod2p in mitochondria from Δ*mtm1* cells grown with 200 μM Mn. The remaining 75 μM was associated with $Mn_{2\text{-}3}$. This analysis indicates that the concentration of MnSod2p did not change with Mn supplementation in the growth medium, but that the LMM Mn pool concentration increased more than 2-fold. The results of these calculations are visually summarized in Figure V-10.

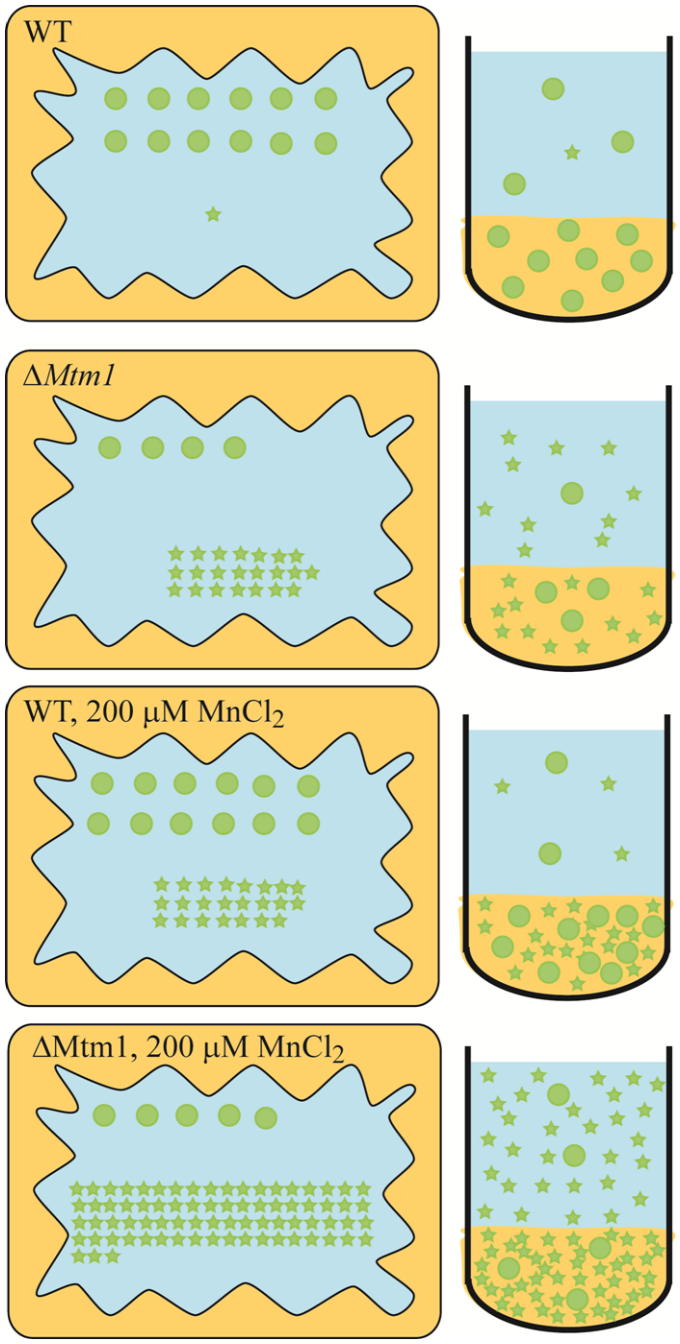

Figure V-10. Manganese distribution in mitochondria. Left side, concentrations of MnSod2p (circles) and $Mn_{2\text{-}3}$ (stars) in intact mitochondria from WT and Δ*mtm1* cells grown on media with ~ 2 and 200 μM Mn. Right side, the Mn content of corresponding mitochondrial extracts after sonication and centrifugation. Each circle and star represents 1 μM Mn concentration.

The corresponding Fe traces exhibited 7 distinguishable features, with significant concentrations in the void volume (Fe_H), 5 minor-intensity peaks in the central region (Figure V-8, *a* and *b*; F_{200}, Fe_{100} , Fe_{60}, Fe_{35}, and Fe_{20}), and an intense LMM feature (Fe_3) that has a slightly higher mass than $Mn_{2\text{-}3}$. Fe_3 is a viable candidate for Fe_{ASR}. For the first two experiments, an average of 25% of the total Fe was solubilized from mitochondrial extracts. Of this, Fe_H represented 67% of total mitochondrial Fe in one experiment and 17% in the other. The Fe_3 intensity corresponded to 19% of total Fe in the first experiment and 74% in the second. Despite the large variations, these two peaks collectively dominated the Fe chromatograms of soluble WT mitochondrial extracts. The intermediate-molecular-mass (IMM) Fe species corresponded to *ca*. 10% of the soluble Fe – representing 2.5% of the total Fe. With a total Fe concentration of 880 μM in WT mitochondria, these IMM Fe species were present at *ca*. 20 μM collectively, with Fe_{100} corresponding to a concentration of *ca*. 9 μM.

An average of 7% of total Fe was solubilized in the corresponding Δ*mtm1* mitochondria samples. Since the Fe concentration in these mitochondria was 3500 μM, this corresponded to 245 μM Fe injected onto the column. Fe_H and Fe_3 again dominated the chromatograms. Fe_{100} represented 2% of the overall chromatogram intensity, corresponding to a concentration of 5 μM. Thus, upon deleting *mtm1*, Fe_{100} declined nearly 2-fold.

Under high Mn nutrient conditions, 14% of WT mitochondrial Fe was solubilized; this corresponded to 87 μM Fe (620 μM×0.14) in the soluble sample. Fe_{100} represented 3% of that Fe (*ca*. 3 μM). For Δ*mtm1* mitochondria, 8% of mitochondrial Fe

was solubilized. At 5200 μM Fe, this corresponded to 416 μM soluble Fe loaded on the column. Fe_{100} represented 0.4%, corresponding to 2 μM. Thus, deleting *MTM1* under high Mn caused a slight decline of Fe_{100}. This was the same qualitative effect as seen under normal Mn growth conditions.

Fe_{100} approximately coeluted with Mn_{100} raising the possibility that it corresponded to FeSod2p. The absolute concentration of Fe_{100} in mitochondria and the percentage of Fe that it represented would indeed make it impossible to detect by either Mössbauer or XAS spectroscopies. If the percentage of Fe-misincorporated Sod2p is defined as = $100 \cdot [Fe_{100}]/([Fe_{100}]+[Mn_{100}])$, then the percentage of FeSod2p was 75 ± 4% and 79 ± 3% for WT and Δ*mtm1* mitochondria (ave. of 3 experiments). Assuming that Fe_{100} corresponds to FeSod2p, these percentages show that *there was no significant difference in the extent of Fe misincorporation into apo-Sod2p between WT and Δmtm1 mitochondria*. Although these results cannot exclude the possibility that Fe_{100} corresponds to FeSod2p, the results of other LC experiments (e.g. *See* Figure V-13) discount this possibility. Thus, we suggest that only minor portions of Sod2p in our WT and *Δmtm1* preparations may be misincorporated with Fe.

We performed SOD2 activity gels and Western blots against Sod2p using pooled Sod2p-containing fractions and as-isolated mitochondria. In all three experiments, pooled fractions of SOD2-active Δ*mtm1* extracts revealed specific activities corresponding to 100 ± 14% of WT levels (Figure V-11, lane 4, 6, 10 vs. lane 3, 5, 9). This again indicated that the extent of Fe-misincorporation in Δmtm1 and WT cells is similar.

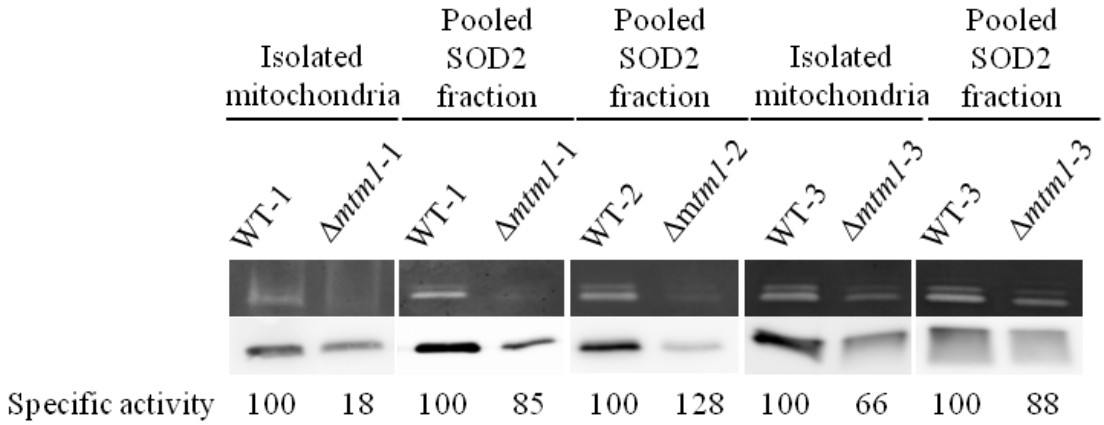

Figure V-11. SOD activity and Western blot analysis of various samples. Lanes 1 and 2, reading from left to right, isolated mitochondria from Experiments 1 of the first group of LC-ICP-MS studies, before sonication. Lanes 3 – 6, pooled Sod2p-containing fractions from the Superdex 200 column in Experiments 1 and 2 (matched with Figure S2 and 6). Lanes 7 and 8 isolated mitochondria from Experiments 3 of the first group of LC-ICP-MS studies, before sonication. Lanes 9 – 10, pooled Sod2p-containing fractions from the Superdex 200 column in Experiments 3 (matched with Figure S3). Specific activities relative to wild type were shown for each lane. Top panels with dark background are images of native PAGE gels stained for NBT SOD2 activity assay. 2 – 3 bright bands represented MnSod2p tetramers migrating with different positions. Bottom panels with white background are images of WB membranes obtained from denaturing SDS-PAGE gels. Generally a single band was observed due to MnSod2p monomer.

The situation was different using isolated mitochondria. The SOD2 specific activity of Δ*mtm1* mitochondrial extracts, prepared from cells grown without Mn supplementation, was *ca*. 20% of the SOD2 specific activity of equivalent WT mitochondrial extracts (Figure V-11, lane 2 vs. 1). *This suggested that a large percentage of Sod2p in Δmtm1 mitochondria is inactive but is not associated with the MnSod2p in the* Mn_{100}*-containing fractions.* The inactive Sod2p probably migrates differently through the column or remains in the pellet during solubilization. We

performed Western blots on various fractions that eluted from the column, but could not identify any that contained Sod2p, suggesting that the inactive form is in the pellet. This form could be Fe-misincorporated, misfolded or modified in some manner.

There was some recovery in SOD2 specific activity in mitochondria isolated from cells grown on Mn supplemented medium (Figure V-11, lane 8 vs. 2), similar to that reported previously.[53] In this case, the SOD2 specific activity of Δ*mtm1* mitochondria was *ca*. 70% relative to WT mitochondria. This might be caused, not by an increase of MnSod2p, but a decrease in Sod2p expression such that only ~ 30% of Sod2p in Δ*mtm1* mitochondria is inactive. Further studies are required to examine this possibility.

LC-ICP-MS of LMM species

We initially collected the $Mn_{2\text{-}3}$ and Fe_3 fractions from the first group of experiments, and subjected them to the LMM size-exclusion column to determine their molecular masses to greater accuracy. The results indicated multiple overlapping species, with poor reproducibility from batch to batch. More consistent (and simpler) results were obtained by disrupting isolated mitochondria by adding detergent (deoxycholate) rather than by sonication. Supernatant fractions were passed through the 10 kDa cut-off membrane and the flow-through was injected onto the column. $Mn_{2\text{-}3}$ and Fe_3 dominated (Figure V-8c, Experiment 4), and they eluted in accordance with molecular masses between 2 – 3 kDa (explaining the subscripts used). Taken together,

these results suggest that the major LMM Mn and Fe species in yeast mitochondria have similar ligand environments (at least in terms of the collective masses of the ligands).

Anion exchange chromatography

We repeated previous LC experiments[54] using the same column (Mono Q) and run conditions (except that we performed our LC under anaerobic conditions). Due to the high salt concentration involved at the end of the gradient, individual fractions were analyzed (after dilution) for metals using the ICP-MS off-line. Soluble mitochondrial extracts from sonicated WT and Δ*mtm1* mitochondria afforded an intense Mn peak at ~ 14 mL, another less intense peak (or group of incompletely resolved peaks centered) at ~ 19 mL, and unassigned peaks at 2, 36, and 62 mL (Figure V-12, Experiment 5). We tentatively assign the dominant peak to $Mn_{2\text{-}3}$, based on results of the LMM size-exclusion study in which MnSod2p and $Mn_{2\text{-}3}$ peaks dominated. SOD2 activity assays and Western blots against Sod2p demonstrated that that Sod2p co-eluted with the second peak(s) (Figure V-12, *insets i*, *ii*). The specific SOD2 activity in the five fractions containing most Sod2p was 2-fold lower in Δ*mtm1* than in WT fractions, suggesting that one or more inactive forms of Sod2p co-eluted with the active form. The Fe concentrations in these fractions were also determined. One major Fe peak was observed in both Δ*mtm1* and WT chromatograms, which we tentatively assign to Fe_3, with similar justification. There were low intensity features in the vicinity of the SOD2-active Mn peaks (Figure V-12, *insets iii*, *iv*), but nothing that comigrated exactly with the SOD2-active fractions or with an intensity that would suggest massive Fe-misincorporation.

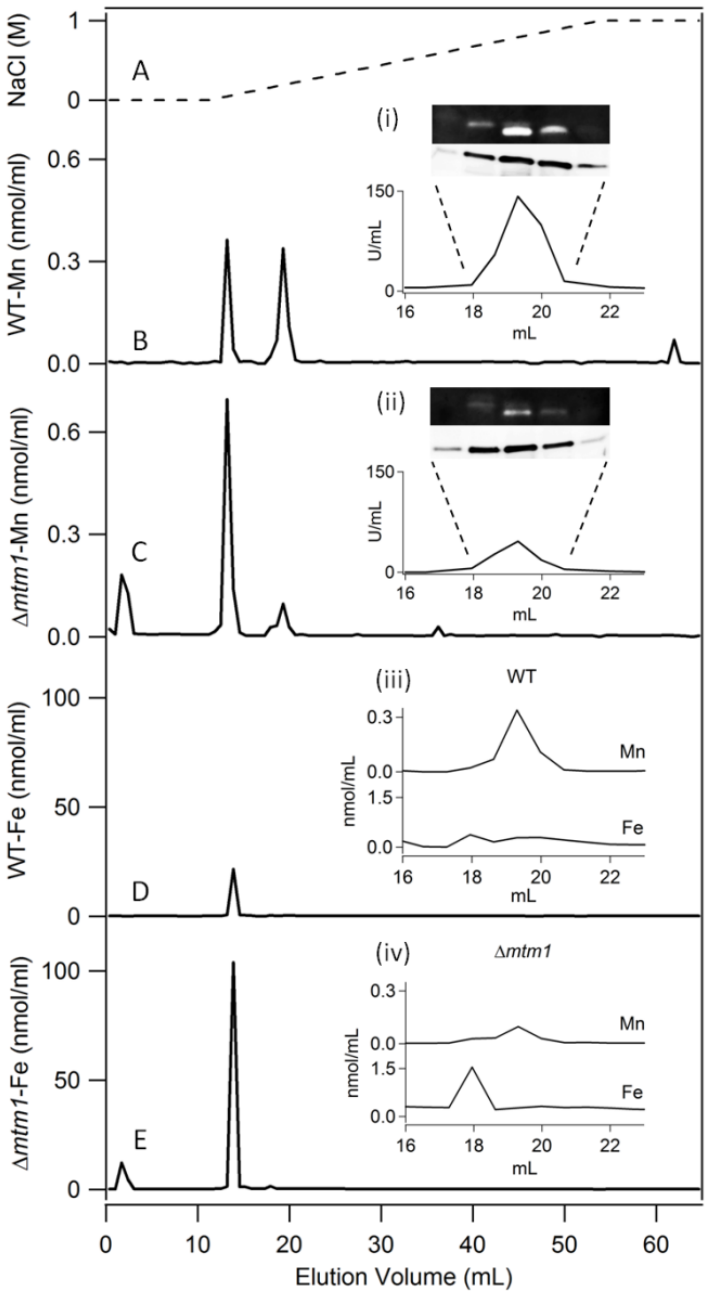

Figure V-12. Off-line ICP-MS anion-exchange chromatograms of soluble W303 and Δ*mtm1* mitochondria, Experiment 5. A, dotted line, salt gradient; B, W303, Mn concentrations in eluted fractions; C, Δ*mtm1*, Mn; D, W303, Fe; E, Δ*mtm1*, Fe. *Insets*, (*i*) W303, SOD2 activity gel and Western blot membrane against Sod2p from five adjacent fractions containing most Mn (*top*), SOD2 unit activity from corresponding fractions (*bottom*); (*ii*) Δ*mtm1*, same as (*i*); (*iii*) W303, close-up view of Mn and Fe profiles in 16 – 23 mL region; (*iv*) Δ*mtm1*, same as (*iii*).

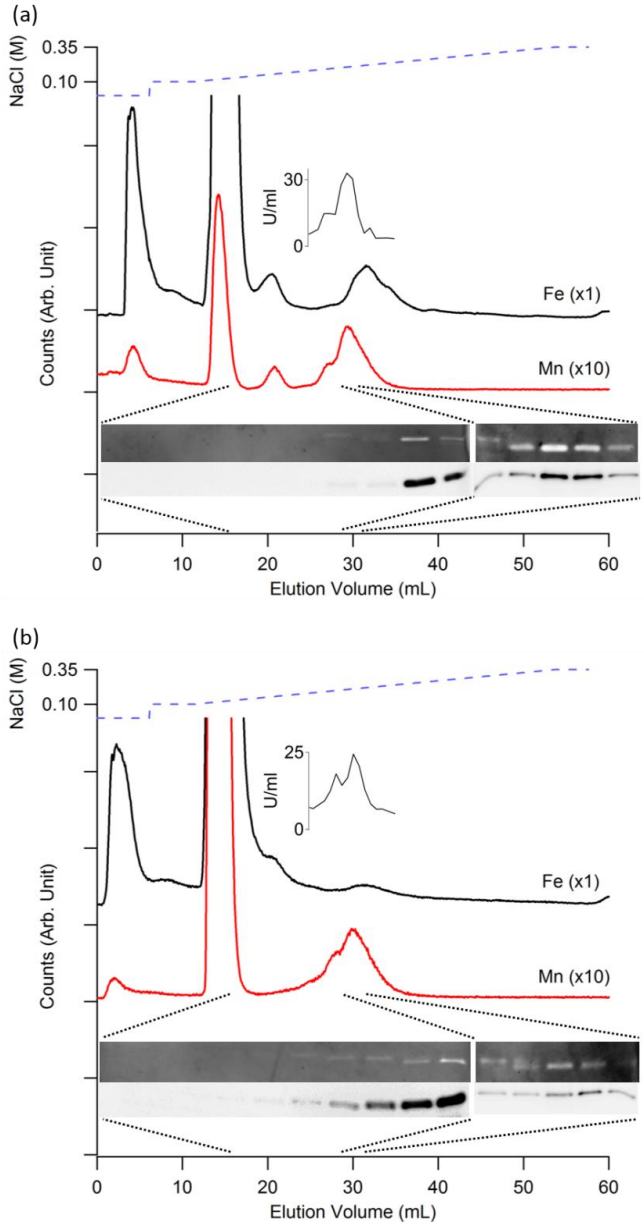

Figure V-13. On-line anion-exchange chromatograms of soluble (a) W303 and (b) Δ*mtm1* mitochondria in Experiment 6. Salt gradient is shown in dotted line. Mn detector responses are multiplied by 10. *Insets*, SOD2 unit activity of 15 fractions around 30 mL (*above Fe trace*); images of SOD2 activity gel and Western blot membrane against Sod2p (*below Mn trace*), from every other fraction in 16 – 28 mL (*left*), from five adjacent fractions (28 – 31 mL) containing most Mn (*right*). Differently-migrating MnSod2p bands in native gel are indicated by arrows above the lane exhibiting a differently charged form (reading from right to left). Contrast for the Western blots of the 16 – 28 mL fractions are greater than for the 28 – 31 mL blots.

The experiment was repeated but using a shallower salt gradient and with the ICP-MS on-line. Sod2p and SOD activity co-eluted with Mn around 30 mL in both of WT and Δ*mtm1* chromatograms (Figure V-13, Experiment 6) whereas the nearest Fe species eluted at a somewhat greater elution volume. These results again indicate that the extent of Fe mis-incorporation is not significant in Δmtm1 cells, and is no greater than in WT cells. SOD2 activity is diminished in Δ*mtm1* mitochondria, but not because of excessive Fe-misincorporation.

The Sod2p in fractions collected from the Mono Q column migrated in four different positions in native gels (see Figure V-13b, *insets*). Sod2p is active as a homotetramer,[53] suggesting that subunits may have different charge, with each combination migrating slightly differently on the column. The situation differs for Sod2p in fractions from size-exclusion columns, because the molecular masses of the different tetrameric forms are so similar (Figure V-8a). Sod2p tetramers in earlier Mono Q fractions are less negatively charged, and more Sod2p in Δ*mtm1* mitochondria eluted earlier compared with WT mitochondria. Although most Sod2p eluted around 30 mL, an Sod2p band was observable down to 20.6 mL (0.14 M NaCl) in the Δ*mtm1* chromatogram, whereas Sod2p was visible only down to 24.7 mL (0.17 M NaCl) in the WT chromatogram. This suggests that Sod2p might require a charge-altering post-translation modification such as phosphorylation to be active, and that the process is somehow diminished in Δ*mtm1* mitochondria. Consistent with this, threonine (T147 and T149) residues in Sod2p can be phosphorylated.[125]

Discussion

Disconnect between Fe accumulation and Sod2 inactivation

The Δ*mtm1/Sod2* mismetallation hypothesis implies that Fe accumulation and Sod2 inactivation in Δ*mtm1* mitochondria are *directly connected* in terms of a reaction network or mechanism. Our characterization of Δ*mtm1* cells grown under anaerobic conditions does not support such a connection. When grown under anaerobic conditions, this strain and the two others that have been studied under anaerobic conditions, namely Yah1p-depleted and Atm1p-depleted cells, do not exhibit the Fe-accumulation phenotype.[80,83] Yet one of these strains (Yah1p-depleted) exhibits strong SOD2 activity while the other two do not. This demonstrates that Fe accumulation is not tied to diminished SOD2 activity. A previous study[54] found that Fe/S cluster assembly was not affected by an Mtm1p-deficiency, suggesting a unique Fe accumulation phenotype. In contrast, our results indicate that the Fe accumulation phenotype in Δ*mtm1* mitochondria has all of the standard characteristics as seen in mitochondria deficient in Yfh1p,[122] Atm1p,[80] and Yah1p.[83] This includes the accumulation of Fe^{III} (phosphate and/or polyphosphate) oxyhydroxide nanoparticles, a defect in Fe/S cluster and heme levels, and an increase in ROS-associated damage. This commonality suggests that these phenomena, for all of these protein-deficiencies, are secondary effects that do not directly provide insight into the function of those proteins, including the function of Mtm1p. Thus, we should discount the Fe accumulation phenotype as we attempt to determine primary functions of Mtm1p and these other proteins.

The manganese-ome of yeast cells

Yeast cells grown in standard medium contain 20 – 40 μM Mn.[19,126] Although much remains to learn about the distribution of these Mn ions in the cell, we were impressed by the simplicity of the mitochondrial Mn LC traces. Our results suggest that the soluble fraction of yeast mitochondrial extracts contain a single Mn-protein, namely MnSod2p, and what appears to be a single LMM Mn species, namely $Mn_{2\text{-}3}$. (We cannot exclude the possibility that the $Mn_{2\text{-}3}$ peak includes multiple species that are unresolved). A small amount of HMM Mn (Mn_H) is also present. The majority of Mn in yeast cells (grown on minimal media without Mn supplementation) is EPR-active and yields a Mn^{II} hyperfine-split signal at g = 2.0.[19] As probed by ENDOR spectroscopy, multiple Mn^{II} complexes with phosphate and/or polyphosphate ligands contribute to this signal.[126] The location of these EPR-active species is unknown, but they do not appear to be located in mitochondria, as these organelles do not exhibit Mn^{II} EPR signals (Our early mitochondria preparations[124] exhibited Mn^{II} EPR, but this has not been observed subsequently.). Isolated vacuoles from cells grown in unsupplemented medium contained only 1.7 μM Mn and exhibited no EPR signals from Mn^{II} ions.[46] We propose that the LMM $Mn_{2\text{-}3}$ species in the mitochondria inserts into apo-Sod2 during maturation. The reaction, taking place in the mitochondrial matrix, is proposed to be

$$Mn^{II}\,L_{2\text{-}3} \;+\; apo\text{-}Sod2p \;\rightarrow\; L_{2\text{-}3} \;+\; MnSod2p$$

The concentration of $Mn_{2\text{-}3}$ increased when the growth medium was supplemented with $MnCl_2$, suggesting that it might also function to store Mn or sequester it to avoid deleterious side-reactions.

Apo-Sod2p-reactive Fe

Fe_{ASR} should be a mononuclear NHHS Fe^{II} species located in the mitochondrial matrix of Δ*mtm1* mitochondria – the Fe^{II} equivalent of Mn_{2-3}. We initiated our studies assuming that the majority of Fe that accumulated in Δ*mtm1* mitochondria would be this type of species. Our biophysical study of Δ*mtm1* mitochondria immediately indicated that the bulk of the Fe in these organelles was Fe^{III} oxyhydroxide (phosphate or polyphosphate) nanoparticles, as the Mössbauer spectroscopic pattern was indistinguishable from that exhibited by such nanoparticles in Yah1 and Atm1-depleted strains. This is consistent with previous XAS results which suggested that *Fe_{ASR}* constitutes an insignificant portion of the Fe in Δ*mtm1* mitochondria.[55] The XAS results indicated approximately *equal* proportions of Fe^{II} and Fe^{III} in Δ*mtm1* mitochondria whereas Mössbauer spectra indicate that all but a few percent of the Fe is in the Fe^{III} oxidation state.

The dominance of nanoparticles rendered the problem of identifying *Fe_{ASR}* more difficult because it meant that we were searching for a tiny amount of a mononuclear HS Fe^{II} complex in an vast excess of inert Fe. We first considered the NHHS Fe^{II} species which afforded a 2% quadrupole doublet in the Δ*mtm1* mitochondrial Mössbauer spectrum. However, similar doublets are also present in spectra of mitochondria from strains that accumulate nanoparticles but do not misincorporate Fe into apo- Sod2p - e.g. those deficient in Yah1p.[83] Fe_{ASR} might *contribute* to the broad NHHS doublet, but if so, it would represent only a small proportion of it.

This suggested that Fe_{ASR} should be present at *very* low concentrations with *no* chance of being characterized or even detected by Mössbauer spectroscopy. Thus, we turned our attention to LC-ICP-MS with the goal of identifying Fe_{ASR} and the Fe-mismetallated FeSod2p. We regard Fe_3 as a viable candidate for Fe_{ASR}, because it is a LMM species with a molecular mass similar to that of $Mn_{2\text{-}3}$. In this case, the mismetallation reaction would be

$$Fe^{II}L_3 \; + \; apo\text{-}Sod2p \; \rightarrow \; L_3 \; + \; FeSod2p$$

The most likely candidate for FeSod2p was Fe_{100}, based on molecular mass. However, the fraction of mismetallated Sod2p present in Δ*mtm1* mitochondria, assuming Fe_{100} to be this species, was no different than in WT mitochondria. This was unexpected, and it casts doubt on this assumption.

We were also unable to reconcile our size-exclusion LC-ICP results with a previous study.[54] The previous Mono Q chromatograms of WT mitochondrial extracts displayed only one Mn peak (MnSod2) which was absent in chromatograms of Δ*mtm1* mitochondria. In contrast, we observed the MnSod2 peak in chromatograms from *both* WT and Δ*mtm1* mitochondria. Moreover, our chromatograms exhibited a second major Mn species that has not been observed previously.

In the earlier study, no Fe peaks were observed in the WT chromatogram while two Fe peaks were observed in the Δ*mtm1* chromatogram (one that comigrated with Sod2p and one that eluted in the void volume). We observed a major Fe species in both WT and Δ*mtm1* chromatograms that did not comigrate with Sod2p, as well as minor Fe peaks that comigrated in the vicinity of MnSod2p. We did not observe an Fe species that

comigrates *precisely* with MnSod2p. We cannot explain these differences. In the previous study, the bulk of Fe in Δ*mtm1* mitochondria was concluded to be associated with Sod2p (as FeSod2p). Based on our results, we conclude that only a tiny amount of mitochondrial Fe could be associated with Sod2p, and that the level of FeSod2p in Δ*mtm1* cells is similar to that in WT cells.

Observed differences may arise from differences in the yeast strain (W303 vs. By4741), growth medium (minimal vs. YPD), growth conditions or preparation methods, but we have no supporting evidence for any of these possibilities. It is also possible that additional FeSod2p formed in Δ*mtm1* mitochondria but that it was less stable than MnSod2p and that it localized primarily in the pellet of our samples. However, yeast FeSod2p is known to be sufficiently stable and soluble for crystallization studies.[127]

Physiological role of Mtm1p

Determining the function of Mtm1p – defined by the species transported by this IM mitochondrial carrier – is a continuing challenge. Our results suggest that the lower SOD2 activity observed in Δ*mtm1 S. cerevisiae* arises, not because of excessive mismetallation, but because a significant portion of Sod2p is misfolded or degraded, and/or because the expression-level of SOD2 is diminished. One possibility is that Mtm1p imports a Maturation Factor (MF) required to help mature apo-Sod2p (Figure V-14). Other proteins that exhibit this phenotype (Ssq1p, Grx5p and Atm1p) might also be involved in apo-Sod2p maturation, which includes installing Mn and folding the protein.

In the absence of Mtm1p (or these other proteins), the rate of maturation might slow such that apo-Sod2p misfolds or does not become metallated at as fast a rate as is observed in WT cells. The slow rate of maturation might cause the Mn species that is used for metallation (e.g. $Mn_{2\text{-}3}$) to accumulate. Under Mn-supplemented conditions, this Mn species would be imported at a greater rate.

Another possiblity, suggested by the results of Figure V-13, is that Mtm1p helps regulate MnSod2 activity and/or stability by promoting a reaction that affects the *charge* on the protein. Phosphorylation reactions are used to regulate numerous mitochondrial enzymes,[128,129] and are involved in the H_2O_2 stress response.[130] Our results are consistent with the possiblity that in the absence of Mtm1p, the degree of phosphorylation declines. However, further studies are required to interpret these results more definitively.

In WT cells, Sod2p is *mainly* metallated with Mn. Fridovich purified Sod2p from *S. cerevisiae*, and found sufficient Fe in the purified Mn-protein solution for no more than 6% of it to be Fe-bound.[91] Approximately 80% of the Sod2p isolated by Whittaker *et al.*[131] from the same organism contained Mn, with ~ 20% containing Fe. Jeong *et al.*[132] purified the Sod2p from the closely-related *Schizosaccharomyces pombe* and was unable to detect *any* Fe (or Cu, Zn, or Ni) in the purified enzyme; the only metal detected was Mn. On the other hand, Kang *et al.*[127] determined the X-ray diffraction crystal structure of the Fe-metallated *S. cerevisiae* Sod2p to 1.79 Å resolution. In cell grown under normal conditions, the extent of mismetallation seems to vary from 0% to 20%. The mismetallated protein used for crystallography was obtained by overexpressing yeast apo-Sod2p in *E. coli* grown in medium supplemented with 100 μM Fe, which may have

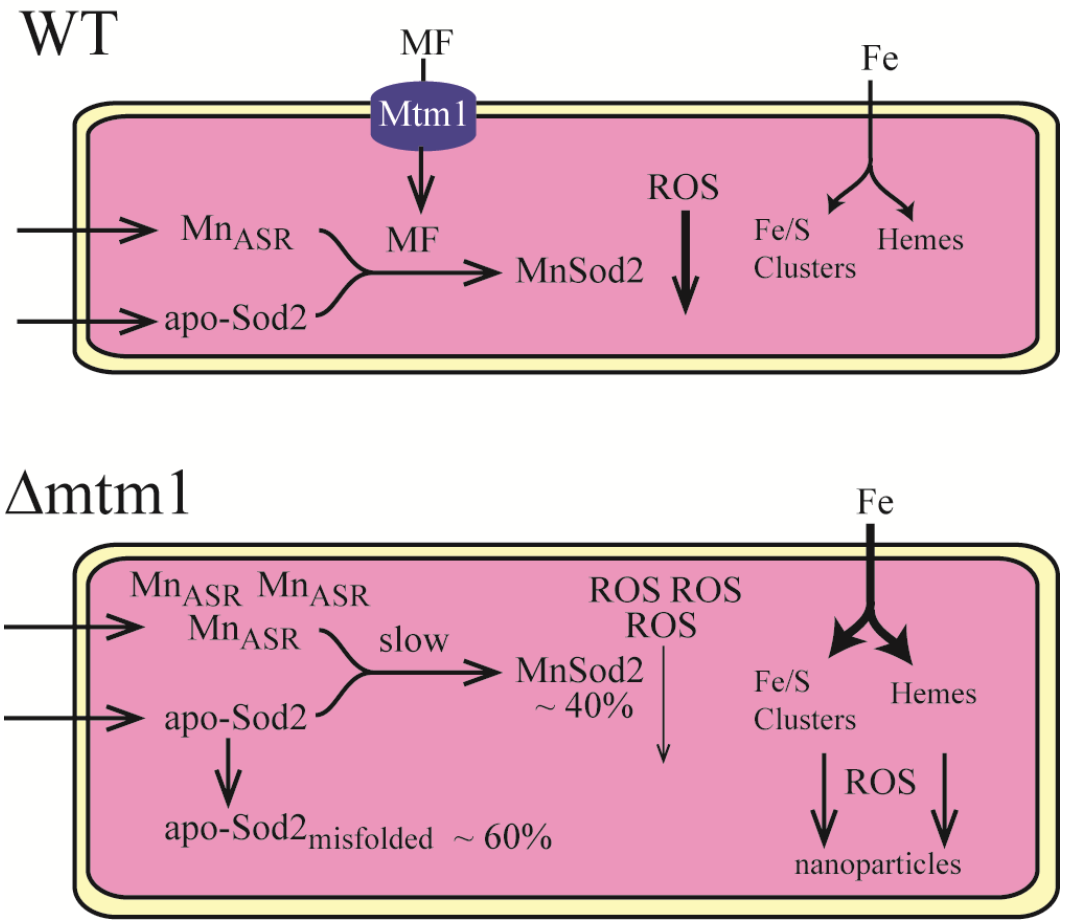

Figure V-14. Possible role of Mtm1p as an importer of a factor (presumed to be a small molecule) that helps mature apo-Sod2p, perhaps involving Mn insertion or protein folding. In the absence of Mtm1p, the rate of maturation slows which causes a build-up of Mn_{ASR} and immature Sod2p that eventually misfolds. The lack of functional MnSod2p increases the concentration of ROS in the matrix, which triggers the Fe accumulation phenotype.

increased the level of mismetallation. Using Mössbauer spectroscopy, Fleisch-hacker *et al.*[133] found that 40% of the Fe in whole *E. coli* cells (grown on medium supplemented with just 10 μM ^{57}Fe) was mononuclear NHHS Fe^{II}. Higher levels of such Fe might be present in cells grown with 100 μM Fe in the medium. Such Fe, consisting of one or

more octahedral complexes with a coordination environment dominated by O and/or N ligands, is the type of Fe expected for mismetallation.

There is no doubt that apo-Sod2p can and does mismetallate with Fe, but our results do not support the view that there is an *increased* level of Fe mismetallation in Δ*mtm1* cells. Rather, they suggest that in Δ*mtm1* cells there is a decline in the degree to which apo-Sod2p is activated, folded, metallated or matured. Establishing the molecular details of this will be a future challenge, but should provide further insight into the physiological role of this fascinating protein.

CHAPTER VI

SUMMARY AND FUTURE DIRECTIONS

Summary

In this dissertation, fundamental issues of cellular Fe metabolism, including those in trafficking and regulation, were addressed using an integrative biophysical and bioanalytical approach. One issue addressed was how yeast cells regulate and traffic Fe during different growth stages. The study described in Chapter III demonstrated that cells regulate Fe-import differently depending on growth mode (rate). Iron was well regulated during exponential growth but not during post-exponential growth. During exponential growth, rates of Fe import and cell growth were matched, affording stable cellular Fe concentrations. As the cells transitioned to post-exponential growth, the high-affinity Fe import rate declined slower than the cell growth rate. This caused Fe to accumulate, initially as Fe^{III} oxyhydroxide nanoparticles and eventually as additional mitochondrial and vacuolar Fe. Once in slow-growth mode, import and growth rates were again matched, and the cellular Fe concentration was again stable. Fermenting cells grown on minimal medium (MM) grew more slowly during exponential phase and transitioned into a true stationary state as glucose levels declined. The Fe concentration of MM-grown cells that just entered stationary state was similar to that of YPAD-grown cells, but MM-grown cells continued to accumulate Fe in stationary state. Fe initially accumulated as nanoparticles and Fe^{II} species, but it eventually accumulated as vacuolar Fe and nanoparticles. 5-day old MM-grown cells had less ROS damage than younger

cells suggesting that Fe concentration alone does not accurately predict the extent of ROS damage; growth medium, growth rate, and duration of growth are also factors.

The mode and rate of growth at the time of harvesting dramatically affected cellular Fe content. A mathematical model of Fe metabolism in a growing cell was developed. The model included Fe import via a regulated high-affinity pathway and an unregulated low-affinity pathway, Fe import from the cytosol into vacuoles and mitochondria, and nanoparticle formation. The model captured essential behavior and demonstrated that the cell regulates its Fe import rate in accordance with its overall growth rate. The lack of regulation of Fe in yeast is perhaps unique relative to the tight regulation of other cellular metabolites. This phenomenon likely derives from the unique chemistry of Fe.

During the course of this study, it became apparent that the nutrient status of the growth medium strongly affected the Fe content of the cell. Cells grown on minimal medium (MM) but deficient in adenine accumulated Fe as nonheme high spin (NHHS) Fe^{II} complexes, possibly located in the cytosol, as they transitioned from exponential to stationary phase. A model was developed in which redox status and pH determine Fe speciation in vacuoles. Vacuoles of adenine-deficient cells may be more reducing than those of MM-grown cells due to the response of these cells to the deficiency, thereby favoring the reduction of vacuolar Fe^{III} and their exit into the cytosol. Adenine-deficient cells suffered less oxidative stress despite the abundance of HS Fe^{II} complexes that should be susceptible to Fenton chemistry.

Reducing initial glucose levels in MM diminished the Fe concentration of stationary state cells. These cells were dominated by vacuolar Fe^{III} and nanoparticles regardless of glucose level. The extent of oxidative damage was proportional to glucose level but not to cellular Fe.

The Fe concentration of 5-day-old rapamycin-treated cells was less than that of equivalent MM-grown cells, suggesting that rapamycin inhibits Fe import. These TOR-inhibited cells contained more NHHS Fe^{II}, implying highly reduced vacuoles, consistent with the observed low level of oxidative damage. The co-presence of Fe^{III} nanoparticles in these cells suggests that rapamycin shifts vacuoles to more basic conditions.

Most Fe in cells grown with extra yeast nitrogen base, amino acids and bases was HS Fe^{III}, probably located in the vacuoles. The vacuoles of these cells are probably more acidic than normal such that they can accommodate high concentrations of HS Fe^{III} species. This effect was not the simple sum of the effects of the individual added nutrients, illustrating the complexity of cellular metabolism. Mitochondrial heme levels were also influenced by nutrient status. The ability to alter Fe metabolism by changing nutrient components illustrates the sensitivity of Fe content to the growth medium.

The last issue addressed involved the putative 'bioavailable' Fe pool in Δ*mtm1* mitochondria. Previous studies found that deleting the mitochondrial carrier gene MTM1 causes Fe to accumulate in mitochondria and Mn superoxide dismutase 2 (SOD2) activity to decline. The most popular explanation of this is that some accumulated Fe misincorporates into apo-Sod2p. Mössbauer spectroscopy was used here to determine that most of the accumulated Fe was Fe^{III} nanoparticles which are unlikely to

misincorporate into apo-Sod2p. Under anaerobic conditions, Fe did not accumulate yet SOD2 activity remained low, suggesting that the two phenomena are independent.

Mn concentrations were two-fold higher in Δ*mtm1* mitochondria than in WT mitochondria. Soluble extracts from such samples were subjected to size-exclusion LC with an on-line ICP-MS. Two major Mn peaks were observed, one due to MnSod2p and the other to Mn species with a low molecular mass (LMM) of 2-3 kDa. Most Mn in WT mitochondria was associated with MnSod2p, whereas most Mn in Δ*mtm1* mitochondria was associated with the LMM species. The LMM Mn concentration increased in cells grown on high $MnCl_2$ while the MnSod2p level remained unchanged. Corresponding Fe traces showed numerous peaks, however none comigrated precisely with MnSod2p. This suggests that deleting *MTM1* diminishes SOD2 activity by some means other than Fe misincorporation. A portion of Sod2p in Δ*mtm1* mitochondria might be unfolded or immature. Mtm1p may function to import a species required for apo-Sod2p maturation, activity or stability. The LMM Mn species may deliver Mn into apo-Sod2p during maturation.

Future Directions

Several directions should be pursued so as to enhance our understanding of Fe regulation and trafficking in biological systems. First of all, we have not completely understood our first issue, which is the unregulated Fe uptake in WT yeast cells. The proposed model assumes that the low affinity Fe uptake system, probably Fet4p, is responsible for the Fe build-up. However, this should be confirmed, perhaps by

examining mutant strains with FET4 and/or SMF1 deleted. If these cells were monitored for Fe accumulation during the different growth stages, it may be possible to confirm which system is responsible for the enormous Fe build-up.

In the study of nutrient effect on Fe content in Chapter IV, we reported that the level of glucose in medium determines the amount of Fe uptake. The glucose level is directly related to the growth rate as we have shown in Chapter III. The major growth regulator in response to glucose is PKA, a protein kinase. We are currently missing a connection between glucose metabolism and Fe uptake regulation. However, a catalytic subunit of PKA, Tpk1p, negatively and transcriptionally regulates high affinity Fe uptake system,[134] which seems incongruent with our results. In our study, Fet3p expression level decreased as glucose level in medium decreased. In spite of the discrepancy, studying Δ*tpk1* and Tpk1p-overexpressed strains with our biophysical tools may provide important insights on how glucose metabolism regulates Fe uptake systems.

Another cell growth regulator, TORC1 which responds to both nitrogen and carbon nutrients, has also been shown to determine the level of Fe accumulation and the fate of Fe in the cell (whether to become NHHS Fe^{II} or Fe^{III} nanoparticles). However, there is also a missing part to connect TORC1 pathway and Fe regulation. Based on literature, a human version (tristetraprolin) of Cth1p/2p is derepressed by inhibition of mTOR (mammalian TOR) and degradation of TfR1 mRNA.[135] This is consistent with our observation that rapamycin effectively inhibits Fe uptake. Although Cth1p/2p are not known to regulate either Fet3p or Fet4p, studying Δ*cth1*, Δ*cth2* or double mutant yeast

strains may help reveal the relation among TORC1 pathway, nitrogen metabolism and Fe regulation.

In Chapter V, we hypothesized that Mtm1p may play a role in SOD2 maturation rather than in mitochondrial ISC assembly. However, further evidence for this before it can be established. Since Mtm1p is a member of mitochondrial carrier family, it would be helpful to determine what species Mtm1p transports. Δ*mtm1* and Mtm1p-overexpressed cells could be employed for this. Assuming that Mtm1p imports factor, X, Δ*mtm1*mitochondria may not accumulate X whereas Mtm1p-overexpressed cells may accumulate it more than in the WT strain. We can isolate the mitochondrial soluble fractions from each strain and subject them to LC-ICP-MS. Then we can compare all parameters between two strains, including UV trace at 260 nm, sulfur, phosphorous and metals. If the X is protein, we may be able to find it from UV trace. If it is metal complex or sulfur, phosphorous-containing species, we may be able to find it from all other traces. This experiment may be help identify what Mtm1p transports and eventually help elucidate its role in the SOD2 maturation or mitochondrial Fe homeostasis.

The Labile Iron Pool (LIP) is intriguing because it may play a central role in Fe trafficking in biological systems. In this dissertation, we reported a couple of cases in which yeast cells accumulated high concentration of NHHS Fe^{II} ions. Although LIP may be only a part of the NHHS Fe^{II} pool, many researchers agree that the LIP functions mainly in ferrous form, and thereby the NHHS Fe^{II} observed during our research is a great candidate for the LIP. There are some conditions that cells accumulate more

NHHS Fe^{II} than normal as described in Chapter IV. Among them, adenine-deficient cells accumulated the highest concentration of Fe, although there were more than one species. In addition, there was less than 15% of vacuolar Fe in the cells of some extreme cases, which minimizes the interference by vacuolar Fe after cell disruption. We can gently break up cells with adenine deficiency and subject the soluble fraction (probably cytosolic fraction) into LC-ICP-MS to isolate the NHHS Fe^{II} species.

Another promising experiment using LC-ICP-MS would be to identify low-molecular-mass (LMM) Mn species. Since Δ*mtm1* mitochondria have been demonstrated to accumulate high level of LMM Mn species and only one protein-associated Mn, isolation of this species appears simpler than isolating LMM Fe complex.

REFERENCES

1. Crichton, R. R. (2008) Chapter 13. Iron: Essential for almost all life, In *Biological Inorganic Chemistry*, pp 211-240, Elsevier, Amsterdam, Netherlands.
2. Cotruvo, J. A., Jr., and Stubbe, J. (2012) Metallation and mismetallation of iron and manganese proteins in vitro and in vivo: the class I ribonucleotide reductases as a case study, *Metallomics 4*, 1020-1036.
3. Costas, M., Mehn, M. P., Jensen, M. P., and Que, L. (2004) Dioxygen activation at mononuclear nonheme iron active sites: Enzymes, models, and intermediates, *Chem. Rev. 104*, 939-986.
4. Frey, P. A., Hegeman, A. D., and Ruzicka, F. J. (2008) The radical SAM superfamily, *Crit. Rev. Biochem. Mol. Biol. 43*, 63-88.
5. Imlay, J. A. (2003) Pathways of oxidative damage, *Annu. Rev. Microbiol. 57*, 395-418.
6. Shakoury-Elizeh, M., Tiedeman, J., Rashford, J., Ferea, T., Demeter, J., Garcia, E., Rolfes, R., Brown, P. O., Botstein, D., and Philpott, C. C. (2004) Transcriptional remodeling in response to iron deprivation in *Saccharomyces cerevisiae*, *Molecular Biology of the Cell 15*, 1233-1243.
7. Yamaguchi-Iwai, Y., Ueta, R., Fukunaka, A., and Sasaki, R. (2002) Subcellular localization of Aft1 transcription factor responds to iron status in *Saccharomyces cerevisiae*, *J. Biol. Chem. 277*, 18914-18918.

8. Li, H., Mapolelo, D. T., Dingra, N. N., Keller, G., Riggs-Gelasco, P. J., Winge, D. R., Johnson, M. K., and Outten, C. E. (2011) Histidine 103 in Fra2 Is an iron-sulfur cluster ligand in the [2Fe-2S] Fra2-Grx3 complex and is required for in vivo iron signaling in yeast, *J. Biol. Chem. 286*, 867-876.

9. Van Ho, A., Ward, D. M., and Kaplan, J. (2002) Transition metal transport in yeast, *Annu. Rev. Microbiol. 56*, 237-261.

10. Lill, R., and Müehlenhoff, U. (2008) Maturation of iron-sulfur proteins in eukaryotes: Mechanisms, connected processes, and diseases, *Annu. Rev. Biochem 77*, 669-700.

11. Dancis, A., Klausner, R. D., Hinnebusch, A. G., and Barriocanal, J. G. (1990) Genetic-evidence that ferric reductase is required for iron uptake in *Saccharomyces-cerevisiae*, *Mol. Cell. Biol. 10*, 2294-2301.

12. Georgatsou, E., and Alexandraki, D. (1999) Regulated expression of the *Saccharomyces cerevisiae* Fre1p/Fre2p Fe/Cu reductase related genes, *Yeast 15*, 573-584.

13. Yun, C.-W., Bauler, M., Moore, R. E., Klebba, P. E., and Philpott, C. C. (2001) The role of the FRE family of plasma membrane reductases in the uptake of siderophore-iron in *Saccharomyces cerevisiae*, *J. Biol. Chem. 276*, 10218-10223.

14. Stearman, R., Yuan, D. S., Yamaguchi-Iwai, Y., Klausner, R. D., and Dancis, A. (1996) A permease-oxidase complex involved in high-affinity iron uptake in yeast, *Science 271*, 1552-1557.

15. Heymann, P., Ernst, J., and Winkelmann, G. (1999) Identification of a fungal triacetylfusarinine C siderophore transport gene (TAF1) in *Saccharomyces cerevisiae* as a member of the major facilitator superfamily, *BioMetals 12*, 301-306.

16. Heymann, P., Ernst, J. F., and Winkelmann, G. (2000) Identification and substrate specificity of a ferrichrome-type siderophore transporter (Arn1p) in *Saccharomyces cerevisiae*, *FEMS Microbiol. Lett. 186*, 221-227.

17. Yun, C.-W., Ferea, T., Rashford, J., Ardon, O., Brown, P. O., Botstein, D., Kaplan, J., and Philpott, C. C. (2000) Desferrioxamine-mediated iron uptake in *Saccharomyces cerevisiae* : Evidence for two pathways of iron uptake, *J. Biol. Chem. 275*, 10709-10715.

18. Eide, D., Davis-kaplan, S., Jordan, I., Sipe, D., and Kaplan, J. (1992) Regulation of iron uptake in *Saccharomyces cerevisiae* - the ferrireductase and fe(II) transporter are regulated independently, *J. Biol. Chem. 267*, 20774-20781.

19. Holmes-Hampton, G. P., Jhurry, N. D., McCormick, S. P., and Lindahl, P. A. (2013) Iron content of *Saccharomyces cerevisiae* cells grown under iron-deficient and iron-overload conditions, *Biochemistry 52*, 105-114.

20. Waters, B. M., and Eide, D. J. (2002) Combinatorial control of yeast FET4 gene expression by iron, zinc, and oxygen, *J. Biol. Chem. 277*, 33749-33757.

21. Dix, D. R., Bridgham, J. T., Broderius, M. A., Byersdorfer, C. A., and Eide, D. J. (1994) The FET4 gene encodes the low-affinity Fe(II) transport protein of *Saccharomyces cerevisiae*, *J. Biol. Chem. 269*, 26092-26099.

22. Dix, D., Bridgham, J., Broderius, M., and Eide, D. (1997) Characterization of the FET4 protein of yeast - Evidence for a direct role in the transport of iron, *J. Biol. Chem. 272*, 11770-11777.

23. Cyert, M. S., and Philpott, C. C. (2013) Regulation of cation balance in *Saccharomyces cerevisiae*, *Genetics 193*, 677-713.

24. Chen, X. Z., Peng, J. B., Cohen, A., Nelson, H., Nelson, N., and Hediger, M. A. (1999) Yeast SMF1 mediates H^+-coupled iron uptake with concomitant uncoupled cation currents, *J. Biol. Chem. 274*, 35089-35094.

25. Kakhlon, O., and Cabantchik, Z. I. (2002) The labile iron pool: characterization, measurement, and participation in cellular processes, *Free Radic. Biol. Med. 33*, 1037-1046.

26. Hassett, R. F., Romeo, A. M., and Kosman, D. J. (1998) Regulation of high affinity iron uptake in the yeast *Saccharomyces cerevisiae* - Role of dioxygen and Fe(II), *J. Biol. Chem. 273*, 7628-7636.

27. Konijn, A. M., Glickstein, H., Vaisman, B., Meyron-Holtz, E. G., Slotki, I. N., and Cabantchik, Z. I. (1999) The cellular labile iron pool and intracellular ferritin in K562 cells, *Blood 94*, 2128-2134.

28. Hider, R. C., and Kong, X. L. (2011) Glutathione: a key component of the cytoplasmic labile iron pool, *BioMetals 24*, 1179-1187.

29. Shvartsman, M., and Cabantchik, Z. I. (2012) Intracellular iron trafficking: role of cytosolic ligands, *BioMetals 25*, 711-723.

30. Berg, J. M., Tymoczko, J. L., and Lubert, S. (2002) In *Biochemistry*, W H Freeman, New York.

31. Froschauer, E. M., Schweyen, R. J., and Wiesenberger, G. (2009) The yeast mitochondrial carrier proteins Mrs3p/Mrs4p mediate iron transport across the inner mitochondrial membrane, *Biochim. Biophys. Acta (BBA) - Biomembranes 1788*, 1044-1050.

32. Muhlenhoff, U., Stadler, J. A., Richhardt, N., Seubert, A., Eickhorst, T., Schweyen, R. J., Lill, R., and Wiesenberger, G. (2003) A specific role of the yeast mitochondrial carriers Mrs3/4p in mitochondrial iron acquisition under iron-limiting conditions, *J. Biol. Chem. 278*, 40612-40620.

33. Petrat, F., de Groot, H., Sustmann, R., and Rauen, U. (2002) The chelatable iron pool in living cells: A methodically defined quantity, *Biol. Chem. 383*, 489-502.

34. Tangerås, A., Flatmark, T., Bäckström, D., and Ehrenberg, A. (1980) Mitochondrial iron not bound in heme and iron-sulfur centers. Estimation, compartmentation and redox state, *Biochim. Biophys. Acta (BBA) - Bioenergetics 589*, 162-175.

35. Holmes-Hampton, G. P., Miao, R., Morales, J. G., Guo, Y. S., Münck, E., and Lindahl, P. A. (2010) A nonheme high-spin ferrous pool in mitochondria isolated from fermenting *Saccharomyces cerevisiae*, *Biochemistry 49*, 4227-4234.

36. Pandey, A., Yoon, H., Lyver, E. R., Dancis, A., and Pain, D. (2012) Identification of a Nfs1p-bound persulfide intermediate in Fe-S cluster synthesis by intact mitochondria, *Mitochondrion 12*, 539-549.

37. Lutz, T., Westermann, B., Neupert, W., and Herrmann, J. M. (2001) The mitochondrial proteins Ssq1 and Jac1 are required for the assembly of iron sulfur clusters in mitochondria, *J. Mol. Biol. 307*, 815-825.

38. Lill, R. (2009) Function and biogenesis of iron-sulphur proteins, *Nature 460*, 831-838.

39. Brett, C. L., Kallay, L., Hua, Z., Green, R., Chyou, A., Zhang, Y., Graham, T. R., Donowitz, M., and Rao, R. (2011) Genome-wide analysis reveals the vacuolar pH-stat of *Saccharomyces cerevisiae*, *PLoS One 6*.

40. Klionsky, D. J., Herman, P. K., and Emr, S. D. (1990) The fungal vacuole - composition, function, and biogenesis, *Microbiol. Rev. 54*, 266-292.

41. White, C., and Gadd, G. M. (1986) Uptake and cellular distribution of copper, cobalt and cadmium in strains of *Saccharomyces cerevisiae* cultured on elevated concentrations of these metals, *FEMS Microbiol. Lett. 38*, 277-283.

42. Li, L. T., Chen, O. S., Ward, D. M., and Kaplan, J. (2001) CCC1 is a transporter that mediates vacuolar iron storage in yeast, *J. Biol. Chem. 276*, 29515-29519.

43. Li, L., Bagley, D., Ward, D. A., and Kaplan, J. (2008) Yap5 is an iron-responsive transcriptional activator that regulates vacuolar iron storage in yeast, *Mol. Cell. Biol. 28*, 1326-1337.

44. Puig, S., Askeland, E., and Thiele, D. J. (2005) Coordinated remodeling of cellular metabolism during iron deficiency through targeted mRNA degradation, *Cell 120*, 99-110.

45. Philpott, C. C., and Protchenko, O. (2008) Response to Iron Deprivation in *Saccharomyces cerevisiae*, *Eukaryot. Cell 7*, 20-27.

46. Cockrell, A. L., Holmes-Hampton, G. P., McCormick, S. P., Chakrabarti, M., and Lindahl, P. A. (2011) Mössbauer and EPR study of iron in vacuoles from fermenting *Saccharomyces cerevisiae*, *Biochemistry 50*, 10275-10283.

47. Broach, J. R. (2012) Nutritional control of growth and development in yeast, *Genetics 192*, 73-105.

48. Borgstahl, G. E. O., Parge, H. E., Hickey, M. J., Beyer, W. F., Hallewell, R. A., and Tainer, J. A. (1992) The structure of human mitochondrial manganese superoxide-dismutase reveals a novel tetrameric interface of 2 4-helix bundles, *Cell 71*, 107-118.

49. Vance, C. K., and Miller, A. F. (1998) Simple proposal that can explain the inactivity of metal-substituted superoxide dismutases, *Journal of the American Chemical Society 120*, 461-467.

50. Gerber, J., Muhlenhoff, U., and Lill, R. (2003) An interaction between frataxin and Isu1/Nfs1 that is crucial for Fe/S cluster synthesis on Isu1, *Embo Reports 4*, 906-911.

51. Tsai, C.-L., and Barondeau, D. P. (2010) Human frataxin is an allosteric switch that activates the Fe−S cluster biosynthetic complex, *Biochemistry 49*, 9132-9139.

52. Kispal, G., Csere, P., Prohl, C., and Lill, R. (1999) The mitochondrial proteins Atm1p and Nfs1p are essential for biogenesis of cytosolic Fe/S proteins, *EMBO J. 18*, 3981-3989.

53. Luk, E., Carroll, M., Baker, M., and Culotta, V. C. (2003) Manganese activation of superoxide dismutase 2 in *Saccharomyces cerevisiae* requires *MTM1*, a member of the mitochondrial carrier family, *Proc. Natl. Acad. Sci. U.S.A. 100*, 10353-10357.

54. Yang, M., Cobine, P. A., Molik, S., Naranuntarat, A., Lill, R., Winge, D. R., and Culotta, V. C. (2006) The effects of mitochondrial iron homeostasis on cofactor specificity of superoxide dismutase 2, *EMBO J. 25*, 1775-1783.

55. Naranuntarat, A., Jensen, L. T., Pazicni, S., Penner-Hahn, J. E., and Culotta, V. C. (2009) The interaction of mitochondrial iron with manganese superoxide dismutase, *J. Biol. Chem. 284*, 22633-22640.

56. Palmieri, F., Pierri, C. L., De Grassi, A., Nunes-Nesi, A., and Fernie, A. R. (2011) Evolution, structure and function of mitochondrial carriers: a review with new insights, *Plant J. 66*, 161-181.

57. Beyer, W. F., Jr., and Fridovich, I. (1991) *In vivo* competition between iron and manganese for occupancy of the active-site region of the manganese-superoxide dismutase of *Escherichia coli*, *J. Biol. Chem. 266*, 303-308.

58. DeRisi, J. L., Iyer, V. R., and Brown, P. O. (1997) Exploring the metabolic and genetic control of gene expression on a genomic scale, *Science 278*, 680-686.

59. Haurie, V., Boucherie, H., and Sagliocco, F. (2003) The snf1 protein kinase controls the induction of genes of the iron uptake pathway at the diauxic shift in *Saccharomyces cerevisiae*, *J. Biol. Chem. 278*, 45391-45396.

60. Ronen, M., and Botstein, D. (2006) Transcriptional response of steady-state yeast cultures to transient perturbations in carbon source, *Proc. Natl. Acad. Sci. U.S.A. 103*, 389-394.

61. Loewith, R., and Hall, M. N. (2011) Target of rapamycin (TOR) in nutrient signaling and growth control, *Genetics 189*, 1177-1201.

62. De Virgilio, C. (2012) The essence of yeast quiescence, *FEMS Microbiol. Rev. 36*, 306-339.

63. Nishida, K., and Silver, P. A. (2012) Induction of biogenic magnetization and redox control by a component of the target of rapamycin complex 1 signaling pathway, *PLoS Biol. 10*, e1001269.

64. Fabrizio, P., Pozza, F., Pletcher, S. D., Gendron, C. M., and Longo, V. D. (2001) Regulation of longevity and stress resistance by Sch9 in yeast, *Science 292*, 288-290.

65. Pan, Y., Schroeder, E. A., Ocampo, A., Barrientos, A., and Shadel, G. S. (2011) Regulation of yeast chronological life span by TORC1 via adaptive mitochondrial ROS signaling, *Cell Metab. 13*, 668-678.

66. Wei, M., Fabrizio, P., Hu, J., Ge, H., Cheng, C., Li, L., and Longo, V. D. (2008) Life span extension by calorie restriction depends on Rim15 and transcription factors downstream of Ras/PKA, Tor, and Sch9, *PLoS Genet. 4*.

67. Reverter-Branchat, G., Cabiscol, E., Tamarit, J., and Ros, J. (2004) Oxidative damage to specific proteins in replicative and chronological-aged *Saccharomyces cerevisiae* - Common targets and prevention by calorie restriction, *J. Biol. Chem. 279*, 31983-31989.

68. Replogle, K., Hovland, L., and Rivier, D. H. (1999) Designer deletion and prototrophic strains derived from *Saccharomyces cerevisiae* strain W303-1a, *Yeast 15*, 1141-1149.

69. Firestine, S. M., Misialek, S., Toffaletti, D. L., Klem, T. J., Perfect, J. R., and Davisson, V. J. (1998) Biochemical role of the *Cryptococcus neoformans* ADE2 protein in fungal *de novo* purine biosynthesis, *Arch. Biochem. Biophys. 351*, 123-134.

70. Sharma, K. G., Kaur, R., and Bachhawat, A. K. (2003) The glutathione-mediated detoxification pathway in yeast: an analysis using the red pigment that accumulates in certain adenine biosynthetic mutants of yeasts reveals the involvement of novel genes, *Arch. Microbiol. 180*, 108-117.

71. Dhaoui, M., Auchère, F., Blaiseau, P.-L., Lesuisse, E., Landoulsi, A., Camadro, J.-M., Haguenauer-Tsapis, R., and Belgareh-Touzé, N. (2011) Gex1 is a yeast glutathione exchanger that interferes with pH and redox homeostasis, *Molecular Biology of the Cell 22*, 2054-2067.

72. Lill, R., and Muehlenhoff, U. (2008) Maturation of iron-sulfur proteins in eukaryotes: Mechanisms, connected processes, and diseases, *Annu. Rev. Biochem. 77*, 669-700.

73. Lindahl, P. A., Morales, J. G., Miao, R., and Holmes-Hampton, G. (2009) Isolation of *Saccharomyces cerevisiae* mitochondria for Mössbauer, EPR, and electronic absorption spectroscopic analyses, *Method. Enzymol. 456,* 267-285.

74. Krebs, C., Price, J. C., Baldwin, J., Saleh, L., Green, M. T., and Bollinger, J. M. (2005) Rapid freeze-quench ^{57}Fe Mössbauer spectroscopy: Monitoring changes of an iron-containing active site during a biochemical reaction, *Inorg. Chem. 44*, 742-757.

75. Chen, Y.-L., and Yang, D.-P. (2007) Hyperfine interactions, In *Mössbauer Effect in Lattice Dynamics*, pp 29-77, Wiley-VCH Verlag GmbH & Co. KGaA, Weinheim, Germany.

76. Weil, J. A., and Bolton, J. R. (2006) Basic principles of paramagnetic resonance, In *Electron Paramagnetic Resonance*, pp 1-35, John Wiley & Sons, Inc., Hoboken, New Jersey, USA.

77. Morales, J. G., Holmes-Hampton, G. P., Miao, R., Guo, Y., Münck, E., and Lindahl, P. A. (2010) Biophysical characterization of iron in mitochondria isolated from respiring and fermenting yeast, *Biochemistry 49*, 5436-5444.

78. Park, J., McCormick, S. P., Chakrabarti, M., and Lindahl, P. A. (2013) Insights into the iron-ome and manganese-ome of Δ*mtm1 Saccharomyces cerevisiae* mitochondria, *Metallomics* 5, 656-672.

79. Nishida, K., and Silver, P. A. (2012) Induction of biogenic magnetization and redox control by a component of the target of rapamycin complex 1 signaling pathway, *PLoS Biol. 10*.

80. Miao, R., Kim, H., Koppolu, U. M. K., Ellis, E. A., Scott, R. A., and Lindahl, P. A. (2009) Biophysical characterization of the iron in mitochondria from Atm1p-depleted *Saccharomyces cerevisiae*, *Biochemistry 48*, 9556-9568.

81. Miao, R., Holmes-Hampton, G. P., and Lindahl, P. A. (2011) Biophysical investigation of the iron in Aft1-1(up) and Gal-YAH1 *Saccharomyces cerevisiae*, *Biochemistry 50*, 2660-2671.

82. Lesuisse, E., Santos, R., Matzanke, B. F., Knight, S. A. B., Camadro, J.-M., and Dancis, A. (2003) Iron use for haeme synthesis is under control of the yeast frataxin homologue (Yfh1), *Hum. Mol. Genet. 12*, 879-889.

83. Miao, R., Martinho, M., Morales, J. G., Kim, H., Ellis, E. A., Lill, R., Hendrich, M. P., Münck, E., and Lindahl, P. A. (2008) EPR and Mössbauer spectroscopy of intact mitochondria isolated from Yah1p-depleted *Saccharomyces cerevisiae*, *Biochemistry 47*, 9888-9899.

84. Remacha, M., Jimenez-Diaz, A., Bermejo, B., Rodriguez-Gabriel, M. A., Guarinos, E., and Ballesta, J. P. (1995) Ribosomal acidic phosphoproteins P1 and P2 are not required for cell viability but regulate the pattern of protein expression in *Saccharomyces cerevisiae*, *Mol. Cell. Biol. 15*, 4754-4762.

85. Felice, M. R., De Domenico, I., Li, L. T., Ward, D. M., Bartok, B., Musci, G., and Kaplan, J. (2005) Post-transcriptional regulation of the yeast high affinity iron transport system, *J. Biol. Chem. 280*, 22181-22190.

86. Lange, H., Kaut, A., Kispal, G., and Lill, R. (2000) A mitochondrial ferredoxin is essential for biogenesis of cellular iron-sulfur proteins, *Proc. Natl. Acad. Sci. U.S.A. 97*, 1050-1055.

87. Diekert, K., I.P.M. de Kroon, A., Kispal, G., and Lill, R. (2001) Isolation and subfractionation of mitochondria from the yeast *Saccharomyces cerevisiae*, *Method. Cell Biol. 65*, 37-51.

88. Singh, A., Kaur, N., and Kosman, D. J. (2007) The metalloreductase Fre6p in Fe-efflux from the yeast vacuole, *J. Biol. Chem. 282*, 28619-28626.

89. Kitagaki, H., Cowart, L. A., Matmati, N., Montefusco, D., Gandy, J., de Avalos, S. V., Novgorodo, S. A., Zheng, J., Obeid, L. M., and Hannun, Y. A. (2009) ISC1-dependent metabolic adaptation reveals an indispensable role for mitochondria in induction of nuclear genes during the diauxic shift in *Saccharomyces cerevisiae*, *J. Biol. Chem. 284*, 10818-10830.

90. Flohé, L., and Ötting, F. (1984) Superoxide dismutase assays, *Methods Enzymol. 105*, 93-104.

91. Ravindranath, S. D., and Fridovich, I. (1975) Isolation and characterization of a manganese-containing superoxide-dismutase from yeast, *J. Biol. Chem. 250*, 6107-6112.

92. Singh, A., Severance, S., Kaur, N., Wiltsie, W., and Kosman, D. J. (2006) Assembly, activation, and trafficking of the Fet3p•Ftr1p high affinity iron permease complex in *Saccharomyces cerevisiae*, *J. Biol. Chem. 281*, 13355-13364.

93. Kennedy, M. C., Emptage, M. H., Dreyer, J. L., and Beinert, H. (1983) The role of iron in the activation-inactivation of aconitase, *J. Biol. Chem. 258*, 1098-1105.

94. Kohlhaw, G. B. (1988) Isopropylmalate dehydratase from yeast, *Methods Enzymol. 166*, 423-429.

95. Drevland, R. M., Waheed, A., and Graham, D. E. (2007) Enzymology and evolution of the pyruvate pathway to 2-oxobutyrate in *Methanocaldococcus jannaschii*, *J. Bacteriol. 189*, 4391-4400.

96. Munujos, P., Coll-Cantí, J., González-Sastre, F., and Gella, F. J. (1993) Assay of succinate dehydrogenase activity by a colorimetric-continuous method using iodonitrotetrazolium chloride as electron acceptor, *Anal. Biochem. 212*, 506-509.

97. Kosman, D. J. (2003) Molecular mechanisms of iron uptake in fungi, *Mol. Microbiol. 47*, 1185-1197.

98. Yoon, H., Klinzing, G., and Blanch, H. W. (1977) Competition for mixed substrates by microbial-populations, *Biotechnol. Bioeng. 19*, 1193-1210.

99. Palmiter, R. D., and Huang, L. P. (2004) Efflux and compartmentalization of zinc by members of the SLC30 family of solute carriers, *Pflugers Archiv-European Journal of Physiology 447*, 744-751.

100. Papaefthymiou, G. C. (2010) The Mössbauer and magnetic properties of ferritin cores, *Biochim. Biophys. Acta (BBA) - General Subjects 1800*, 886-897.

101. Flattery-O'Brien, J. A., Grant, C. M., and Dawes, I. W. (1997) Stationary-phase regulation of the *Saccharomyces cerevisiae* SOD2 gene is dependent on additive

effects of HAP2/3/4/5- and STRE-binding elements, *Mol. Microbiol. 23*, 303-312.

102. Hughes, A. L., and Gottschling, D. E. (2012) An early age increase in vacuolar pH limits mitochondrial function and lifespan in yeast, *Nature 492*, 261-265.

103. Bulteau, A.-L., Dancis, A., Gareil, M., Montagne, J.-J., Camadro, J.-M., and Lesuisse, E. (2007) Oxidative stress and protease dysfunction in the yeast model of Friedreich ataxia, *Free Radic. Biol. Med. 42*, 1561-1570.

104. Park, J., McCormick, S. P., Chakrabarti, M., and Lindahl, P. A. (2013) Lack of iron regulation in *Saccharomyces cerevisiae* during post-exponential growth modes, *Submitted*.

105. Smirnov, M. N., Smirnov, V. N., Budowsky, E. I., Inge-Vechtomov, S. G., and Serebrjakov, N. G. (1967) Red pigment of adenine-deficient yeast *Saccharomyces cerevisiae*, *Biochem. Biophys. Res. Commun. 27*, 299-304.

106. Silver, J., Hamed, M. Y., and Morrison, I. E. G. (1985) Studies of the reactions of ferric iron with glutathione and some related thiols. Part V. Solid complexes containing Fe^{II} and glutathione or Fe^{III} with oxidized glutathione, *Inorg. Chim. Acta-Bioinorganic Chemistry 107*, 169-178.

107. Stevens, B. J. (1977) Variation in number and volume of mitochondria in yeast according to growth-conditions - Study based on serial sectioning and computer graphics reconstitution, *Biologie Cellulaire 28*, 37-56.

108. Bonawitz, N. D., Chatenay-Lapointe, M., Pan, Y., and Shadel, G. S. (2007) Reduced TOR signaling extends chronological life span via increased respiration and upregulation of mitochondrial gene expression, *Cell Metab. 5*, 265-277.

109. Magherini, F., Carpentieri, A., Amoresano, A., Gamberi, T., De Filippo, C., Rizzetto, L., Biagini, M., Pucci, P., and Modesti, A. (2009) Different carbon sources affect lifespan and protein redox state during *Saccharomyces cerevisiae* chronological ageing, *Cell. Mol. Life Sci. 66*, 933-947.

110. Barbet, N. C., Schneider, U., Helliwell, S. B., Stansfield, I., Tuite, M. F., and Hall, M. N. (1996) TOR controls translation initiation and early G1 progression in yeast, *Molecular Biology of the Cell 7*, 25-42.

111. Robertson, R. P. (2004) Chronic oxidative stress as a central mechanism for glucose toxicity in pancreatic islet beta cells in diabetes, *J. Biol. Chem. 279*, 42351-42354.

112. Cameroni, E., Hulo, N., Roosen, J., Winderickx, J., and Virgilio, C. D. (2004) The novel yeast PAS kinase Rim15 orchestrates G0-associated antioxidant defense mechanisms, *Cell Cycle 3*, 460-466.

113. Portnoy, M. E., Jensen, L. T., and Culotta, V. C. (2002) The distinct methods by which manganese and iron regulate the Nramp transporters in yeast, *Biochem. J. 362*, 119-124.

114. Wanke, V., Cameroni, E., Uotila, A., Piccolis, M., Urban, J., Loewith, R., and De Virgilio, C. (2008) Caffeine extends yeast lifespan by targeting TORC1, *Mol. Microbiol. 69*, 277-285.

115. Maris, A. F., Assumpção, A. L. K., Bonatto, D., Brendel, M., and Henriques, J. A. P. (2001) Diauxic shift-induced stress resistance against hydroperoxides in *Saccharomyces cerevisiae* is not an adaptive stress response and does not depend on functional mitochondria, *Curr. Genet. 39*, 137-149.

116. Yang, Z., and Klionsky, D. J. (2009) An overview of the molecular mechanism of autophagy, In *Autophagy in infection and immunity* (Levine, B., Yoshimori, T., and Deretic, V., Eds.), pp 1-32, Springer-Verlag, Berlin, Heidelberg, Germany.

117. Robinson, A. J., Overy, C., and Kunji, E. R. S. (2008) The mechanism of transport by mitochondrial carriers based on analysis of symmetry, *Proc. Natl. Acad. Sci. U.S.A. 105*, 17766-17771.

118. Mühlenhoff, U., Gerber, J., Richhardt, N., and Lill, R. (2003) Components involved in assembly and dislocation of iron-sulfur clusters on the scaffold protein Isu1p, *EMBO J. 22*, 4815-4825.

119. Kim, K. D., Chung, W. H., Kim, H. J., Lee, K. C., and Roe, J. H. (2010) Monothiol glutaredoxin Grx5 interacts with Fe-S scaffold proteins Isa1 and Isa2 and supports Fe-S assembly and DNA integrity in mitochondria of fission yeast, *Biochem. Biophys. Res. Commun. 392*, 467-472.

120. Babcock, M., de Silva, D., Oaks, R., Davis-Kaplan, S., Jiralerspong, S., Montermini, L., Pandolfo, M., and Kaplan, J. (1997) Regulation of mitochondrial iron accumulation by Yfh1p, a putative homolog of frataxin, *Science 276*, 1709-1712.

121. Nilsson, R., Schultz, I. J., Pierce, E. L., Soltis, K. A., Naranuntarat, A., Ward, D. M., Baughman, J. M., Paradkar, P. N., Kingsley, P. D., Culotta, V. C., Kaplan, J., Palis, J., Paw, B. H., and Mootha, V. K. (2009) Discovery of genes essential for heme biosynthesis through large-scale gene expression analysis, *Cell Metab. 10*, 119-130.

122. Lesuisse, E., Santos, R., Matzanke, B. F., Knight, S. A. B., Camadro, J. M., and Dancis, A. (2003) Iron use for haeme synthesis is under control of the yeast frataxin homologue (Yfh1), *Hum. Mol. Genet. 12*, 879-889.

123. Seguin, A., Sutak, R., Bulteau, A. L., Garcia-Serres, R., Oddou, J. L., Lefevre, S., Santos, R., Dancis, A., Camadro, J. M., Latour, J. M., and Lesuisse, E. (2010) Evidence that yeast frataxin is not an iron storage protein in vivo, *Biochim. Biophys. Acta-Mol. Basis Dis. 1802*, 531-538.

124. Hudder, B. N., Morales, J. G., Stubna, A., Münck, E., Hendrich, M. P., and Lindahl, P. A. (2007) Electron paramagnetic resonance and Mössbauer spectroscopy of intact mitochondria from respiring *Saccharomyces cerevisiae*, *J. Biol. Inorg. Chem. 12*, 1029-1053.

125. Reinders, J., Wagner, K., Zahedi, R. P., Stojanovski, D., Eyrich, B., van der Laan, M., Rehling, P., Sickmann, A., Pfanner, N., and Meisinger, C. (2007) Profiling phosphoproteins of yeast mitochondria reveals a role of phosphorylation in assembly of the ATP synthase, *Mol. Cell. Proteomics 6*, 1896-1906.

126. McNaughton, R. L., Reddi, A. R., Clement, M. H. S., Sharma, A., Barnese, K., Rosenfeld, L., Gralla, E. B., Valentine, J. S., Culotta, V. C., and Hoffman, B. M. (2010) Probing in vivo Mn^{2+} speciation and oxidative stress resistance in yeast cells with electron-nuclear double resonance spectroscopy, *Proc. Natl. Acad. Sci. U.S.A. 107*, 15335-15339.

127. Kang, Y., He, Y. X., Zhao, M. X., and Li, W. F. (2011) Structures of native and Fe-substituted SOD2 from *Saccharomyces cerevisiae*, *Acta Crystallogr. F-Struct. Biol. Cryst. Commun. 67*, 1173-1178.

128. Zhao, X. L., Leon, I. R., Bak, S., Mogensen, M., Wrzesinski, K., Hojlund, K., and Jensen, O. N. (2011) Phosphoproteome analysis of functional mitochondria isolated from resting human muscle reveals extensive phosphorylation of inner membrane protein complexes and enzymes, *Mol. Cell. Proteomics 10*.

129. Akhmedov, D., De Marchi, U., Wollheim, C. B., and Wiederkehr, A. (2012) Pyruvate dehydrogenase E1 alpha phosphorylation is induced by glucose but does not control metabolism-secretion coupling in INS-1E clonal beta-cells, *Biochim. Biophys. Acta-Mol. Cell Res. 1823*, 1815-1824.

130. Herrero, E., Ros, J., Belli, G., and Cabiscol, E. (2008) Redox control and oxidative stress in yeast cells, *Biochim. Biophys. Acta-Gen. Subj. 1780*, 1217-1235.

131. Whittaker, M. M., and Whittaker, J. W. (2012) Metallation state of human manganese superoxide dismutase expressed in *Saccharomyces cerevisiae*, *Arch. Biochem. Biophys. 523*, 191-197.

132. Jeong, J. H., Kwon, E. S., and Roe, J. H. (2001) Characterization of the manganese-containing superoxide dismutase and its gene regulation in stress response of *Schizosaccharomyces pombe*, *Biochem. Biophys. Res. Commun. 283*, 908-914.

133. Fleischhacker, A. S., Stubna, A., Hsueh, K. L., Guo, Y. S., Teter, S. J., Rose, J. C., Brunold, T. C., Markley, J. L., Munck, E., and Kiley, P. J. (2012) Characterization of the 2Fe-2S cluster of *Escherichia coli* transcription factor IscR, *Biochemistry 51*, 4453-4462.

134. Robertson, L. S., Causton, H. C., Young, R. A., and Fink, G. R. (2000) The yeast A kinases differentially regulate iron uptake and respiratory function, *Proc. Natl. Acad. Sci. U.S.A. 97*, 5984-5988.

135. Bayeva, M., Khechaduri, A., Puig, S., Chang, H.-C., Patial, S., Blackshear, P. J., and Ardehali, H. (2012) mTOR regulates cellular iron homeostasis through tristetraprolin, *Cell Metab. 16*, 645-657.